



People's Democratic Republic of Algeria
Ministry of Higher Education and Scientific Research
University of Batna
Faculty of Technology
Department of Electronics



MODELING OF MULTIGATE FET-BASED SENSORS FOR ENGINEERING APPLICATIONS

A Dissertation Presented to the University of Batna

Department of Electronics

By

Mohamed MEGUELLATI

Submitted in fulfillment of the requirement of the degree of Doctor of Science in

Electronics

Advisor

Prof. Fayçal DJEFFAL

Approved by:

Full name	Title	Quality	Establishment
Zohir Dibi	Professor	Chairman	University of Batna
Fayçal Djeffal	Professor	Supervisor	University of Batna
Abdelhamid Benhaya	Professor	Examiner	University of Batna
Abdelouahab Bentabet	Assoc.Professor	Examiner	University of Bordj-Bou-Argeridj
Amar Mezache	Assoc.Professor	Examiner	University of M'sila
Abdesselam Hocini	Assoc.Professor	Examiner	University of M'sila



République Algérienne Démocratique Et Populaire
Ministère De L'Enseignement Supérieur
Et De La Recherche Scientifique
Université De Batna
Faculté De Technologie



Thèse

Présentée au

Département D'Electronique

Pour l'obtention du diplôme de

Doctorat en sciences en Electronique

Par

Mohamed MEGUELLATI

Intitulée

Modélisation des capteurs multigrille à base de FET pour des applications de l'ingénierie.
Modeling of multigate FET-based sensors for engineering applications.

Devant le jury composé de:

Zohir DIBI	Professeur. U. Batna	Président
Fayçal DJEFFAL	Professeur. U. Batna	Rapporteur
Abdelhamid BENHAYA	Professeur. U. Batna	Examineur
Abdelouahab BENTABET	M.C. U. Bordj-Bou-Argeridj	Examineur
Amar MEZACHE	M.C. U. M'sila	Examineur
Abdesselam HOCINI	M.C. U. M'sila	Examineur

Acknowledgment

Firstly, I thank **Allah**, the Most High, for the opportunity He gave me to study, to research and to write this dissertation. **Thank Allah**, my outmost thanks, for giving me the ability, the strength, attitude and motivation through this research and to complete this work.

I wish to express my special gratitude to my supervisor Professor Fayçal DJEFFAL for accepting me as a PhD student at the Department of Electronics. I am sincerely grateful for your guidance, wisdom, and specially your endless patients in dealing with me throughout all these years. It is difficult to overstate my gratitude to you, with your enthusiasm, your inspiration, and your great efforts make this approach easier. Many thanks to you for assisting me throughout my thesis-writing period; you provided encouragement, sound advice, good company, and lots of good ideas. Thank you for believing me and for giving me good advice, support and freedom along the way. I'm grateful for all scientific discussion we had in this journey and sharing fun time together.

I would like to thank Zohir DIBI from University of Batna for being president of the examination committee. I would like to thank my oral thesis committee members, Abdelhamid BENHAYA from University of Batna, Abdelouahab Bentabet from University of Bordj-Bou-Arreridj, Amar Mezache and Abdesselam Hocini from University of M'sila, for accepting the examination of this thesis.

I would like to thank all my friends, colleagues and the staff at the Department of Electronics, University of Batna for their help along the realisation of this work.

My deep gratitude is due, to my parents for their devotion, sacrifices, continuous guidance, encouragement, support, and prayers for my whole life. Thanks are due, to my brother and my sisters for their cooperation and help. I also want to thank all my immediate and extended family members for all their love and support.

Contents

Acknowledgment	
List of figures	
List of tables	
Published work	
Introduction	1
Layout of the Thesis	3
Chapter I: Sensors and their applications in engineering	4
I.1 Introduction	5
II.2 Chemical sensors	5
II.2.1 Definitions	5
II.2.2 Classification of chemical sensors	6
II.2.2.1. Optical devices.....	7
II.2.2.2 Electrochemical devices.....	8
II.2.2.3 Electrical devices	9
II.2.2.4 Mass sensitive devices	9
II.2.2.5 Magnetic devices	9
II.2.2.6 Thermometric devices.....	10
II.2.3 Applications of chemical sensors.....	10
II.3 Dosimetry and Radiation Protection.....	11
II.3.1 Importance of Dosimetry	11
II.3.2 Passive Dosimetry.....	12
II.3.3 Active Dosimetry	13
II.4 Sensors and sensor systems for Industrial and environmental Applications	16
I.6 conclusion	19
Chapter II: A novel design to deep submicron FET-based chemical sensors	20
II.1 Introduction	21
II.2 A novel multigate design to improve the sensitivity behavior for deep submicron ISFET-based sensors	22
II.2.1 Derivation of DG ISFET sensitivity model	22
II.2.2 Results and discussions	25
II.3 Numerical Analysis of Thin Film Junctionless pH-ISFET Sensor	27
II.3.1 JISFET design and its parameters	27
II.3.2 Results and discussions.....	30
III.4 a Junctionless-multigate design to improve the electrical performances for deep submicron ISFET-based sensors	33
II.4.1 JGAASISFET design and simulation	33
II.4.2 Results and discussions.....	36
III.5 Conclusion.....	38
Chapter III:New monitoring multi-gate sensor (DDGAA) RADFET	39
III.1 Introduction	40
III.2 Conventional pMOS dosimeters (RADFETs).....	41
III.3 Theory development and model derivation DDGAA RADFET	43
III.3.1 Interface potential analysis	43
III.3.2 Threshold voltage shift model.....	46

III.4 Results and discussion	47
III.5 Conclusion	51
Chapter IV: Improvement and Implementation of the (DDGAA) RADFET sensor in radioactive environment	52
IV.1 Introduction	53
IV.2 GA-based optimization of the radiation sensitivity of DDGAA RADFET	53
IV.2.1 Genetic algorithms	53
IV.2.1.1 How Genetic Algorithms are Different from Traditional Methods	54
IV.2.1.2 How Genetic Algorithms Work	55
IV.2.1.3 Basic steps of genetic algorithms	56
IV.2.2 GA-based sensitivity optimisation	59
IV.3 Radioactive environment sensing.....	60
IV.3.1 Multilayered perceptron (MLP) networks	61
IV.3.2 Training Algorithm	63
IV.3.3 Adaptive noise filtering using Back Propagation Neural Network.....	64
IV.3.3.1 Approach	64
IV.3.4 Result and discussion	65
IV.4 Conclusion.....	67
Conclusions and future work	68
Bibliography	70
Appendix	76

LIST OF FIGURES

Chapter I:

Figure I. 1: Schematic representation of the composition and function of an optical chemical sensor	07
Figure I. 2: General representation of electrochemical sensor	08
Figure I.3: Simplified schematic of a p-channel MOSFET dosimeter	14
Figure I.4: (a) Quartz fiber electroscope without any absorbed dose. (b) Incident radiation produces charge pairs in the ionization chamber that decreases the charge on the electrometer pushing the electrodes close together. The eyepiece of the microscope is shown to read a dose of 140 units	15

Chapter II:

Figure II.1: Cross-section of the proposed DG ISFET structure Derivation of DG ISFET sensitivity model	22
Figure II.2: I-V characteristics as function of pH values for (a) $L=0.1\mu\text{m}$ and (b) $L=10\mu\text{m}$	25
Figure II.3: Variation of the sensor sensitivity for conventional (SG) and DG ISFET as function of channel length	26
Figure II.4: C-V curves response of the proposed AM-based pH-JISFET for different pH values (from $\text{pH}=2$ to $\text{pH}=12$).....	27
Figure II.5: Longitudinal cross sections showing the doping profiles (a) conventional IM-based pH-ISFET and the (b) Proposed AM-based pH-JISFET.....	28
Figure II.6: Curves of the drain current and the transconductance versus bias voltage with different pH values.....	30
Figure II.7: Bias voltage of the AM-based pH-JISFET as function of pH values. The inset shows bias voltage of the conventional IM-based pH-ISFET as function of pH values for both working regimes (linear and saturation).....	31
Figure II.8: Longitudinal cross sections showing the doping profiles and channel-designs (a) conventional pH-ISFET and the (b) Proposed pH-JGAAISFET	33
Figure II.9: C-V curves response of the proposed AM-based pH-JGAAISFET for different pH values (from $\text{pH}=2$ to $\text{pH}=12$).....	35

Figure II.10: Curves of the drain current versus bias voltage with different pH values.....	36
--	----

Chapter III:

Figure III.1: Cross section of pMOS dosimeter (RADFET) with the defects created by radiation.....	41
Figure III.2: Cross-sectional view of the proposed DDGAA RADFET design.....	43
Figure III.3: (a) Variation of surface potential along the channel (b) Variation of interface potential along the SiO ₂ /Si ₃ N ₄ interface for different irradiation-induced interfacial traps densities with ($V_{gs} = -5V, V_{ds} = IV, L = 100nm, t_1 = 5nm, t_2 = 5nm, \epsilon_1 = 3.9, \epsilon_2 = 7.5, t_{si} = 20nm, N_D = 10^{15} cm^{-3}$)	47
Figure III.4: Threshold voltage shift variation against the irradiation-induced interfacial traps densities for the conventional and DDGAA RADFET designs.....	48
Figure III.5: Variation of threshold voltage shift in function of the absorbed radiation dose for the conventional and DDGAA RADFET designs	50
Figure III.6: Set-up for a measurement of V_{th} and absorbed radiation dose (read-out circuit configuration)	50

Chapter IV:

Figure IV.1: Flow Diagram of Genetic Algorithm	56
Figure IV.2: Two-point Crossover	58
Figure IV.3: Mutation Operator	58
Figure IV.4: Multilayered perceptron networks with two hidden layers	62
Figure IV.5: BPNN Filter Structure	65
Figure IV.6: The distorted image due to the transmission noise	66
Figure IV.7: The denoised image using MLP	66
Figure IV.8: Validation of the neural network result for test set	67

LIST OF TABLES

Chapter I:

Table I.1: Summary of advantages and disadvantages of each sensor	18
--	----

Chapter II:

Table II.1: Simulation parameters of both devices	29
--	----

Table II.2: pH sensitivity and electrical characteristics of both devices	32
--	----

Table II.3: Simulation parameters of both devices	35
--	----

Table II.4: pH sensitivity and electrical characteristics of both devices	37
--	----

Chapter IV:

Table IV.1: DDGAA RADFET Design Parameters	60
---	----

Table IV.2: Sample Hetero Association table relating input vectors and output vectors of the BPNN	65
---	----

Related publications work

Book chapter

[1] Fayçal DJEFFAL and **Mohamed MEGUELLATI**, “multigate RADFET dosimeter For Radioactive Environment Monitoring Applications”, series title: lecture notes in electrical engineering, Editors names: Gi-Chul Yang, SIO-IONG AO. Len Gelman, Title of Book/Volume/Conference: IAENG Transactions on Engineering Technologies -Special Issue of the World Congress on Engineering 2012, GPU/PS: 3/9059, SPIN: GT-C-CTP-09/2011, Springer.

Journal papers

[J.1] **M. Meguellati**, F. Djeflal, D. Arar, F. Douak and L. Khettache, "New RADFET Dosimeter Design For Radioactive Environment Monitoring Applications", J. Engineering Letters, Vol: 20-4, pp. 20-24, 2012.

[J.2] **M. Meguellati**, F. Djeflal, "New Dual-Dielectric Gate All Around (DDGAA) RADFET dosimeter design to improve the radiation sensitivity", Published by Elsevier, J. Nuclear Instruments and Methods in Physics Research A, pp. 24–28, 683, 2012.

[J.3] F. Djeflal, **M. Meguellati**, N. Abdelmalek," Numerical Analysis of Thin Film Junctionless pH-ISFET Sensor", J. Sensors & Transducer, Published by IFSA, pp. 35-40, Vol. 123, December 2010.

[J.4] T. Bendib, F.Djeflal, **M. Meguellati**, A. Benhaya and M. Chahdi, "A compact drain current model based on Genetic algorithm computation to study the nanoscale Double-Gate MOSFETs", J. Semiconductor Physics, Quantum Electronics and Optoelectronics, pp. 27-30, 12(1), 2009.

[J.5] F. Djeflal, **M. Meguellati**, A. Benhaya, "A two-dimensional analytical analysis of subthreshold behavior to study the scaling capability of nanoscale graded channel gate stack DG MOSFETs", Published by Elsevier, J. Physica E, pp. 1872–1877, 41, 2009.

Conference papers

More than ten international conferences.

Introduction

In everyday life, we use our senses to interact with the environment. We can see, touch, smell, hear and taste the external world surrounding us through interactions that usually occur with an initial contact between an organism and its environment [1-2]. The sensors are widely recognized as one of the most promising solution for several biomedical and engineering problems like: nuclear reactors, chirurgical interventions, etc. The good operation of engineering systems is based on two fundamental aspects: (1) the control of different units and blocks of the system and (2) data processing and acquisition from the environment which is based on the sensors-based block. In electronic industry the FET-based devices are considered as attractive alternatives for chemical, physiological, nuclear industry, space, radiotherapy and environment monitoring applications due to their rapid time responses, reliability, low power consumption, high dose range, and compatibility to standard CMOS technology and on-chip signal processing [3-6]. To extract information accurately about the environment alone requires the use of a new generation of FET-based sensors for deep submicron scale. As semiconductor devices are scaled into the deep submicron regime, short-channel effects (SCEs) begin to plague conventional planar CMOS-based sensors. To avoid the electrical constraints, a new design and improvement of conventional FET-based sensors become important. The multigate MOSFETs are the most suitable devices for the scaling of CMOS down to the submicron range. In this dissertation, we propose and investigate the applicability of multigate structures for the design, modeling and optimization of new architectures of submicron sensors for engineering-based applications.

Firstly, a new pH-ISFET sensor, called the Junctionless ISFET sensor (JISFET), and its numerical analysis have been proposed, investigated and expected to improve the fabrication process and the sensitivity behavior for pH-ISFET sensor-based applications. The numerical analysis has been used to predict and compare the performances of the proposed design and conventional pH-ISFET. In addition, a novel multigate sensor is proposed to improve the behavior of the ion-sensitive field-effect transistor (ISFET) sensitivity in deep submicron domain for deep submicroelectronics applications. The proposed structure has been analyzed and validated by the good sensitivity obtained in deep submicron regime. moreover, a new multigate pH-ISFET

sensor design, called the Junctionless Gate All Around (GAA) ISFET sensor (JGAAISFET), and its numerical analysis have been proposed, investigated and expected to improve the fabrication process and the sensitivity behavior for pH-ISFET sensor-based applications. The numerical analysis has been used to predict and compare the performances of the proposed design and conventional pH-ISFET, where the comparison of device architectures shows that the proposed pH- JISFET sensor exhibits a superior performance with respect to the conventional pH-ISFET in term of fabrication process and electrical performances. The numerical model provides a basic framework to account for the electronic and chemical performances in future multigate pH-ISFET designs, being easily adaptable to gate structures as the double-gate (DG) or Tri-gate (TG). The obtained results make the proposed chemical sensors a promising candidate for future integrated CMOS-based sensors for chemical applications.

Secondly, a new radiation sensitive FET (RADFET) dosimeter design (called the Dual-Dielectric Gate All Around DDGAA RADFET dosimeter) to improve the radiation sensitivity performance and its analytical analysis have been proposed, investigated and expected to improve the sensitivity behavior and fabrication process for RADFET dosimeter-based applications. Analytical models have been developed to predict and compare the performance of the proposed design and conventional (bulk) RADFET, where the comparison of device architectures shows that the proposed design exhibits a superior performance with respect to the conventional RADFET in term of fabrication process and sensitivity performances. The proposed design has linear radiation sensitivities of approximately $95.45\mu\text{V}/\text{Gy}$ for wide irradiation dose range (from Dose=50Gy to Dose=3000 Gy). Our results showed that the analytical analysis is in close agreement with the 2-D numerical simulation over a wide range of devices parameters. The obtained results make the DDGAA RADFET dosimeter an alternative solution to improve the monitoring process into radioactive environment.

Finally, Genetic Algorithm-based approach has been developed to optimize (maximization) the sensor sensitivity in order to apply it for a monitoring problem. In this context, the image denoising process is considered in this work, where the problem of mapping from a noisy image to a noise-free image is investigated. In this work we attempt to learn this mapping directly with a plain multi layer perceptron (MLP) applied to denoising image. The proposed device and the Artificial Neural Networks (ANNs) have been used to study and show the impact of the proposed dosimeter on the environment monitoring and remote sensing applications. The proposed approach can

be used for remote sensing applications. It is to note that our work can be extended to implement the proposed design into Software tools in order to study the engineering systems under radiation conditions.

Layout of the Thesis

To make the work understandable and more consistent this thesis is divided into five chapters.

The chapter I presents a brief discussion of the several types of sensors. At the beginning, we defined the chemical sensors, and we give a describable of his classification and their applications. Then we define and describe the different type of radiation sensors.

A new design of pH-ISFET called Junctionless ISFET sensor (pH-JISFET) is proposed for future CMOS-based sensors. Also, a novel Double Gate (DG) ISFET, to study and improve the sensor sensitivity in deep submicron regime, are given in chapter II. In addition, we propose a new design of pH-ISFET called Junctionless Gate All Around pH-ISFET sensor (pH-JGAAISFET). Finally, some concluding notes are given.

In the chapter III we present the main concept related to the conventional (bulk) RADFET device. Also, we derive an analytical interface potential distribution including radiation-induced interface-traps. The threshold voltage shift model can then be determined based on the interface potential model. In addition, we investigate the performance of the proposed design.

In the chapter IV we present the applicability of genetic algorithms (GAs) and Artificial Neural Networks (ANNs) approaches to optimize and improve the radiation sensitivity of the DDGAA RADFET for integrated CMOS-based dosimeters. Moreover, the proposed dosimeter model was used to study and show the impact of the proposed design on the environment monitoring applications.

In conclusion, a few suggestions for future research directions are included.

Chapter I

Sensors and their applications in engineering

Abstract: Sensors engineering are central to industrial applications being used for process control, monitoring, and safety. Sensors are also central to medicine being used for diagnostics, monitoring, critical care, and public health. This chapter is focused on presenting a brief overview of the most sensors applied in engineering systems, for different application areas, as well as the challenges presented in their implementations. So, this chapter is a brief introduction to sensing technology and identifies some of the opportunities and associated challenges. This chapter can be considered as an introductory platform of our work, which will be presented in this thesis.

I.1 Introduction

Recently there has been much interest sensors, in different application such as health, medical, spatial, control,...etc..., generated and good progress made in the study of engineering system. Sensors belong to the modern world like the mobile phone, the compact disc or the personal computer [7]. Chemical and radiation sensors, as a special variety of sensors, can be found, for example, in a cold storage place in the form of a freshness sensor which detects spoiled food. A generation ago, the word sensor was not widely used. Today, however, sensors are becoming ubiquitous in our daily lives. Our world is changing rapidly, and sensors play an important role in this process. Chemical and radiation sensors analyze our environment, i.e. they detect which substances are present and in what quantity. Dosimeters measure an individual's or an object's [7-11] exposure to something in the environment particularly to a hazard inflicting cumulative impact over long periods of time, or over a lifetime. This article concentrates on the radiation dosimeter, which measures exposure to ionizing radiation. The radiation dosimeter is of fundamental importance in the disciplines of radiation dosimetry and health physics. Other types of dosimeters are sound dosimeters, ultraviolet dosimeters and electromagnetic field dosimeters. There are thousands of sensors in several domain of application. We most interest for chemical and radiation sensors.

In this chapter we briefly discuss the several types of sensors. At the beginning, we defined the chemical sensors, and we give a describable of his classification and their applications. Then we define and describe the different type of radiation sensors. This chapter can be considered as an introductory platform for further chapters.

II.2 Chemical sensors

II.2.1 Definitions

A chemical sensor is a device that transforms chemical information, ranging from the concentration of a specific sample component to total composition analysis, into an analytically useful signal. A physical sensor is a device that provides information about a physical property of the system [7]. A chemical sensor is an essential component of an analyzer. In addition to the sensor, the analyzer may contain devices that perform the following functions: sampling, sample transport, signal processing, data processing. An analyzer may be an essential part of an automated system. The analyzer working according to a sampling plan as a function of time acts as a monitor [7,12].

Chemical sensors contain two basic functional units: a receptor part and a transducer part. Some sensors may include a separator which is, for example, a membrane. In the receptor part of a sensor the chemical information is transformed into a form of energy which may be measured by the transducer. The transducer part is a device capable of transforming the energy carrying the chemical information about the sample into a useful analytical signal. The transducer as such does not show selectivity [7,13].

The receptor part of chemical sensors may be based upon various principles:

- Physical, where no chemical reaction takes place. Typical examples are those based upon measurement of absorbance, refractive index, conductivity, temperature or mass change.
- Chemical, in which a chemical reaction with participation of the analyte gives rise to the analytical signal.
- Biochemical, in which a biochemical process is the source of the analytical signal. Typical examples are microbial potentiometric sensors or immunosensors. They may be regarded as a subgroup of the chemical ones. Such sensors are called biosensors.

In some cases it is not possible to decide unequivocally whether a sensor operates on a chemical or on a physical principle. This is, for example, the case when the signal is due to an adsorption process. Sensors are normally designed to operate under well defined conditions for specified analytes in certain sample types [7]. Therefore, it is not always necessary that a sensor responds specifically to a certain analyte. Under carefully controlled operating conditions, the analyte signal may be independent of other sample components, thus allowing the determination of the analyte without any major preliminary treatment of the sample. Otherwise unspecific but satisfactory reproducible sensors can be used in series for multicomponent analysis using multivariate calibration software and signal processing. Such systems for multicomponent analysis are called sensor arrays [7].

II.2.2 Classification of chemical sensors

The development of instrumentation, microelectronics and computers makes it possible to design sensors utilizing most of the known chemical, physical and biological

principles that have been used in chemistry. Chemical sensors may be classified according to the operating principle of the transducer.

II.2.2.1. Optical devices

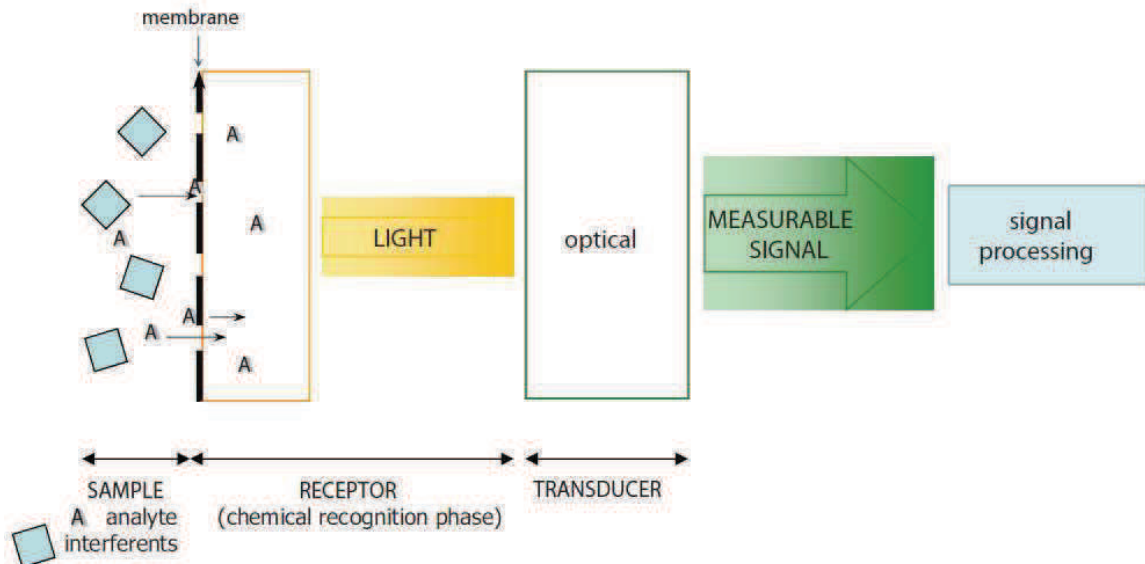


Figure I. 1: Schematic representation of the composition and function of an optical chemical sensor [14].

The Optical devices transform changes of optical phenomena, which are the result of an interaction of the analyte with the receptor part as shown in figure I.1 [7,15]. This group may be further subdivided according to the type of optical properties which have been applied in chemical sensors:

- a) Absorbance, measured in a transparent medium, caused by the absorptivity of the analyte itself or by a reaction with some suitable indicator.
- b) Reflectance is measured in non-transparent media, usually using an immobilized indicator.
- c) Luminescence, based on the measurement of the intensity of light emitted by a chemical reaction in the receptor system.
- d) Fluorescence, measured as the positive emission effect caused by irradiation. Also, selective quenching of fluorescence may be the basis of such devices.
- e) Refractive index, measured as the result of a change in solution composition. This may include also a surface plasmon resonance effect.
- f) optothermal effect, based on a measurement of the thermal effect caused by light absorption.

g) Light scattering, based on effects caused by particles of definite size present in the sample. The application of many of these phenomena in sensors became possible because of the use of optical fibers in various configurations. Such devices have also been called optodes [7,15-18]. It should be emphasized that fiber optics now commonly used are only technical devices applicable in a large group of optical sensors which can be based on various principles.

II.2.2.2 Electrochemical devices

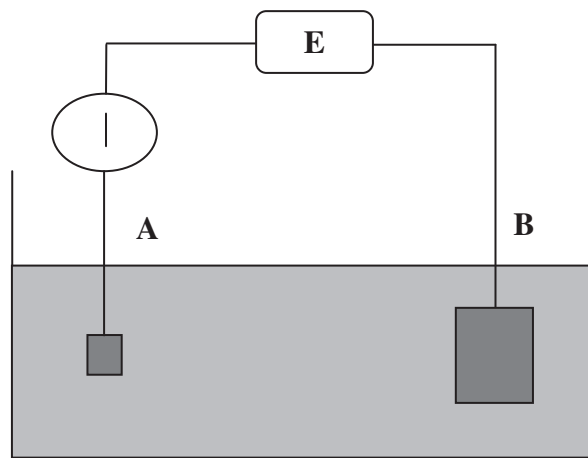


Figure I. 2: General representation of electrochemical sensor.

The Electrochemical devices transform the effect of the electrochemical interaction analyte – electrode into a useful signal as shown in figure I.2. Such effects may be stimulated electrically or may result in a spontaneous interaction at the zero-current condition. The following subgroups may be distinguished:

- a) Voltammetric sensors, including amperometric devices, in which current is measured in the d.c. or a.c. mode. This subgroup may include sensors based on chemically inert electrodes, chemically active electrodes and modified electrodes. In this group are included sensors with and without (galvanic sensors) external current source.
- b) Potentiometric sensors, in which the potential of the indicator electrode (ion-selective electrode, redox electrode, metal oxide electrode) is measured against a reference electrode.
- c) Chemically sensitized field effect transistor (CHEMFET) in which the effect of the interaction between the analyte and the active coating is transformed into a

change of the source-drain current. The interactions between the analyte and the coating are, from the chemical point of view, similar to those found in potentiometric ion-selective sensors.

- d) Potentiometric solid electrolyte gas sensors, differing from class 2b) because they work in high temperature solid electrolytes and are usually applied for gas sensing measurements.

II.2.2.3 Electrical devices

The Electrical devices based on measurements, where no electrochemical processes take place, but the signal arises from the change of electrical properties caused by the interaction of the analyte [7,19].

- a) Metal oxide semiconductor sensors used principally as gas phase detectors, based on reversible redox processes of analyte gas components.
- b) Organic semiconductor sensors, based on the formation of charge transfer complexes, which modify the charge carrier density.
- c) Electrolytic conductivity sensors.
- d) Electric permittivity sensors.

II.2.2.4 Mass sensitive devices

The Mass sensitive devices transform the mass change at a specially modified surface into a change of a property of the support material. The mass change is caused by accumulation of the analyte [7].

- a) Piezoelectric devices used mainly in gaseous phase, but also in solutions, are based on the measurement the frequency change of the quartz oscillator plate caused by adsorption of a mass of the analyte at the oscillator.
- b) Surface acoustic wave devices depend on the modification of the propagation velocity of a generated acoustical wave affected by the deposition of a definite mass of the analyte.

II.2.2.5 Magnetic devices

The Magnetic devices based on the change of paramagnetic properties of a gas being analyzed. These are represented by certain types of oxygen monitors [7,20].

II.2.2.6 Thermometric devices

The Thermometric devices based on the measurement of the heat effects of a specific chemical reaction or adsorption which involve the analyte. In this group the heat effects may be measured in various ways, for example in the so called catalytic sensors the heat of a combustion reaction or an enzymatic reaction is measured by use of a thermistor [7]. The devices based on measuring optothermal effects (If) can alternatively be included in this group.

This classification represents one of the possible alternatives. Sensors have, for example, been classified not according to the primary effect but to the method used for measuring the effect. Or also been classified according to the application to detect or determine a given analyte. Another basis for the classification of chemical sensors may be according to the mode of application, It is, of course, possible to use various classifications as long as they are based on clearly defined and logically arranged principles.

The biosensors are not presented as a special class because the process on which they are based is, in general, common to chemical sensors. They may be also differentiated according to the biological elements used in the receptor. Those may be: organisms, tissues, cells, organelles, membranes, enzymes, antibodies, etc [7]. The biosensors may have several enzymatic systems coupled which serve for amplification of the signal [21,22]. Various sensors may be combined in sets which are often called multisensors.

II.2.3 Applications of chemical sensors

Chemical sensors consist of a recognition element that is sensitive to stimuli produced by various chemical compounds (analyte) and a transduction element that generates a signal whose magnitude is functionally related to the concentration of the analyte. Chemical sensors also include a special branch referred to as biosensors for the recognition of biochemicals and bio-reactions. The use of biological elements such as organisms, enzymes, antibodies, tissues, and cells as receptors differentiates biosensors from conventional chemical sensors. In general, the chemical sensors are broadly classified into gas, liquid, and solid particulate sensors based on the phases of the analyte. They are further categorized as optical, electrochemical, thermometric, and

gravimetric (mass sensitive) sensors according to the operating principle of the transducer [23].

Chemical sensors have become an indispensable part of our technology driven society and can be found in chemical process, pharmaceutical, food, biomedical, environmental, security, industrial safety, clinical, and indoor monitoring applications to highlight a few [16-19]. Like many fields in science, chemical sensors have benefited from the growing power of computers, integrated electronics, new materials, novel designs, and processing tools. Manifestation of such technological changes can be seen in the development of miniaturized, inexpensive, portable, and mass manufacturable chemical sensors capable of static and continuous measurements even in remote environments [23]. Moreover, research on nanostructured materials and the use of sensor arrays in electronic nose (e-nose) systems is addressing the need for better analyte selectivity. Breakthroughs over the last decade have pushed chemical sensors into new markets [13,15,16], as well as new applications within existing markets.

II.3 Dosimetry and Radiation Protection

II.3.1 Importance of Dosimetry

It is a universally accepted fact that radiation causes damage, which can range from a subtle cell mutation in a living organism to the bulk damage in a silicon detector. The type of damage depends mainly on the type and energy of radiation and the type of material. This damaging mechanism of radiation is sometimes exploited for the benefit of mankind. An obvious example is the radiation therapy of cancer, where cancer cells are targeted and destroyed by radiation [24].

Unfortunately the damage caused by radiation cannot always be easily quantified. Some types of cell mutations caused by radiation take years to develop into detectable cancer. The same is true for electronic components that are in a hostile radiation field. The damage is so slow that often it is hard to notice the small degradation in performance. The question is, how do we then find out if a particular individual or equipment has received a high enough dose. The answer lies in the statistics. There have been extensive studies to determine the safe radiation levels for individuals, radiation workers, and equipments using statistical inferences of the damage data collected over a long period of time. Based on these studies, standards have been set for maximum allowable dose to humans. For materials, in most of the

cases, such as silicon detectors in a particle accelerator, the issue is operational degradation and not safety and therefore no universally accepted standards exist [24].

II.3.2 Passive Dosimetry

Passive dosimetries involve the use of a material to record dose and then take the material out of the radiation environment to read the recorded value. This method is not suitable for measuring instantaneous dose rates but is highly successful and convenient for measuring integrated dose. Some of the commonly used passive dosimetry techniques are described below.

a. Thermoluminescent Dosimetry

TLDs can measure only integrated doses since they must be allowed to absorb and store energy. Even though other more efficient detectors are now available, still due to their simplicity of operation, TLDs are being used extensively in different fields. Generally the intention is to determine the dose received by a person or equipment, such as a semiconductor detector, over a long period of time [24-27].

TL dosimeters are also being routinely used in experiments at particle accelerators, where the aim is to determine the integrated dose received by the radiation vulnerable devices, such as silicon detectors. This approach has been highly successful since these devices do not need any electronic circuitry for operation and can be easily installed and retrieved. The drawback is that they cannot be used to measure instantaneous doses and are also not as accurate as electronic detectors [24]. Another area in which TL dosimeters are gaining interest is the clinical dosimetry, which has traditionally been occupied by ionization chambers and semiconductor detectors.

b. Optically Stimulated Luminescence Dosimetry

Thermal stimulation is not the only means of retrieving stored energy from materials.

There are also materials, which emit light when stimulated by light photons. These materials, called optically stimulated luminescence or simply OSL materials, form a new class of dosimeters with qualities much superior than the conventional TL dosimeters. The OSL materials can store energy in the same way as TL materials but they give off light when stimulated optically instead of thermally as in the case of TLDs. This is a relatively new technology and was mostly unheard of before 1992 [24].

Looking at the list above, it is quite evident that OSL materials have many desirable characteristics. Therefore since the realization of their potential, OSL dosimeters are becoming more and more popular.

C. Film Dosimetry

Film dosimetry is based on the so called radiochromatic materials, which change color when exposed to radiation. Since the amount of this coloration is proportional to the delivered dose, therefore radiochromatic films provide a direct means of dose measurement.

D. Track Etch Dosimetry

Track etch detectors are usually made of plastics in the form of polymer foils. Since these materials are fairly inexpensive, they are widely used for personal and environmental radiation monitoring [24].

The most commonly used track etch material is the so called CR39 plastic, which has the composition of polyallyl diglycol carbonate. The material can be bought in the form of large sheets, which can then be cut into desired sizes.

II.3.3 Active Dosimetry

Active dosimetry involves use of an electronic detector and is suitable for measuring both instantaneous and integrated doses. The most commonly employed active dosimeters are described below.

a. Ion Chamber Dosimetry

Ionization chambers have long been used in all types of dosimetry because of their simplicity in design and low operating cost. In clinical practice, they have become standard dosimetry tools, though the trend is now shifting towards other types of detectors such as semiconductor devices [24,27].

b. Solid State Dosimetry

b.1 MOSFET Dosimeter

MOSFET is an acronym of Metal Oxide Semiconductor Field Effect Transistor. This technology has existed for a number of years but its use has been limited to electronic devices as shown in figure I.3. Its possible role as a radiation dosimeter was investigated a few years ago. It was found that it could not only work as an efficient dosimeter but also provided many advantages over conventional dosimeters. Ever since, its use has considerably increased in the field of radiation therapy [24].

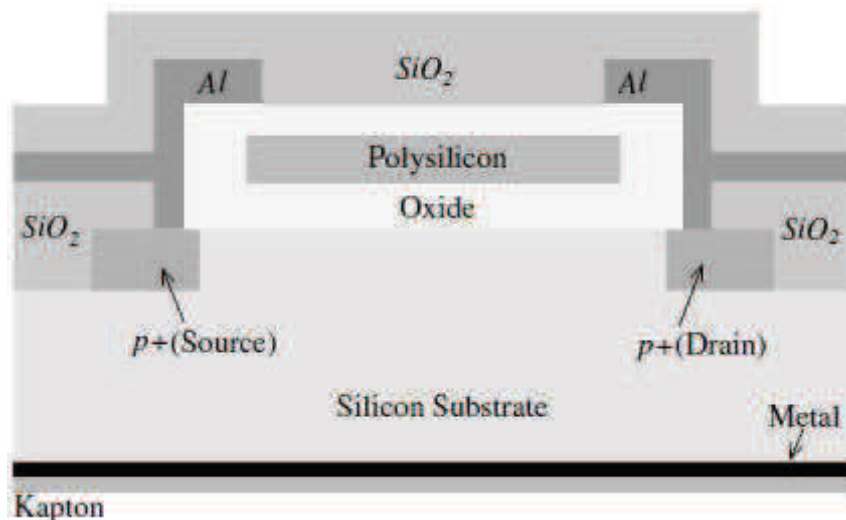


Figure 11.3: Simplified schematic of a p-channel MOSFET dosimeter [14].

b.2 Diamond Dosimeter

Diamond is a radiation hard substance, which has made it a material of choice in for building detectors used in hostile radiation environments. The detectors based on CVD diamonds have been discussed in the chapter on solid state detectors. The dosimeters based on CVD diamond have the same type of structure but they are smaller in size [24].

c. Plastic Scintillator Dosimeter

Scintillators are available in many shapes and forms but for dosimetry purposes the most popular are plastic scintillators. A typical plastic scintillator dosimeter consists of a plastic scintillator, an optical fiber to carry the light photons, and a PMT to count the photons. Sometimes another fiber and a PMT is added to the setup to measure and subtract the background light [24].

However the development of highly efficient light guides and PMTs has made the task simpler than before. Consequently these dosimeters are now gaining popularity.

d. Quartz Fiber Electroscope

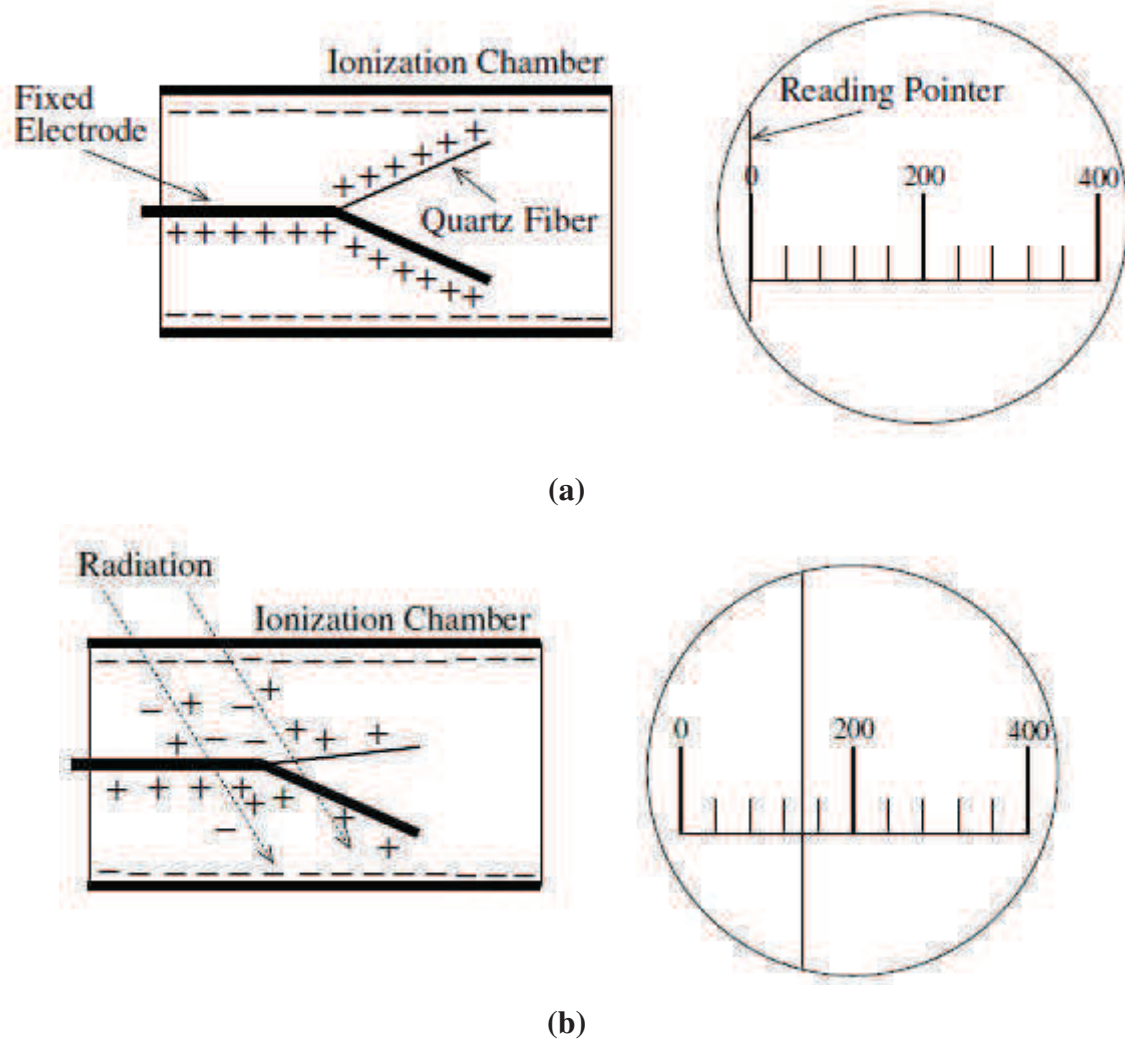


Figure 11.4: (a) Quartz fiber electroscope without any absorbed dose. (b) Incident radiation produces charge pairs in the ionization chamber that decreases the charge on the electrometer pushing the electrodes close together. The eyepiece of the microscope is shown to read a dose of 140 units [24].

Quartz fiber electroscope is a pocket dosimeter that has the capability of instantaneous dose readout. It is therefore generally called a Self-Reading Pocket-Dosimeter or SRPD. It consists of the following main components.

- **Ionization Chamber:** This consists of a very small volume gas filled chamber where the incident radiation produces electron ion pairs.
- **Quartz Fiber Electrometer:** This is used to measure the charge produced by the radiation in the ionization chamber. It consists of a movable quartz fiber and

a metal frame forming its two electrodes. The separation of these electrodes depends on the amount of charge on the metal electrode.

- **Microscope:** The purpose of the microscope is to facilitate the reading of the fiber image.

II.4 Sensors and sensor systems for Industrial and environmental Applications

Background

Sensors and sensor systems are a key underpinning technology for a wide range of applications. They can be used to:

- Improve quality control and productivity in manufacturing processes by monitoring variables such as temperature, pressure, flow and composition
- Help ensure a clean and healthy environment by monitoring the levels of toxic chemicals and gases emitted into watercourses and the air, both in locality, and, via satellites, globally
- Monitor area and regional compliance with environmental standards
- Enhance health, safety and security in the home and workplace through their use in air-conditioning systems, fire and smoke detection and surveillance equipment
- Track the movement of goods at site, local and global scales

CALL TO

Sensors and sensor systems developed for operation in harsh conditions, including those for control and positioning, can be expected to share significant synergies with those required for small satellites, more so as lower cost small satellite solutions are applied to new user applications in Science, the environment and a variety of user services [28]. The wide applicability and multidisciplinary nature of sensor technology also offers scope for the transfer of knowledge and expertise between sectors.

Collaborative Research and Development

A sensor is a device or system that can measure and respond to physical or chemical quantities and can include control and processing electronics, software and interconnection networks. Control systems can incorporate a number of sensing devices working with computer processing capability and actuators to monitor and control processes and products [28].

Application areas can include:

- On-line process monitoring and control
- Quality control
- Condition monitoring
- Remote sensing, including earth observation
- Non-destructive or non-invasive monitoring
- Environmental monitoring and control
- Energy efficiency
- Health, safety and security in the workplace and home (not medical)
- Space

In addition, to individual sensors, sensor arrays and sensor systems incorporating overall automation and control functions. Sensing devices primarily intended for medical applications, e.g. in vivo measurements [28].

Engineer can be based on any advanced sensor technologies including:

- Optics
- Optoelectronics
- Fibre optics
- Acoustics
- Solid-state electrochemistry
- Magnetics
- Micro/nano engineering
- Smart technologies
- Thick and thin film electronics
- Surface acoustic waves

Passive dosimetry				
	TL dosimeters	OSL dosimetry	Film dosimetry	Track etch detectors
The advantages	<ul style="list-style-type: none"> •No Electronics Circuitry. •Small Size: A typical TL dosimeter is less than 5mm long and 2mm wide. •Wide Dynamic Range. 	<ul style="list-style-type: none"> •Faster Processing. •Higher Precision. •High Dynamic Range. •Multiple Readouts. •Shapes and Forms. •Mechanical Stability. 	<ul style="list-style-type: none"> •No Post Irradiation Processing. •High Spatial Resolution. •Good Spatial Uniformity: (typically better than 95%). 	<ul style="list-style-type: none"> •Cost Effectiveness: Due to their low cost. •Good Sensitivity. •Operationally Safe.
The disadvantages	<ul style="list-style-type: none"> •TL dosimeters cannot be used to measure dose rate. •There is no universal TL material that can be used to measure dose from all types of radiation. 	<ul style="list-style-type: none"> •Expensive manufacturing •Fading. •Temperature Dependence 	<ul style="list-style-type: none"> •Fading. •UV Sensitivity. •Film Orientation: The optical density should be measured at the same orientation at which the film was exposed to radiation. 	<ul style="list-style-type: none"> •Track Fading. •Insensitivity to Photons. •Dependence on Etching Rate: The results depend to some extent on the etching process.

Active dosimetry				
	MOSFET Dosimeter	Diamond Dosimeter	Quartz Fiber Electroscop	Plastic Scintillator Dosimeter
The advantages	<ul style="list-style-type: none"> •Small Size: MOSFET dosimeters are very small in size with typical dimension of less than a millimeter. •Good Spatial Resolution. •Good Isotropy. •Large Dynamic Range. •Radiation Type Sensitivity: they can be used for dosimetry of any type of radiation. 	<ul style="list-style-type: none"> •Radiation Hardness: is suitable for use in very high radiation environments. •Stability against Water. •Good Temperature Stability. •Good Isotropy. •Good Energy Response: they can be used over a large dynamic range without the need of correction factors. •Medium-sized. •Good Spatial Resolution. •Tissue Equivalence: this only holds for medical dosimetry applications. 	<ul style="list-style-type: none"> •Visual Readout. •Good Accuracy. •Repeated Usage. •Easy Handling: This device is of the size of a pen and can be carried in a pocket. 	<ul style="list-style-type: none"> •Small Size. •Temperature Stability. •Good Spatial Resolution. •Good Energy Response. •Radiation Hardness. •Good Isotropy. •Large Dynamic Range. •Water Equivalence: This makes them suitable for phantom measurements in clinical dosimetry.
The disadvantages	<ul style="list-style-type: none"> •Sensitivity to Bias Instability. •Radiation Damage. •Temperature Dependence: specially designed double MOSFET devices have shown good temperature stability. 	<ul style="list-style-type: none"> •Dose Rate Dependence: Diamond dosimeters show some dependence on dose rate. •Polarization: If diamond dosimeters are not in a radiation field they tend to become polarized. Therefore to minimize this effect they must be irradiated before being deployed. 	<ul style="list-style-type: none"> •Readout Errors. •Low Dynamic Range. •Low Accuracy. 	<ul style="list-style-type: none"> •They are highly susceptible to background Cherenkov light.

Table I.1: different dosimeter characteristics

I.6 conclusion

Sensor technology is one of the technologies that will play a major role in the future; it can be used in all sectors of industry. Sensors and sensor systems perform a diversity of sensing functions allowing the acquisition, capture, communication, processing and distribution of information. This may be chemical composition, texture and morphology, large-scale structure, positions and also dynamics. Sensor development continues to be an area of science and technology with great growth potential. The sensors and sensor systems have made critical contributions to the exploration of space, military missions, and humanitarian needs. In this chapter a brief overview of the most sensors applied in engineering systems has been presented. Classification of chemical sensors and their applications has been provided. In addition, we presented the different types of radiation sensors and their applications for different engineering areas, as well as the challenges presented in their implementations for practical exploration.

Chapter II

A novel design to deep submicron FET-based chemical sensors

Abstract: In this chapter, a new pH-ISFET sensor, called the Junctionless ISFET sensor (JISFET), and its numerical analysis have been proposed, investigated and expected to improve the fabrication process and the sensitivity behavior for pH-ISFET sensor-based applications. The numerical analysis has been used to predict and compare the performances of the proposed design and conventional pH-ISFET. In addition, a novel multigate sensor is proposed to improve the behavior of the ion-sensitive field-effect transistor (ISFET) sensitivity in deep submicron domain for deep submicroelectronics applications. The proposed structure has been analyzed and validated by the good sensitivity obtained in deep submicron regime. Finally, a new multigate pH-ISFET sensor design, called the Junctionless Gate All Around (GAA) ISFET sensor (JGA AISFET), and its numerical analysis have been proposed, investigated and expected to improve the fabrication process and the sensitivity behavior for pH-ISFET sensor-based applications. The numerical analysis has been used to predict and compare the performances of the proposed design and conventional pH-ISFET, where the comparison of device architectures shows that the proposed pH- JISFET sensor exhibits a superior performance with respect to the conventional pH-ISFET in term of fabrication process and electrical performances. The numerical model provides a basic framework to account for the electronic and chemical performances in future multigate pH-ISFET designs, being easily adaptable to gate structures as the double-gate (DG) or Tri-gate (TG). The obtained results make the proposed chemical sensors a promising candidate for future integrated CMOS-based sensors.

II.1 Introduction

Although the development of clinical sensors has increased in recent years, improvements in sensitivity, selectivity, limits of detection, fast response and miniaturization are yet to be attained. Health care appears to provide the best opportunity for sensor development. Among the wide range of different sensors, electrochemical sensors are the most common in the engineering field, due to their high sensitivity and selectivity, portability, rapid response time and low cost.

Sensors based on field-effect transistors have been focused of interest both from applications and fundamental research point of views. In electronic industry these devices are considered as attractive alternatives for chemical, physiological, nuclear industry, space, radiotherapy and environment monitoring applications due to their rapid time responses, reliability, low power consumption, high dose range, and compatibility to standard CMOS technology and on-chip signal processing [3-6, 29]. The so-called threshold voltage of the transistor is a function of the solution surrounding the gate. The operational mechanism of the ISFET originates from the pH sensitivity of the inorganic gate oxide such as SiO_2 or Ta_2O_5 . Research in multi-gate SOI MOSFETs (MuGFETs) for deep submicron CMOS applications is currently being carried out by many semiconductor manufacturers, as these devices hold the promise for pushing the limits of silicon integration beyond the limits of classical planar technologies.

The Gate All Around GAA MOSFETs have emerged as excellent devices to provide the electrostatic integrity needed to scale down transistors to minimal channel lengths, and allowing a continuous progress in digital and analog applications. Employing this design for chemical and environment monitoring applications becomes more beneficial if the device is made in vertical cylindrical recrystallized silicon due to highly flexible process integration options [37-39].

This chapter is organized as follows. In Section II.2, a new design of pH-ISFET called Junctionless ISFET sensor (pH-JISFET) is proposed for future CMOS-based sensors. In Section II.3, we propose a novel Double Gate (DG) ISFET, to study and improve the sensor sensitivity in deep submicron regime. In Section II.4, we propose a new design of pH-ISFET called Junctionless Gate All Around pH-ISFET sensor (pH-JGAISFET). Finally, section II.5 summarizes some concluding notes.

II.2 A novel multigate design to improve the sensitivity behavior for deep submicron ISFET-based sensors

II.2.1 Derivation of DG ISFET sensitivity model

In this section we propose a novel Double Gate (DG) ISFET, to study and improve the sensor sensitivity in deep submicron regime. Figure I.1. shows the schematic Cross-section view of the proposed DG ISFET structure Derivation of DG ISFET sensitivity model. The proposed study is based on a compact model of drain current by solving a 1-D Poisson's equation with free mobile carrier effect included. The theory illustrates the improved characteristics of DG ISFETs over conventional single gate ISFETs for deep submicron circuit's applications.

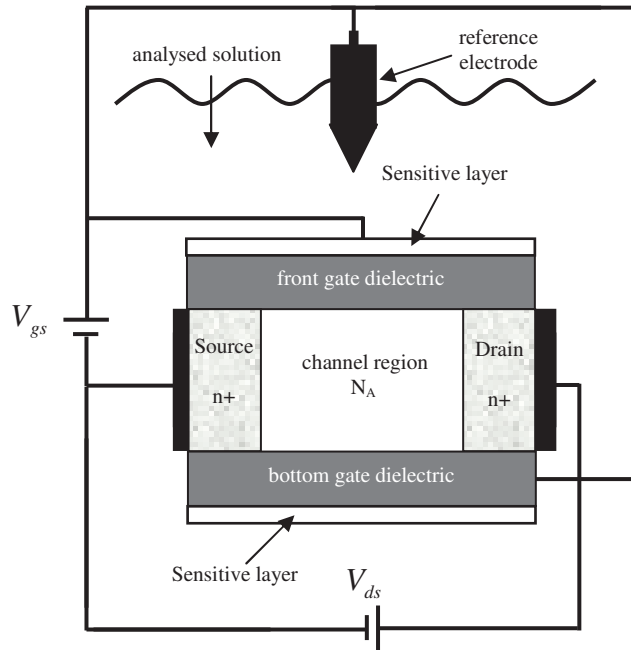
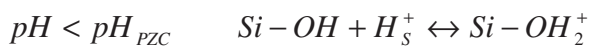


Figure II.1: Cross-section of the proposed DG ISFET structure Derivation of DG ISFET sensitivity model.

According to the site binding theory [5,29], Exchange of the potential determining ions with positive, neutral and negative surface sites of insulating surface SiOH_2^+ , SiOH and SiO^- can be described as follows



$$\text{With } k_a = \frac{[\text{Si-O}^-][H_s^+]}{[\text{Si-OH}]}$$



$$\text{With } k_b = \frac{[\text{Si-OH}_2^+]}{[\text{Si-OH}][H_s^+]}$$

where pH_{PZC} , k_a and k_b are the pH value at the point of zero charge, equilibrium constants of acid point and base point respectively [5]. In respect of the Boltzmann distribution, the surface concentration of hydrogen ions $[H_s^+]$ is given in dependence on the surface potential (ψ_0) and the concentration value of protons in the solution $[H_s^+]$ is:

$$[H_s^+] = [H^+] \exp\left(-\frac{q\psi_0}{kT}\right) \quad (\text{III.1})$$

The surface potential (ψ_0) is dependent on the membrane material and pH value of the electrolyte. The surface potential can be expressed as:

$$\psi_0 = 2.303 \frac{kT}{q} \frac{\beta}{\beta+1} (pH_{PZC} - pH) \quad (\text{III.2})$$

Where k is Boltzmann's constant, T is the temperature of the system, and β is a parameter which reflects the chemical sensitivity of the gate insulator and is dependent on the density of surface hydroxyl groups. It is given by:

$$\beta = \frac{2q^2 N_s \sqrt{K_{OH}}}{C_{DL} kT} \quad (\text{III.3})$$

$$\text{With } K_{OH} = \frac{K_a}{K_b}$$

Where N_s is total number of surface sites per unit area, C_{DL} is a simple capacitance derived by the Gouy-Chapman-Stern model [6]. It is to note that the value of β is essentially depends on the material and technology process used to prepare the ISFET [31-33].

The working of the proposed DG ISFET (Figure II.1) is very similar to that of a DG MOSFET, expect that a solution gate was used instead of a metal gate. Being based to the DG MOSFET model [3], the expression of the ISFET drain-source current (I_{DS}), is given as follow [29]:

$$I_{ds} = \left(\frac{\mu_{eff} W}{L} \right) \left[\frac{q_s^2 - q_d^2}{2n_1} + (q_s - q_d) \right] \quad (\text{III.4a})$$

Where q_s and q_d are the normalized charge at the source and the drain respectively, $n_1 = 1 + \left(\frac{C_{si}}{C_{si} + C_{ox}} \right)$ represents the ideality factor, C_{si} and C_{ox} represent the silicon and oxide capacitance respectively and μ_{eff} represents the effective mobility.

The analytical expression of the normalized charge within the channel is given in [34] as

$$q_I = n_1 \left(1 + \exp \left(V_{gs} - \left(\frac{V_{to}}{n_1} \right) - V_{ch} \right) \right) \quad (\text{III. 4b})$$

V_{t_0} represents the threshold voltage given in [39] as

$$V_{to} = th_1 V_{fb} + th_2 \left(\frac{C_{eq}}{C_{ox}} \right) V_{fb} + th_3 \left(\frac{C_{eq}}{C_{ox}} \right) 2\phi_B + th_4 \left(1 + \left(\frac{C_{eq}}{C_{si}} \right) \right) \left(\frac{qN_A t_{si}}{C_{ox}} \right) \quad (\text{III. 4c})$$

Where $C_{eq} = \frac{C_{si} \cdot C_{ox}}{C_{si} + C_{ox}}$, and ϕ_B , V_{fb} are the barrier and the flat band voltage

respectively. By replacing V_{ch} by the S/D voltage, q_s and q_d can be evaluated.

In the case of DG ISFET, the threshold voltage can be expressed as [29]:

$$V_T (ISFET) = V_T (MOSFET) - \frac{\Phi_M}{q} + E_{ref} + \chi^{sol} - \psi_0 \quad (\text{III. 5})$$

Where E_{ref} is the potential of the reference electrode χ^{sol} is the electrolyte-insulator surface dipole potential and Φ_M is the work function of the metal gate.

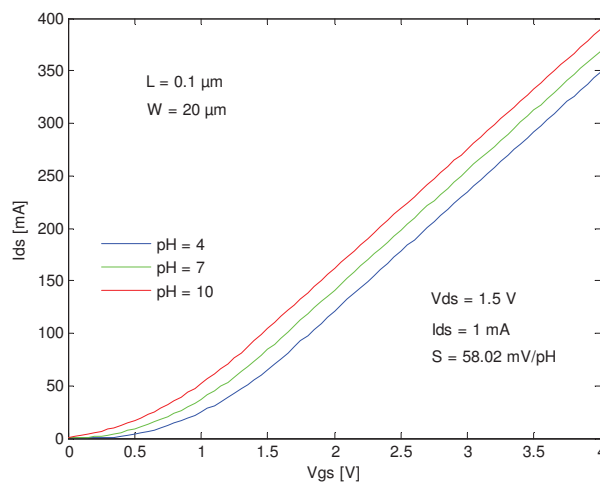
Since V_T can be chemically modified via the interfacial potential at the electrolyte/oxide interface, the $I_{DS} - V_{GS}$ (the drain current versus drain to source voltage) characteristics of the ISFET recorded as a function of pH of the solution, as shown in figure II.2.

The biasing of the DG ISFET at constant drain-to-source current I_{DS0} and voltage V_{DS} allows us the determination of the pH sensor sensitivity [6,31] as:

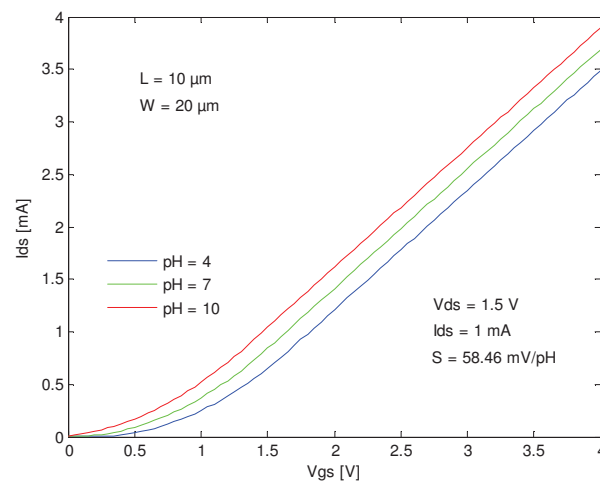
$$S = \frac{\Delta V_T}{\Delta pH} = \frac{\Delta V_{GS}}{\Delta pH} \quad (\text{III. 6})$$

II.2.2 Results and discussions

Since DG ISFET is a sensing device, the input parameter should be threshold voltage, and since threshold voltage can be chemically modified via the interfacial potential at the electrolyte/oxide interface, the current-voltage characteristics are recorded in function of pH values as it is shown in Figure II.2. The pH sensitivity of individual DG ISFET was simulated and analyzed using the analytical expressions developed in section. II. The reference electrode voltage, and the source and sink bias currents were variables parameters. The effect of solution pH on the DG ISFET threshold voltage is clearly seen in Figure II.2.



(a)



(b)

Figure II.2: I-V characteristics as function of pH values for (a) $L=0.1\mu\text{m}$ and (b) $L=10\mu\text{m}$.

This Figure shows the behavior of drain current, I_{DS} , in function of applied gate voltages, V_{GS} , at drain bias, $V_{DS} = 1.5V$, for different channel lengths ($L = 0.1\mu m$ and $L = 10\mu m$). This analysis clearly indicates that the DG ISFET is electronically identical to a conventional DG MOSFET with one additional feature which is the possibility to chemically modify the threshold voltage via the interfacial potential at the electrolyte/oxide interface. In order to study the effect of the DG ISFET scalability on the sensor's sensitivity, we present in Figure II.3 the evolution of the sensitivity behavior as function of channel lengths for both structures Double Gate and Single Gate one. It can be observed that the sensitivity decreases rapidly as the channel length decreases in the case of SG ISFET, where the low recorded value of the sensitivity is $45mV/pH$ for $L=0.1\mu m$ [3]. It also clear that the sensitivity degradation becomes more apparent for very short channel length devices (less than $10\mu m$), which can be explained by the fact that the early and channel length modulation effects take place essentially in the short channel devices domain. Contrary, in case of DG ISFET the value of the sensitivity equals to $58mV/pH$, which is the ideal value of the sensitivity, for wide channel length domain. Consequently, it can be reasonably claimed that the proposed DG ISFET structure can alleviate the critical problem and further improve the immunity of short channel effects of deep submicron CMOS-based sensors for the chemical and biomedical applications [29].

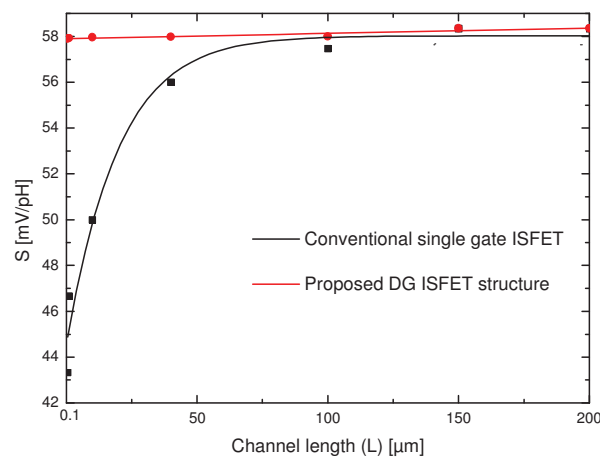


Figure II.3: Variation of the sensor sensitivity for conventional (SG) and DG ISFET as function of channel length.

II.3 Numerical Analysis of Thin Film Junctionless pH-ISFET Sensor

II.3.1 JISFET design and its parameters

The pH-ISFET can be seen as an ions sensor device. The physical treatment of the pH-ISFET attempts to relate the amount of ions concentration and reference voltage applied between the gate, and the body to the amount of inversion or accumulation charges accumulated in the channel [35]. This charge distribution in the channel can then be related to the variation of the threshold voltage for a given drain–source bias and ions concentration. The accumulated charge at the semiconductor/oxide interface, together with the channel electrostatic potential drop, gives rise to a capacitance C_{Si} . Figure II.4 shows a plot of the total, Electrolyte-Insulator-Semiconductor (EIS), capacitance, normalized to the insulator capacitance, as a function of bias voltage and pH values, illustrating the effect of the pH values on C-V characteristics for the depletion and accumulation working modes. The main effect of a change in a pH solution is a shift in the threshold voltage and the total accumulation capacitance. This phenomenon can be modeled according to the site-binding model [37,45]. As a consequence of these shifts, the EIS structure can be used as sensor diode for depletion and accumulation working modes.

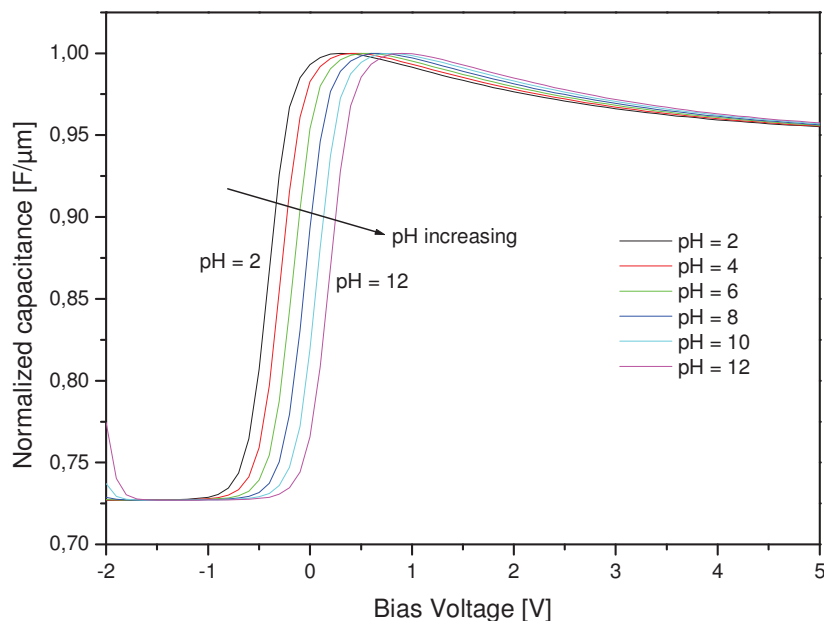


Figure II.4: C–V curves response of the proposed AM-based pH-JISFET for different pH values (from pH=2 to pH=12).

The cross-sectional view of the conventional pH-ISFET and pH-JISFET are shown in Figure II.5. From the figures it is clear that in the case of pH-JISFET design the channel region has the same doping polarity as the source and drain. So, the proposed design has no junctions and less variability in comparison to the conventional pH-ISFET. The device is analyzed with a gate oxide thickness of 10nm. The silicon film thickness is chosen to be very thin layer, 20nm, in order to avoid the shifting of the channel region in the deep of SOI film in the case of Accumulation-Mode design [43]. The channel length for both devices is 350nm which is compatible with CMOS process technology. Also, the incorporation of a high-k HfTiO_3 as sensing membrane deposited on oxide film can improve the sensitivity behavior in comparison with conventional pH-ISFET sensors for wide pH range [45].

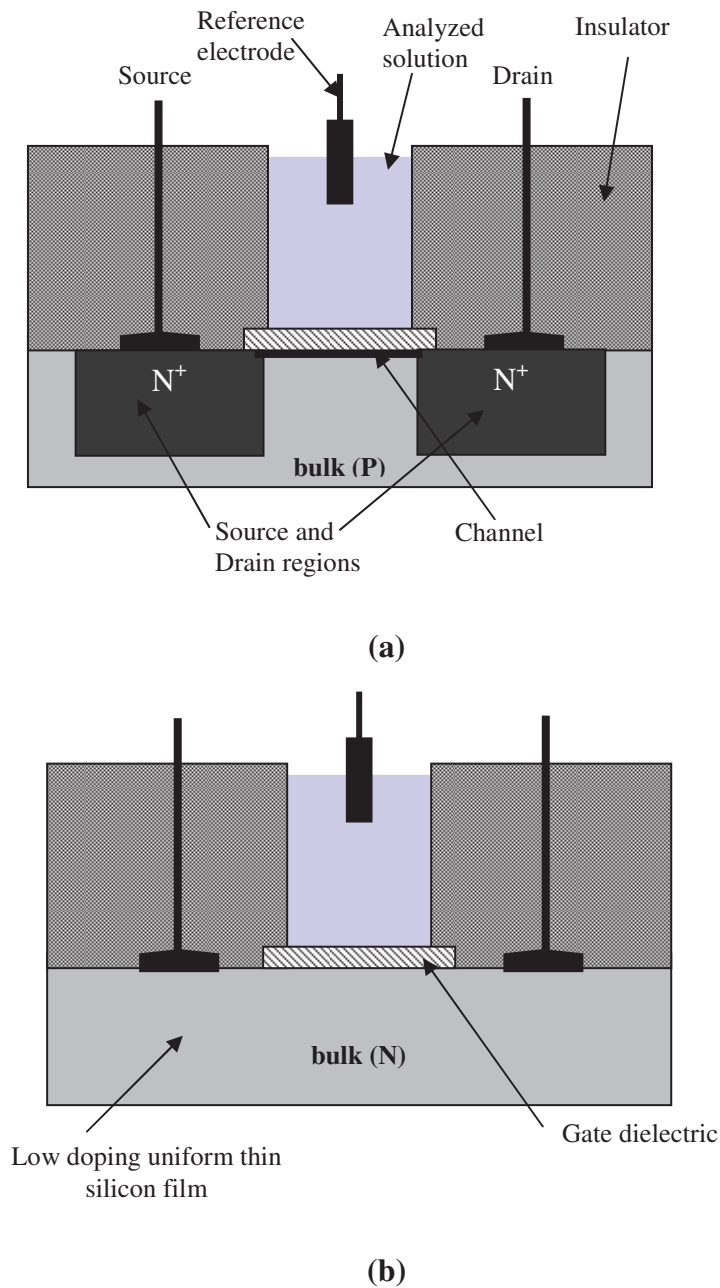


Figure II.5: Longitudinal cross sections showing the doping profiles (a) conventional IM-based pH-ISFET and the (b) Proposed AM-based pH-JISFET.

The electrical parameters of both devices, AM-based JISFET and IM-based ISFET, were analysed using ATLAS 2-D device simulator [46]. The numerical studies are performed to compare the characteristics of the proposed AM-based JISFET structure with conventional IM-based ISFET on the basis electrical and fabricating process performances. The parameters used in our study for both structures are given in Table II.1.

Parameters	IM-based pH-ISFET	AM-based pH-JISFET
Channel doping	$5.10^{16} \text{ cm}^{-3}$ (P-type)	$5.10^{16} \text{ cm}^{-3}$ (N-type)
Source/Drain doping	10^{20} cm^{-3} (N ⁺ -type)	$5.10^{16} \text{ cm}^{-3}$ (N-type)
Silicon thickness (t_{si})	20nm	20nm
Channel length (L)	0.35 μm	0.35 μm
Channel width (W)	1 μm	1 μm
Gate oxide thickness (t_{ox})	10nm	10nm
sensing membrane	high- k HoTiO ₃	high- k HoTiO ₃

Table II.1: Simulation parameters of both devices.

The simulated AM-based JISFET has a uniform doping concentration ($N_D = 5.10^{16} \text{ cm}^{-3}$) throughout the channel and source/drain regions, whereas abrupt source and drain junctions are used for the IM-based ISFET [35]. Appropriate models are used in ATLAS for drift-diffusion model without impact ionization, carrier mobility, recombination-generation and the parameters such as threshold voltage, channel electric field and leakage current compared by changing the pH between 2 and 12 at a constant of drain current of 10 μA for saturation regime and 4 μA for linear domain. It is to note that all computations have been done at room temperature.

II.3.2 Results and discussions

Because of the uniform N-type doping of the channel, the AM-based JISFET requires an appropriate sensing membrane and reference voltage in order to improve the sensor performances and to achieve suitable threshold voltage values for wide concentration range [35]. The transconductance gives the same peak value in a concentration range between pH=2 and pH=12 as shown in Figure II.6.

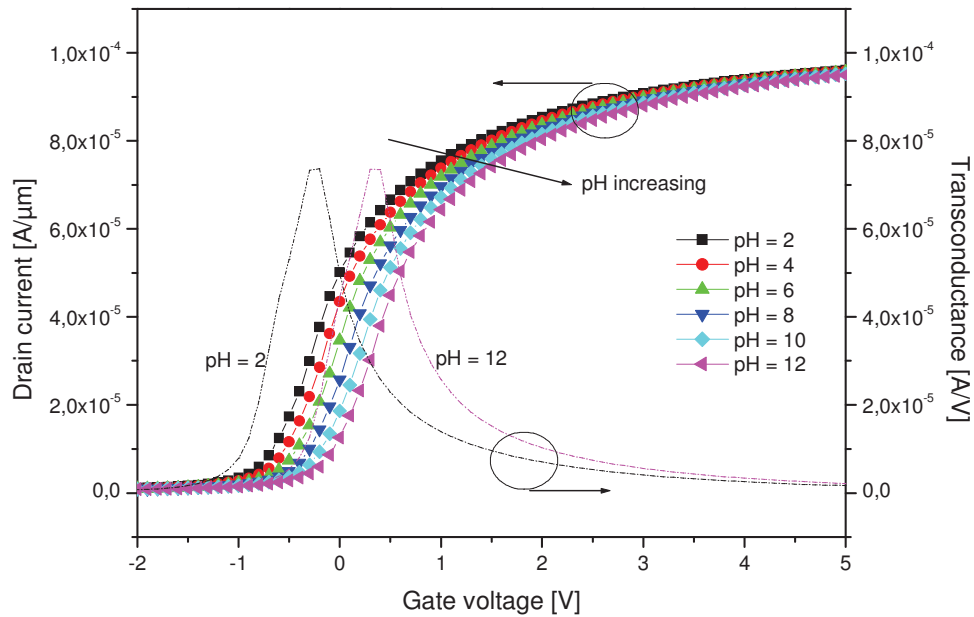


Figure II.6: Curves of the drain current and the transconductance versus bias voltage with different pH values.

The slope of the same I_D versus bias voltage can be obtained around the maximum transconductance. This slope has a concept with bias voltage that is the threshold voltage of AM-based JISFET. Figure II.7 shows that the pH sensitivity of the proposed AM-based JISFET sensor was investigated through the shift in the threshold voltage as a function of pH values. This variation is mainly due to the ionization of the surface hydroxyl groups by either hydrogen ions or hydroxyl ions [35]. To evaluate the sensing performances of the proposed design, we plotted the pH-dependence of the reference voltage for both working regimes (weak and strong accumulation modes). The pH sensitivity and linearity of the AM-based JISFET were about 59.60mV/pH and 0.98 for weak and strong accumulation regimes. The same sensitivity has been recorded in the case of conventional design.

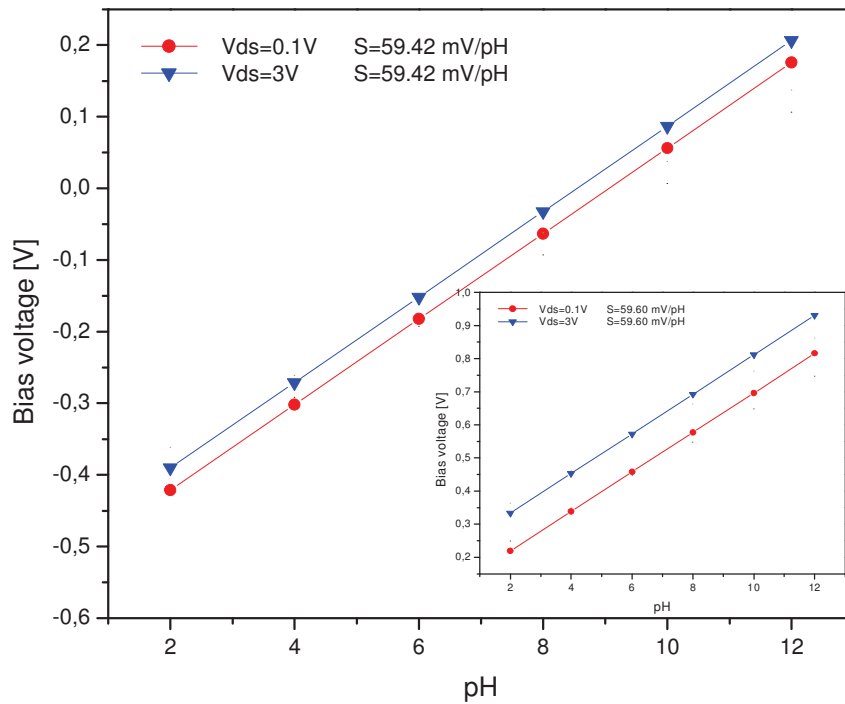


Figure II.7: Bias voltage of the AM-based pH-JISFET as function of pH values. The inset shows bias voltage of the conventional IM-based pH-ISFET as function of pH values for both working regimes (linear and saturation).

Table II.2 shows a comparison of the sensitivities and the electrical performances of both architectures. As can be seen from the table, AM-based JISFET has better electrical performances in comparison with the conventional design [35]. So, our design provides a high sensitivity, better electrical and technological performances in comparison with the conventional structure. These results make the proposed design as a promising candidate for future CMOS-based sensors.

Parameters	Conventional pH-ISFET	pH-JISFET
Output Conductance [A/V]	$3.26 \cdot 10^{-6}$	$1.98 \cdot 10^{-8}$
Off-current [A]	$2.42 \cdot 10^{-5}$	$1.62 \cdot 10^{-5}$
Subthreshold Swing [mV/dec]	92.38	61.58
Threshold voltage [V]	0.07	-0.14
DIBL [mV/V]	1821.90	244.27
Power consumption [mW]	2.30	0.19
Sensitivity [mV/pH]	59.42	59.60
Thermal stability	stable for wide temperature range	stable for wide temperature range
Cost	average	low
Read-out circuit complexity	high	low
Derived current and threshold voltage controllability	low	high

Table II.2: pH sensitivity and electrical characteristics of both devices.

III.4 a Junctionless-multigate design to improve the electrical performances for deep submicron ISFET-based sensors

II.4.1 JGAAISFET design and simulation

Figure II.8 shows the bird's eye view of the proposed JGAAISFETs used in device simulations. Device simulations were performed by the 3-D ATLAS simulator. SOI substrate was used in both conventional planar ISFETs and JGAAISFETs having n-type channels and the same physical parameters. Also, the devices had a low-doped

channel region, say, NA was uniform and $=10^{16} \text{ cm}^{-3}$. The source/drain extension doping profile, for conventional design, was set as Gaussian with the peak concentration of 10^{20} cm^{-3} , and the source/drain lateral doping abruptness was 2.5 nm/dec [47]. The supply voltage was set to be 1 V.

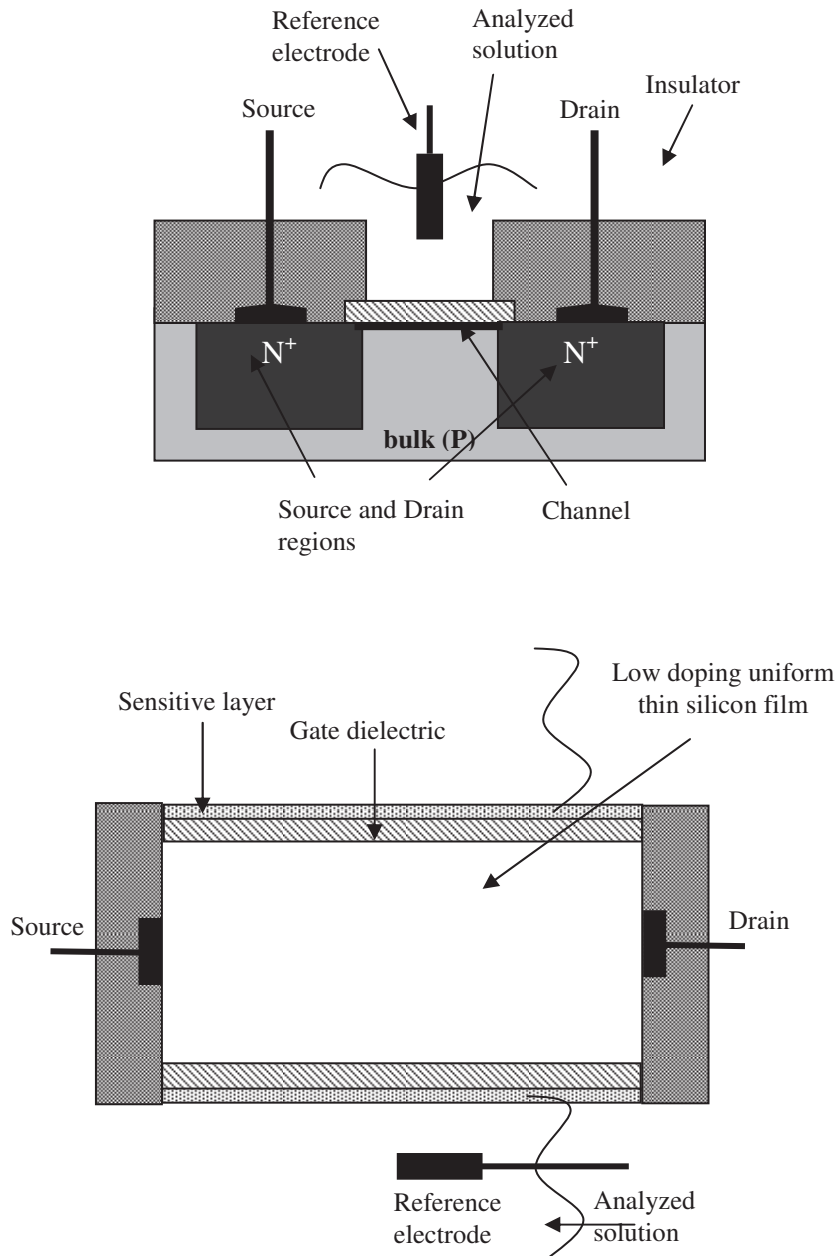


Figure II.8: Longitudinal cross sections showing the doping profiles and channel- designs (a) conventional pH-ISFET and the (b) Proposed pH-JGAISFET.

Simulations were done with various pH values. From Figure II.8 it is clear that in the proposed JGAISFET design the channel region has the same doping polarity as the source and drain. So, the proposed design has no junctions and less variability in

comparison to the conventional pH-ISFET. The device is analyzed with a gate oxide thickness of 10nm. The channel length for both devices, conventional and proposed designs, is 350nm which is compatible with vertical CMOS process technology. Also, the incorporation of a high-k HoTiO_3 as sensing membrane deposited on oxide film can improve the sensitivity behavior in comparison with conventional pH-ISFET sensors for wide pH range [47-49]. The silicon film thickness is chosen to be very thin layer, 20nm, in order to avoid the shifting of the channel region in the deep of SOI film in the case of Accumulation-Mode design [39,47]. In addition, in the proposed design, the physical treatment of the sensor attempts to relate the amount of ions concentration and reference voltage applied between the gate, and the body to the amount accumulation charges accumulated in the cylindrical channel. This charge distribution in the channel can then be related to the variation of the threshold voltage for a given drain–source bias and ions concentration. The accumulated charge at the semiconductor/oxide interface, together with the channel electrostatic potential drop, gives rise to a capacitance C_{Si} .

Figure II.9 shows a plot of the total, Electrolyte-Insulator-Semiconductor (EIS), capacitance, normalized to the insulator capacitance, as a function of bias voltage and pH values, illustrating the effect of the pH values on C-V characteristics for the depletion and accumulation working modes. The parameters used in our analysis for both structures are given in Table II.3.

The analyzed JGAISFET has a uniform doping concentration throughout the channel and source/drain regions, whereas abrupt source and drain junctions are used for the conventional ISFET. Appropriate models are used in ATLAS simulator [46] for Drift-Diffusion model and the parameters such as threshold voltage, channel electric field and leakage current compared by changing the pH between 2 and 12 at a constant of drain current of $10\mu\text{A}$ for saturation regime and $4\mu\text{A}$ for linear domain. It is to note that all computations have been done at room temperature.

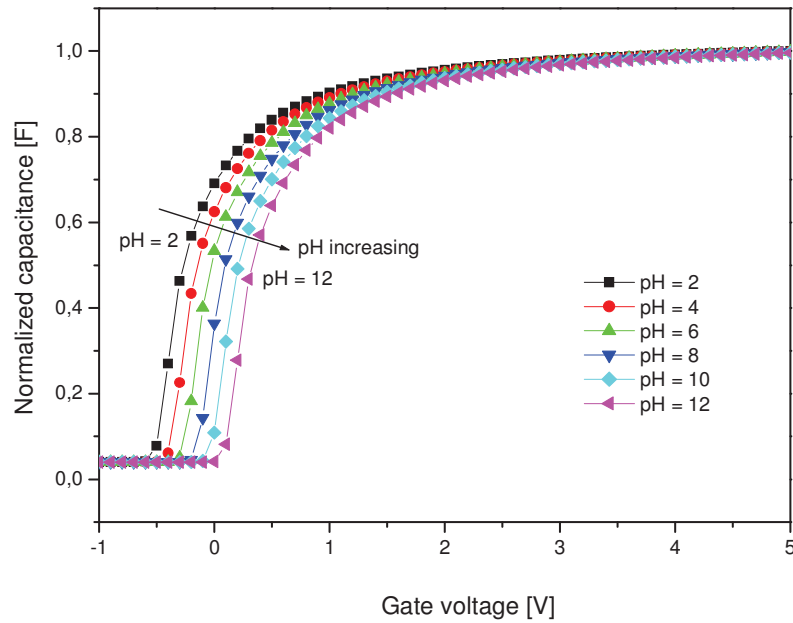


Figure II.9: C–V curves response of the proposed AM-based pH-JGAAISFET for different pH values (from pH=2 to pH=12).

Parameters	pH-ISFET	pH-JGAAISFET
Channel doping	$5.10^{16} \text{ cm}^{-3}$ (P-type)	$5.10^{16} \text{ cm}^{-3}$ (N-type)
Source/Drain doping	10^{20} cm^{-3} (N ⁺ -type)	$5.10^{16} \text{ cm}^{-3}$ (N-type)
Silicon thickness (t_{si})	20nm	20nm
Channel length (L)	$0.35\mu\text{m}$	$0.35\mu\text{m}$
Gate oxide thickness (t_{ox})	10nm	10nm
sensing membrane	high- k HoTiO ₃	high- k HoTiO ₃

Table II.3: Simulation parameters of both devices.

II.4.2 Results and discussions

Since we have a uniform N-type doped channel, the JGAAISFET needs an adequate sensing membrane and reference voltage for the improvement of the sensor performances in addition to the achievement of suitable threshold voltage values for wide concentration interval. Figure II.10 shows the transfer characteristics of the proposed JGAAISFETs. DIBL (Drain Induced Barrier Lowering) was defined as the difference in threshold voltage when the drain voltage was increased from 0.1 to 1 V [47]. The evaluation of this parameter is very important to study the electrical behavior of the sensor in function of dimensions and physical parameters such as channel length and channel doping. In this case, the threshold voltage extraction was performed considering a constant current level of $3\mu\text{A}$.

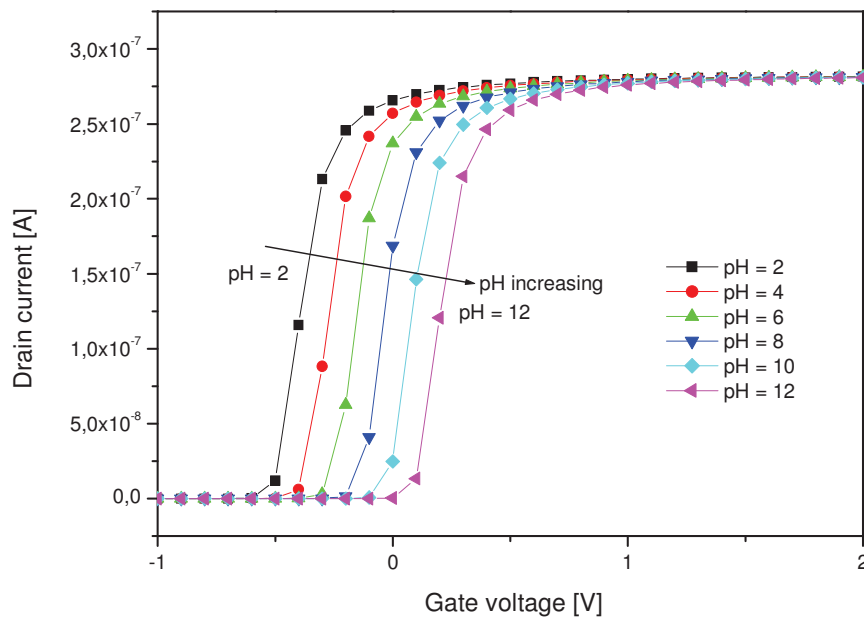


Figure II.10: of the drain current versus bias voltage with different pH values.

From the results in Table II.4, we confirmed that JGAAISFETs had small SS (subthreshold swing) and DIBL as well as a high ON/OFF current ratio in comparison with conventional IFET designs. Moreover, JGAAISFETs had higher transconductance and drift current. In addition low power consumption has been recorded in the case of JGAAISFET design. This means that JGAAISFET has better electrical and scaling performances in comparison with the conventional design [47,49]. So, our design

provides a high sensitivity, better electrical and technological performances in comparison with the conventional structure. These results make the proposed design as a promising candidate for CMOS-based sensors [50-53].

Parameters	Conventional pH-ISFET	pH-JGAAISFET
Output Conductance [A/V]	$4.68.10^{-8}$	$1.68.10^{-11}$
Off-current [A]	$7.14.10^{-7}$	$2.68.10^{-7}$
Subthreshold Swing [mV / dec]	83.6	60.43
Threshold voltage [V]	-0.88	-0.49
DIBL [mV / V]	25.84	0.037
Power consumption [mW]	0.19	$3.13.10^{-3}$
Sensitivity [mV / pH]	59.65	59.65
Thermal stability	stable for wide temperature range	stable for wide temperature range
Cost	average	low
Read-out circuit complexity	high	low
Derived current and threshold voltage controllability	low	high

Table II.4: pH sensitivity and electrical characteristics of both devices.

III.5 Conclusion

In this chapter, a new pH-ISFET, called the Junctionless ISFET sensor (JISFET), based on Accumulation- Mode aspect has been proposed. The proposed sensor has no source and drain junctions, where the concentration and doping type is the same in the channel region and in the source and drain. The performances of the proposed design were compared to the conventional pH-ISFET, illustrating the superior performance of the proposed sensor with respect to the conventional pH-ISFET in terms of fabrication process and electrical performances.

In addition, an analytical analysis for a new DG ISFET structure has been developed. It has been shown that the introduction of the second gate region exhibits an improvement in the screening of the drain potential variation, and reduced the effect of the short-channel-effects on the sensitivity behavior. The law of scaling capability of the proposed structure was compared to the conventional SG ISFET, illustrating the improved sensitivity behavior of the DG ISFET over SG ISFET's. The analytical analysis has been used to predict the sensitivity performances of downscaled ISFETs sensors, where the study shows that the proposed DG ISFET design exhibits a superior performance for short channel domain in terms of threshold voltage and sensitivity behavior.

Finally, we compared new sensor design, pH-JGAAISFET, with conventional planar pH-ISFET through 2-D device simulations. The short-channel effects of the pH-JGAAISFETs were more effectively suppressed than those of the conventional planar pH-ISFET. Also, we confirmed that pH-JGAAISFETs had advantages in CMOS scaling in comparison with planar pH-ISFETs. With continued progress towards fabricating pH-ISFET devices, it is possible to fabricate pH-JGAAISFET without much technological processes. Our numerical analysis provides the incentive for experimental exploration of the pH-ISFETs with Accumulation-Mode and cylindrical-channel aspects.

Chapter III- New monitoring multi-gate sensor (DDGAA) RADFET

Abstract: In this chapter, a new radiation sensitive FET (RADFET) dosimeter design (called the Dual-Dielectric Gate All Around DDGAA RADFET dosimeter) to improve the radiation sensitivity performance and its analytical analysis have been proposed, investigated and expected to improve the sensitivity behavior and fabrication process for RADFET dosimeter-based applications. Analytical models have been developed to predict and compare the performance of the proposed design and conventional (bulk) RADFET, where the comparison of device architectures shows that the proposed design exhibits a superior performance with respect to the conventional RADFET in term of fabrication process and sensitivity performances. The proposed design has linear radiation sensitivities of approximately $95.45\mu V/Gy$ for wide irradiation dose range (from Dose=50Gy to Dose=3000 Gy). Our results showed that the analytical analysis is in close agreement with the 2-D numerical simulation over a wide range of devices parameters. The obtained results make the DDGAA RADFET dosimeter a promising candidate for future integrated CMOS-based dosimeters.

III.1 Introduction

The Gate All Around GAA MOSFETs have emerged as excellent devices to provide the electrostatic integrity needed to scale down transistors to minimal channel lengths, and allowing a continuous progress in digital and analog applications. In addition to a better electrostatics than the conventional bulk MOSFET, the use of these devices have advantages relative to the electronic transport, mainly due to (i) the reduced surface roughness scattering because the lower vertical electric field and (ii) the reduction of the Coulomb scattering because the film is made of undoped/low-doped silicon [51,58-60]. Design and modeling guidelines of GAA MOSFETs have been discussed in previous work [53,58-60]. Employing this design for environment monitoring applications (irradiation measurement) becomes more beneficial if the device is made in vertical cylindrical recrystallized silicon due to highly flexible process integration options. There have been several reports of MOSFETs fabricated in recrystallized silicon for high-density digital integrated circuits [53].

Radiation sensitive MOSFETs (RADFETs) have been focus of interest both from applications and fundamental research point of views. In electronic industry these devices are considered as attractive alternatives for nuclear industry, space, radiotherapy and environment monitoring applications due to their reliability, low power consumption, non-destructive read-out of dosimetric information, high dose range, and compatibility to standard CMOS technology and on-chip signal processing [61-63]. The main RADFET disadvantage is the relatively low sensitivity. In this context, the submicron multi-gate design may be considered as attractive alternative to overcome this disadvantage because of the high electrical performance and reliability provided by the multi-gate structure in comparison with single-gate one. However, as semiconductor devices are scaled into the deep submicron domain, short-channel effects (SCEs) begin to plague conventional planar CMOS-based devices. To avoid the electrical constraints and improve the sensitivity performance, a new design and enhancement of conventional (bulk) RADFET become important. In this chapter, a new design of RADFET called the Dual-Dielectric Gate All Around (DDGAA) RADFET dosimeter, in which the manufacturing processes and sensitivity performances will be greatly improved, is proposed for deep submicron CMOS-based dosimeter applications. The (DDGAA) RADFET dosimeter design presented in this chapter is basically surrounded dual-dielectric layers (SiO_2 and Si_3N_4) with low p-channel (Si) doping concentration. The results showed that the analytical model is in agreement with the 2-D numerical

simulation over a wide range of device parameters. The proposed structure has been analyzed and validated by the good sensitivity and electrical performance obtained in deep submicron regime in comparison with the conventional (bulk) design.

This chapter is organized as follows. In Section 2, we present the main concept related to the conventional (bulk) RADFET device. In Section 3, we derive an analytical interface potential distribution including radiation-induced interface-traps. The threshold voltage shift model can then be determined based on the interface potential model. In Section 4, we investigate the performance of the proposed design. The conclusions will be drawn in Section 5.

III.2 Conventional pMOS dosimeters (RADFETs)

The conventional (bulk) RADFET is a unique radiation dosimeter with a high scale dimension (the dimensions of sensor elements are $\approx 1\text{mm}^2$). The pMOS dosimeter advantages, in comparison with other dosimetric systems, include immediate, non-destructive read out of dosimetric information, extremely small size of the sensor element, the ability to permanently store the absorbed dose, wide dose range, very low power consumption, compatibility with microprocessors, and competitive price (especially if cost of the read out system is taken into account). Figure III.1 shows the using of pMOS dosimeter in radiation therapy [65].

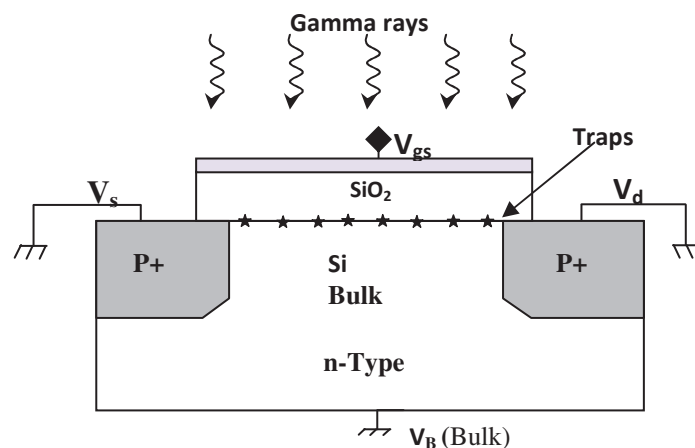


Figure III.1: Cross section of pMOS dosimeter (RADFET) with the defects created by radiation [65]

The main bulk RADFET disadvantages are a need for calibration in different radiation fields ("energy response"), relatively low resolution (starting from about 1 rad) and nonreusability. In this context, the submicron multi-gate design may be considered

as attractive alternative to overcome this disadvantage because of the high electrical performance and reliability provided by the multi-gate structure in comparison with single-gate one. However, as semiconductor devices are scaled into the deep submicron domain, short-channel effects (SCEs) begin to plague conventional planar CMOS-based devices. To avoid the electrical constraints and improve the sensitivity performance, a new design and enhancement of conventional (bulk) RADFET become important [65, 66].

The basic concept of MOS dosimeter is to convert the threshold voltage shift, ΔV_T , induced by radiation, into absorbed radiation dose, D . This dependence can be expressed in the form:

$$\Delta V_T = A \cdot D^n,$$

where $\Delta V_T = V_T - V_{T0}$, V_T is the threshold voltage after irradiation, V_{T0} before radiation, A is a constant, and n is the degree of linearity. n depends on oxide thickness, electric field and absorbed dose.

Ideally, this dependence is linear, i.e $n=1$, and then A represents the sensitivity, S , of MOS dosimeter:

$$S \propto \frac{\Delta V_T}{D} \left(\frac{V}{G_y} \right)$$

The threshold voltage shift ΔV_T is caused by radiation-induced oxide charge and interface traps. Irradiation results in the trapping of holes (generated by the radiation) in the S_iO_2 , and the creation of interface states at the S_i/S_iO_2 boundary. Both the trapped holes and interface states contribute to the ΔV_T in the same direction in the case of pchannel MOS (pMOS) transistors and opposite to each others in the case of n-channel MOS (nMOS).

Namely, the positive oxide trapped charge decreases, but interface traps increases ΔV_T in nMOS transistors, compensating the effect of each others. Both the positive oxide trapped charge and interface traps increase the absolute values of ΔV_T in pMOS transistors [65, 66]. It is reason that pMOS transistors, instead of nMOS transistors, have been used as a radiation dosimeter. It should be noted that the electrons, generated by the radiation, could be also trapped in the oxide, but it is less probable, and the net oxide charge induced by radiation is always positive. The sensitivity increasing to the radiation is one of the main objectives when designing pMOS transistors for radiation dosimetric purposes (called pMOS dosimetric transistors).

III.3 Theory development and model derivation DDGAA RADFET

III.3.1 Interface potential analysis

Schematic cross-sectional view of the proposed (DDGAA) RADFET dosimeter is presented in Figure III.2. The insulator consists of a thermal oxide (SiO_2) grown on a (100) n on n+ epitaxial silicon substrate (channel), and a low pressure CVD silicon nitride layer (Si_3N_4) deposited on top of the oxide. ND/S represents the doping level of the drain/source region, respectively. The channel region is bounded by source and drain spacing at $x=0$ and L , respectively, where L is the gate length. With a negatively applied gate bias, holes generated in the SiO_2 layer are transported and trapped at the SiO_2/Si_3N_4 interface producing a measurable threshold-voltage shift as it is shown in Figure III.2.

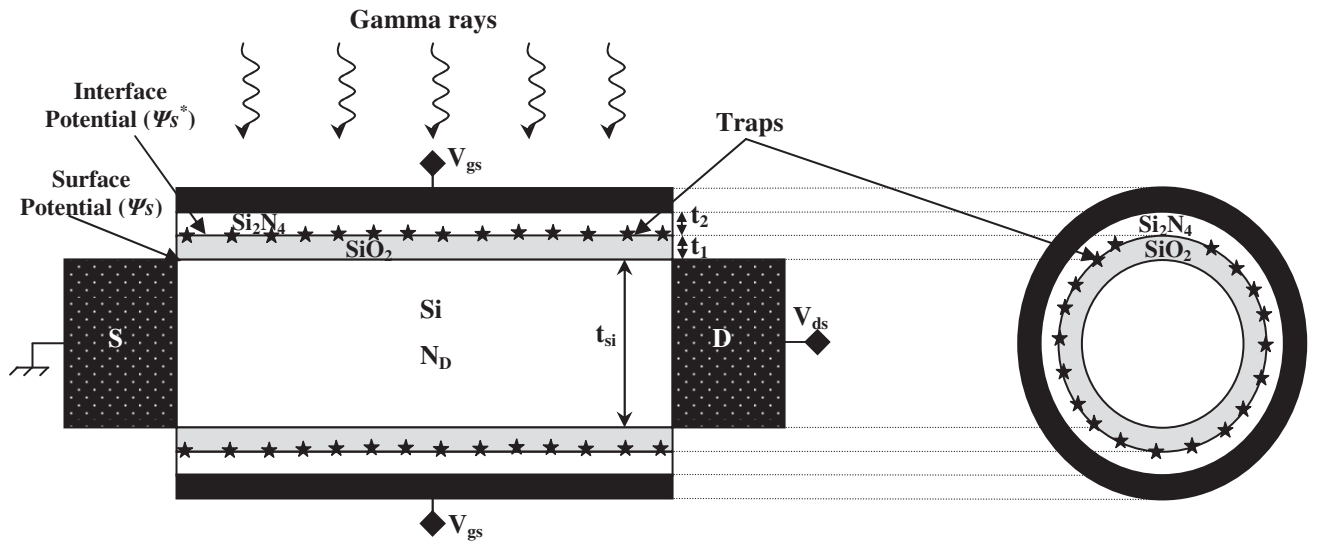


Figure III.2: Cross-sectional view of the proposed DDGAA RADFET design

The investigation reported in this work for gamma radiation sources can also be applied qualitatively to other radiation sources (protons, electrons ...).

For deep submicron devices, the solution of 2D Poisson's equation satisfying suitable boundary conditions is required to model the interface potential. Refer to Figure III.2, the 2D Poisson's equation for the channel region is given by

$$\frac{1}{r} \frac{\partial}{\partial r} \left(r \frac{\partial \psi(r, x)}{\partial r} \right) + \frac{\partial^2 \psi(r, x)}{\partial x^2} = \frac{q \cdot N_D}{\epsilon_{si}} \quad (\text{III. 7})$$

The boundary conditions for $\psi(x, r)$ are found by satisfying continuity of both the normal component of the electric displacement at the (Si/SiO_2) interfaces, and the potential at the source/drain sides.

Using the same parabolic potential profile in vertical direction [51] and applying the symmetry condition of $\frac{\partial \psi}{\partial r} = 0$ for $r=0$, we obtained the following expressions of 2-D channel potential as

$$\psi(r, x) = \frac{C_{ox}}{\epsilon_{si} \cdot t_{si}} [V_g^* - \psi_s(x)] r^2 + \left(1 + \frac{C_{ox} t_{si}}{4\epsilon_{si}}\right) \psi_s(x) - \frac{C_{ox} t_{si}}{4\epsilon_{si}} V_g^* \quad (\text{III. 8})$$

Where $\psi_s(x)$ represents the surface potential (the potential at the Si/SiO_2 interface),

With C_{ox} represents the insulator capacitance ($C_{ox} = \frac{2\pi\epsilon_1 L}{\ln(1 + 2t_1/t_{si})}$), t_{si} is the silicon thickness, the effective oxide and silicon nitride layer is defined as $t_{oxeff} = t_1 + t_2 \frac{\epsilon_1}{\epsilon_2}$ with t_1 is the thickness of the SiO_2 ($\epsilon_1 = \epsilon_{ox}$) layer and t_2 is the thickness of the Si_3N_4 layer (ϵ_2). V_{bi} is the junction voltage between the source/drain and intrinsic silicon, $V_{bi} = (kT/q) \ln(N_{D/S}/n_i)$, n_i is the intrinsic silicon density, V_{ds} represents the drain-to-source voltage and k is the Boltzmann constant. V_g^* represents the effective voltage at the gate which is introduced to simplify notations and alleviate derivations for symmetric structure as $V_g^* = V_{gs} - V_{fb}$, with V_{fb} is the flat-band voltage.

Substituting (2) in (1), we obtain the differential equation that deals only with surface potential as

$$\frac{d^2 \psi_s(x)}{dx^2} - \frac{1}{\lambda^2} \psi_s(x) = D_1 \quad (\text{III. 9})$$

$$\text{With } \lambda = \sqrt{\frac{\epsilon_{si} \cdot t_{oxeff} \cdot t_{si}}{4 \cdot \epsilon_{ox}}} \text{ and } D_1 = \frac{q \cdot N_D}{\epsilon_{si}} - \frac{1}{\lambda^2} \cdot V_g^*$$

Where λ represents the natural length of the analyzed (DDGAA) RADFET dosimeter. This parameter gives the scaling capability (downscaling ability) of the device. D_1 is a factor which represents the impact of the applied gate voltage and channel doping on the surface potential.

The boundary conditions in channel and oxide regions (Figure III.2) are given as,

$$\psi_s(x=0) = V_{bi} \quad (\text{III. 10a})$$

$$\psi_s(x=L) = V_{bi} + V_{ds} \quad (\text{III. 10b})$$

$$\epsilon_2 \frac{V_{gs}^* - \psi_s^*}{t_2} = \epsilon_1 \frac{\psi_s^* - \psi_s}{t_1} \quad (\text{continuity of the normal component of the electric}$$

$$\text{displacement at the interface } SiO_2/Si_3N_4) \quad (\text{III. 10c})$$

Where ψ_s^* represents the interface potential at SiO_2/Si_3N_4 interface which satisfies the continuity of the normal component of the electric displacement at the interface (Eq. III. 10c).

Substituting (III. 10c) in (III. 9), we obtain the differential equation that deals only with interface potential as

$$\frac{d^2 \psi_s^*(x)}{dx^2} - \frac{1}{\lambda^2} \psi_s^*(x) = D_2 \quad (\text{III. 11})$$

$$\text{With } D_2 = \alpha - \beta V_{gs}^* \text{ and } \alpha = \frac{qN_D \epsilon_2 t_1}{\epsilon_{si}(\epsilon_2 t_1 + \epsilon_1 t_2)}, \beta = \frac{\epsilon_2 t_1}{\lambda^2(\epsilon_2 t_1 + \epsilon_1 t_2)}$$

This resolution of this Equation allows us the calculation of the interface potential without (before) irradiation.

In the case of RADFET under irradiation new term should be introduced in order to include the radiation-induced interface-traps effect [51]. So, the parameter D_2 can be written, in this case, as, $D_2 = \alpha - \beta V_{gs}^* - \frac{qN_f}{\epsilon_2 t_2}$, with N_f represents the irradiation induced localized interface charge density per square area. The second term in this expression represents the impact of the irradiation induced localized interface charge density on the interface potential.

Using these boundary conditions (Eqs III. 10a, III. 10b and III. 10c), the surface and interface potentials can be, respectively, expressed as

$$\psi_s(x) = -\lambda^2 D_2 + \frac{\phi_D \sinh\left(\frac{x}{\lambda}\right) - \phi_S \sinh\left(\frac{x-L}{\lambda}\right)}{\sinh\left(\frac{L}{\lambda}\right)} \quad (\text{III. 12})$$

$$\text{With } \phi_D = V_{ds} + \lambda^2 D_2 \text{ and } \phi_S = V_{bi} + \lambda^2 D_2$$

$$\psi_s^*(x) = \frac{\epsilon_1 t_2}{\epsilon_2 t_1 + \epsilon_1 t_2} V_{gs}^* + \frac{\epsilon_2 t_1 x}{\epsilon_2 t_1 + \epsilon_1 t_2} \psi_s(x) \quad (\text{III. 13})$$

III.3.2 Threshold voltage shift model

The basic concept of RADFET dosimeter is to convert the threshold voltage shift, ΔV_{th} , induced by radiation, into absorbed radiation dose, where $\Delta V_{th} = V_{th} - V_{th0}$ with V_{th} and V_{th0} represent the threshold voltage after and before irradiation, respectively.

Based on the surface potential model given by Eq. (III. 12), the threshold voltage can be derived using the condition of the minimum channel potential $\psi_{s\min}|_{V_{gs}=V_{th}} = 2\phi_B$, with $\psi_{s\min} = \psi_s(x_{\min})$, V_{th} is the threshold voltage value, and ϕ_B represents the bulk potential of silicon body given as $\phi_B = (K_B T/q) \ln(N_D/n_i)$ where K_B represents the Boltzmann constant. The location of the minimum surface potential can be obtained analytically by solving $\frac{d\psi_s(x)}{dx} = 0$ [51].

The solution of the equation $\psi_{s\min}|_{V_{gs}=V_{th}} = 2\phi_B$ at low drain-source voltage for long channel lengths ($L \gg \lambda$) can be given as

$$V_{th} = \frac{\left(2A\phi_B + \lambda^2\alpha + \frac{qN_f}{\epsilon_2 t_2}\right) \sinh\left(\frac{L}{\lambda}\right) + (V_{bi} - V_{ds}) \sinh\left(\frac{L}{2\lambda}\right)}{\left(\beta\lambda^2 - \frac{B}{A}\right) \sinh\left(\frac{L}{\lambda}\right) - 2 \sinh\left(\frac{L}{2\lambda}\right)} \quad (\text{III. 14a})$$

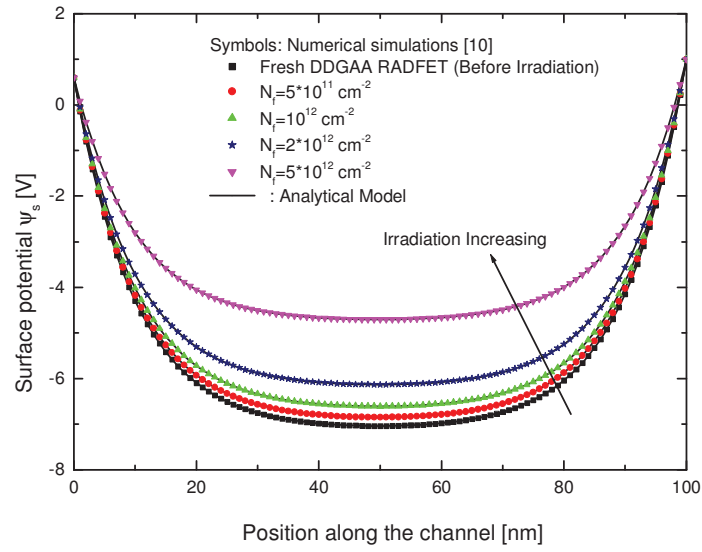
$$\text{with: } A = \frac{\epsilon_1 t_2 - \epsilon_2 t_1}{\epsilon_1 t_2}, \quad B = \frac{\epsilon_2 t_1}{\epsilon_1 t_2}$$

$$V_{th0} = V_{th}|_{N_f=0} = \frac{(2A\phi_B + \lambda^2\alpha) \sinh\left(\frac{L}{\lambda}\right) + (V_{bi} - V_{ds}) \sinh\left(\frac{L}{2\lambda}\right)}{\left(\beta\lambda^2 - \frac{B}{A}\right) \sinh\left(\frac{L}{\lambda}\right) - 2 \sinh\left(\frac{L}{2\lambda}\right)} \quad (\text{III. 14b})$$

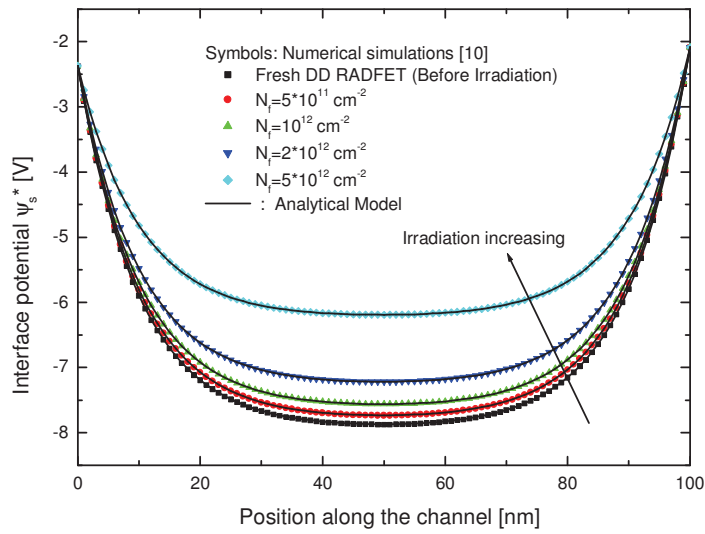
From (III. 14a) and (III. 14b), the threshold voltage shift can be given as

$$\Delta V_{th} = \frac{\frac{qN_f}{\epsilon_2 t_2} \sinh\left(\frac{L}{\lambda}\right)}{\left(\beta\lambda^2 - \frac{B}{A}\right) \sinh\left(\frac{L}{\lambda}\right) - 2 \sinh\left(\frac{L}{2\lambda}\right)} \quad (\text{III. 14c})$$

III.4 Results and discussion



a



b

Figure III.3: (a) Variation of surface potential along the channel (b) Variation of interface potential along the SiO_2/Si_3N_4 interface for different irradiation-induced interfacial traps densities with ($V_{gs} = -5V, V_{ds} = 1V, L = 100nm, t_1 = 5nm, t_2 = 5nm,$

$$\epsilon_1 = 3.9, \epsilon_2 = 7.5, t_{si} = 20nm, N_D = 10^{15} cm^{-3}).$$

Figure III.3 shows the variation of the calculated surface potential (Figure III.3a) and interface potential (Figure III.3b) along the channel for a 100 nm DDGAA RADFET with different interface charges densities N_f at the bias condition $V_{gs} = -5V$ and $V_{ds} = 1V$. It can be seen that a shift (decreasing potential barrier) in the potential profile along the channel, for both surface and interface potentials, as function of the interface charges densities N_f . The shift in the potential profile screens the region near the source end from the variations in drain voltage and thus ensures reduction in short channel effect. In addition, a good uniform increasing of the surface potential as function of the interface charge densities can be observed in Figure III.3a. This surface potential behavior can provide a high threshold voltage sensitivity against the interface charges densities (N_f), which is the main parameter which affects the RADFET sensitivity. Therefore, the proposed design can provide a high sensitivity performance.

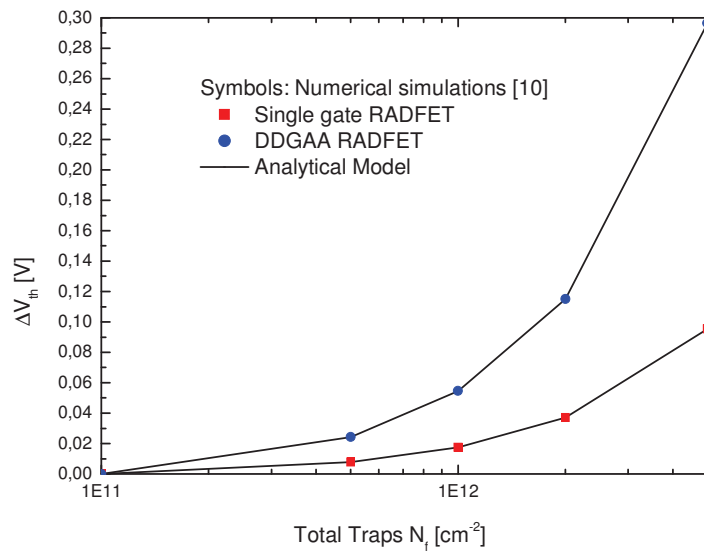


Figure III.4: Threshold voltage shift variation against the irradiation-induced interfacial traps densities for the conventional and DDGAA RADFET designs.

In figure III.4, the variation of threshold voltage shift with different interface charge densities N_f has been compared with conventional bulk (single gate) RADFET. It is shown that the threshold voltage shift values are considerably increased in case of DDGAA RADFET even for interface charge densities more than $6 \cdot 10^{11} cm^{-2}$ [54-57].

Moreover, due to the improved gate controllability, DDGAA RADFET has a higher threshold voltage shift values as compared to conventional RADFET which makes it suitable for high sensitive dosimeter applications.

The RADFET radiation sensitivity, S , given by [63,64]:

$$S = \frac{\Delta V_{th}}{D} \quad (\text{III. 15})$$

Where D represents the absorbed radiation dose.

From an experimental study carried out by A. Jaksic et al [63] an empirical relationship between the interface charge densities, N_f , and the absorbed radiation dose, D , for the silicon material at room temperature can be written as

$$N_f = d_{11}D + d_{12} \quad (\text{III. 16})$$

Where $d_{11} = 1.6 \times 10^9 \text{ cm}^{-2} / \text{Gy}$ and $d_{12} = 5 \times 10^{10} \text{ cm}^{-2}$ are fitting parameters.

Substituting (III. 16) in (III. 14c), we obtain the RADFET sensitivity model that deals only with absorbed radiation dose as

$$S = \frac{\frac{q}{\epsilon_2 t_2} \sinh\left(\frac{L}{\lambda}\right) \left(d_{11} + \frac{d_{12}}{D}\right)}{\left(\beta \lambda^2 - \frac{B}{A}\right) \sinh\left(\frac{L}{\lambda}\right) - 2 \sinh\left(\frac{L}{2\lambda}\right)} \quad (\text{III. 17})$$

In figure III.5, the variation of DDGAA RADFET sensitivity versus the absorbed radiation dose, D , has been compared with conventional (bulk) RADFET. For both designs, the output response of the RADFETs is linear with absorbed radiation dose. It is clearly shown that DDGAA RADFET has higher sensitivity, $S = 95.45 \mu\text{V} / \text{Gy}$, in comparison with conventional RADFET design, $S = 30.68 \mu\text{V} / \text{Gy}$.

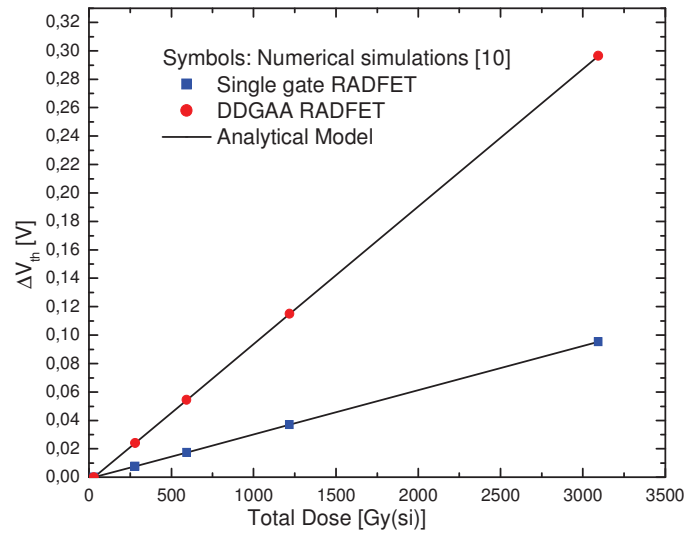


Figure III.5: Variation of threshold voltage shift in function of the absorbed radiation dose for the conventional and DDGAA RADFET designs.

This means that DDGAA RADFET has better electrical and scaling performances in comparison with the conventional design. So, our design provides a high sensitivity, better electrical and technological performances in comparison with the conventional structure. These results make the proposed design as a promising candidate for CMOS-based dosimeters [54].

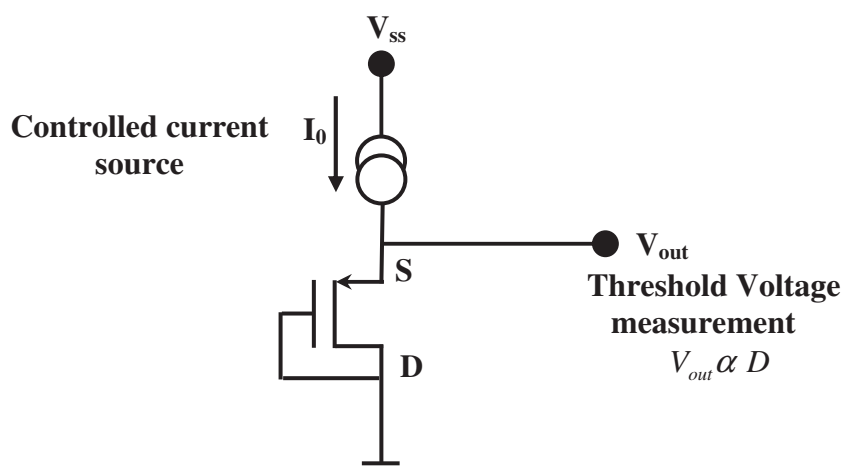


Figure III.6: Set-up for a measurement of V_{th} and absorbed radiation dose (read-out circuit configuration).

Due to the high performance provided by the proposed RADFET design (high sensitivity and threshold voltage linearity); the read of the absorbed radiation dose (D) can be carried out by using a simple Read-out Circuit (RC), as it is shown in figure III.6. In figure III.6, the threshold voltage is measured at a single point of the transfer characteristics, applying a specified current (in the order of ten μA) to the RADFET, while drain and gate are shorted. Due to the simplicity of the Read-out Circuit, the RC configuration is suitable for practical low power applications.

III.5 Conclusion

In this work, we compared new sensor design, DDGAA RADFET, with conventional planar RADFET through 2-D analytical investigation. A two-dimensional analytical analysis comprising radiation-induced interface-traps effect, 2D surface and interface potentials, threshold voltage shift and sensitivity model for DDGAA RADFET has been developed. It has been found that incorporation of the gate all around design leads to an improvement threshold behavior while also enhancing the gate controllability, and thus provides better performance as compared to conventional planar RADFETs. The threshold voltage shift behavior of the proposed design was more effectively improved than those of the conventional planar RADFET. Also, we confirmed that DDGAA RADFET had advantages in CMOS scaling in comparison with planar RADFET.

Moreover, the DDGAA RADFET has a linear sensitivity about $S = 95.45 \mu\text{V} / \text{Gy}$ in radiation dose ranging from $D = 0$ to $D = 3000$ Gy. With continued progress towards fabricating RADFET-based dosimeters, it is possible to fabricate DDGAA RADFET without much technological processes. Our analytical analysis provides the incentive for experimental exploration of the DDGAA RADFETs with around-gate and cylindrical-channel aspects.

Application of the GA-based design approach to DDGAA RADFET has also been discussed. It can be concluded that proposed GA-based approach is efficient and gives the promising results.

Chapter IV-

**Improvement and Implementation of the (DDGAA) RADFET sensor
in radioactive environment**

Abstract: In this chapter, Genetic Algorithm-based approach has been developed to optimize (maximization) the sensor sensitivity. In addition, Image denoising can be described as the problem of mapping from a noisy image to a noise-free image. In this work we attempt to learn this mapping directly with a plain multi layer perceptron (MLP) applied to denoising image. The proposed device and the Artificial Neural Networks (ANNs) have been used to study and show the impact of the proposed dosimeter on the environment monitoring and remote sensing applications. The proposed approach can be used for remote sensing applications. It is to note that our work can be extended to implement the proposed design into Software tools in order to study the engineering systems under radiation conditions.

IV.1 Introduction

Nowadays, artificial intelligence are studied and applied in various disciplines such as neurobiology, psychology, computer science, cognitive science, engineering, economics, medicine, etc. Intelligent Control techniques are recently recognised tools in both academia and industry. Methodologies coming from the field of computational intelligence, such as neural networks, genetic algorithm, can lead to accommodation of more complex processes, improved performance and considerable time savings and cost reductions. Genetic algorithms (GAs), developed by Holland [71], have traditionally used a more domain-independent representation, namely, binary strings. However, many recent applications of GAs have focused on other representations, such as graphs (neural networks), Lisp expressions, ordered lists, and real-valued vectors. A neural network is a way of modeling data based on computer learning. The networks are built from a training dataset where structures in the data are found by the use of algorithms that use no a priori given information. Multilayered perceptron (MLP) networks trained using back propagation (BP) algorithm are the most popular choice in neural network applications. It has been shown that the network can provide satisfactory results. However, MLP network and BP algorithm can be considered as the basis to the neural network studies. The topic of image denoising is an active area of research in image processing and computer vision. However, the goal of noise filtering, or image denoising, is to exploit the available information in the observed image to obtain an estimate of the noise-free information.

This chapter is organized as follows. In Section 2, we present the applicability of genetic algorithm optimization (GA) approach to optimize the radiation sensitivity of the DDGAA RADFET for integrated CMOS-based dosimeters. In Section 3, the proposed dosimeter model was used to study and show the impact of the proposed design on the environment monitoring applications. The conclusions will be drawn in Section 4.

IV.2 GA-based optimization of the radiation sensitivity of DDGAA RADFET

IV.2.1 Genetic algorithms

Genetic algorithms (GAs) are stochastic global search algorithms that form a subset of evolutionary algorithms (EAs). The search method is drawn from the principles of natural selection and population genetics, where the characteristics of individuals are expressed using genotypes. The main driving operator of a Genetic

algorithm is selection (to model survival of the fittest) and recombination through application of a crossover operator (to model reproduction) [70-72].

A genetic algorithm is a search technique used in computing to find exact or approximate solutions to optimization and search problems. Genetic algorithms are a particular class of evolutionary algorithms (also known as evolutionary computation) that use techniques inspired by evolutionary biology such as inheritance, mutation, selection, and crossover (also called recombination). Genetic algorithms are search algorithms based on mechanics of natural selection and natural genetics. In every generation, a new set of artificial creatures or strings is created using bits and pieces of the fittest of the old [70-72].

In the following we present how GAs are different from traditional methods of optimization, how they work, their related techniques, and their vast areas of applications.

IV.2.1.1 How Genetic Algorithms are Different from Traditional Methods?

Genetic algorithms are different from more normal optimization and search procedures, like direct and indirect calculus-based methods, enumerative schemes, random search algorithms etc, in four ways [70,73]:

- A. It works on coding of the parameter set, not the parameters themselves.
- B. It searches from a population of points, not a single point.
- C. It uses objective function information, not the derivative or other auxiliary knowledge.
- D. It uses probabilistic transition rules, not deterministic rules.

Genetic algorithms require the natural parameter set of the optimization problem to be coded as a finite-length string over some finite alphabet. In many optimization methods, we move gingerly from a single point in the decision space to the next using some transitional rule to determine the next point. The point-to-point method is dangerous because it is perfect prescription for locating false peak in multi-modal search spaces. By contrast, genetic algorithm works from a rich database of points simultaneously, climbing many peaks in parallel; thus, probability of finding a false peak is reduced over that go point-to-point.

Many search techniques require much auxiliary information in order to work properly. In contrast, genetic algorithm requires only objective function values associated with individual string. Unlike other methods, genetic algorithms use random

choice as a tool to guide a search toward regions of the search space with likely improvement. These four differences contribute towards genetic algorithms robustness and resulting advantage over other more commonly used techniques.

IV.2.1.2 How Genetic Algorithms Work?

Genetic algorithms are implemented as a computer simulation in which a population of abstract representations (called chromosomes or the genotype or the genome) of candidate solutions (called individuals, creatures, or phenotypes) to an optimization problem evolves toward better solutions. Traditionally, solutions are represented in binary as strings of 0s and 1s, but other encoding are also possible. The evolution usually starts from a population of randomly generated individuals and happens in generations. In each generation, the fitness of every individual in the population is evaluated, multiple individuals are stochastically selected from the current population (based on their fitness), and modified (recombined and possibly randomly mutated) to form a new population. The new population is then used in the next iteration of the algorithm. Commonly, the algorithm terminates when either a maximum number of generations has been produced, or a satisfactory fitness level has been reached for the population. If the algorithm has terminated due to a maximum number of generations, a satisfactory solution may or may not have been reached. A typical genetic algorithm requires two things to be defined [74]:

- ✚ A genetic representation of the solution domain.
- ✚ A fitness function to evaluate the solution domain.

A standard representation of the solution is as an array of bits. Arrays of other types and structures can be used in essentially the same way. The main property that makes these genetic representations convenient is that their parts are easily aligned due to their fixed size that facilitates simple crossover operation. Variable length representations may also be used, but crossover implementation is more complex in this case.

The fitness function is defined over the genetic representation and measures the quality of the represented solution. The fitness function is always problem dependent. For instance, in the knapsack problem we want to maximize the total value of objects that we can put in a knapsack of some fixed capacity. A representation of a solution might be an array of bits, where each bit represents a different object, and the value of the bit (0 or 1) represents whether or not the object is in the knapsack. Not every such

representation is valid, as the size of objects may exceed the capacity of the knapsack. The fitness of the solution is the sum of values of all objects in the knapsack if the representation is valid or 0 otherwise. In some problems, it is hard or even impossible to define the fitness expression; in these cases, interactive genetic algorithms are used. Once we have the genetic representation and the fitness function defined, GA proceeds to initialize a population of solutions randomly, and then improve it through repetitive application of mutation, crossover and selection operators.

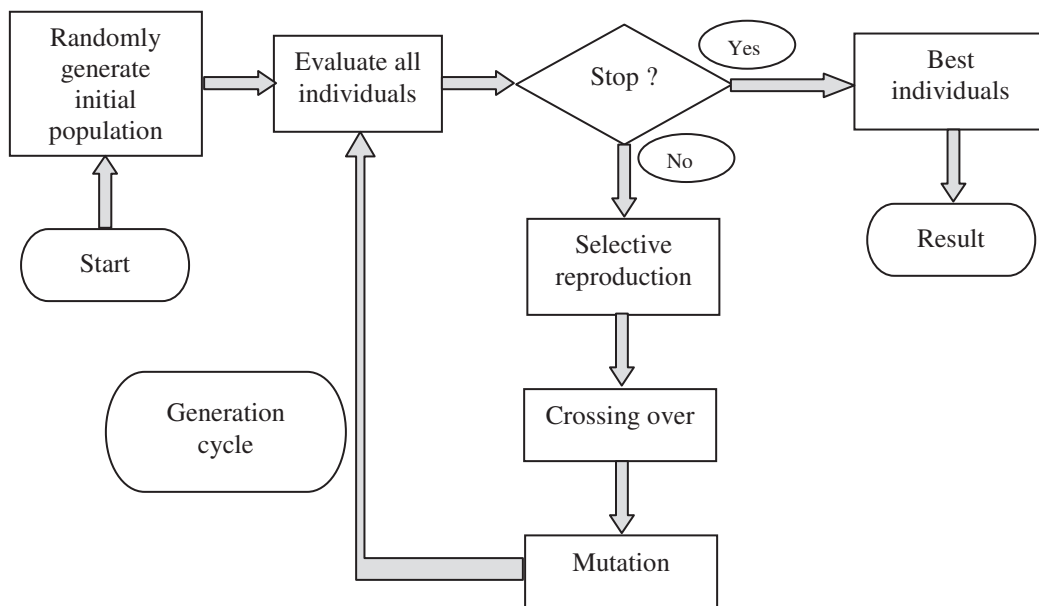


Figure IV.1: Flow Diagram of Genetic Algorithm [70]

IV.2.1.3 Basic steps of genetic algorithms

- Initialization of the population

Initialization involves setting the parameters for the algorithm, creating the scores for the simulation, and creating the first generation of chromosomes. In this benchmark, seven parameters are set:

- The genes value (Genes) is the number of variable slots on a chromosome;
- The codes value (Codes) is the number of possible values for each gene;
- The population size (PopSize) is the number of chromosomes in each generation;
- Crossover probability (CrossoverProb) is the probability that a pair of chromosomes will be crossed;
- Mutation probability (MutationProb) is the probability that a gene on a chromosome will be mutated randomly;

- the maximum number of generations (MaxGenerations) is a termination criterion which sets the maximum number of chromosome populations that will be generated before the top scoring chromosome will be returned as the search answer; and
- The generations with no change in highest-scoring (elite) chromosome (GensNoChange) is the second termination criterion which is the number of generations that may pass with no change in the elite chromosome before that elite chromosome will be returned as the search answer.

- Selection

Selection is the process of determining the number of times, or a trial, a particular individual is chosen for reproduction and, thus, the number of offspring that an individual will produce. The selection of individuals can be viewed as two separate processes [75,76]:

- 1) Determination of the number of trials an individual can expect to receive, and
- 2) Conversion of the expected number of trials into a discrete number of offspring.

There are many methods how to select the best chromosomes, for example roulette wheel selection, Boltzman selection, tournament selection, rank selection, steady state selection and some others.

- Crossover (Recombination)

The basic operator for producing new chromosomes in the GA is that of crossover. Like its counterpart in nature, crossover produces new individuals that have some parts of both parent's genetic material. The simplest form of crossover is that of single-point crossover [75,76]. There are many variations on crossover, for example multi-point crossover, Uniform crossover, and some others. An example of two-point crossover method is given in Figure IV.2.

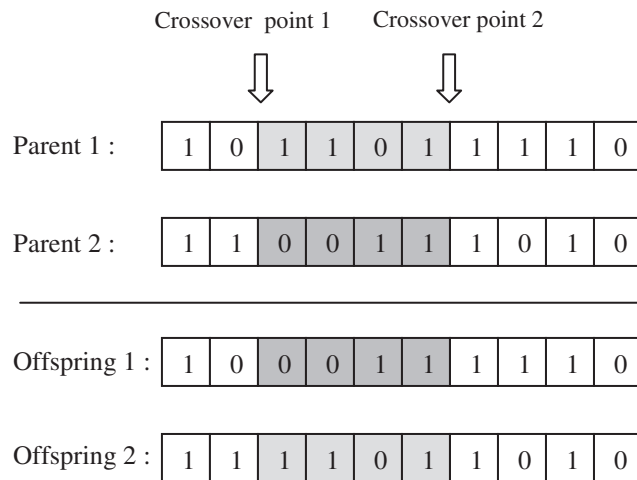


Figure IV.2: Two-point Crossover

- Mutation

In natural evolution, mutation is a random process where one allele of a gene is replaced by another to produce a new genetic structure. In GAs, mutation is randomly applied with low probability, typically in the range 0.001 and 0.01, and modifies elements in the chromosomes. Usually considered as a background operator, the role of mutation is often seen as providing a guarantee that the probability of searching any given string will never be zero and acting as a safety net to recover good genetic material that may be lost through the action of selection and crossover [76].

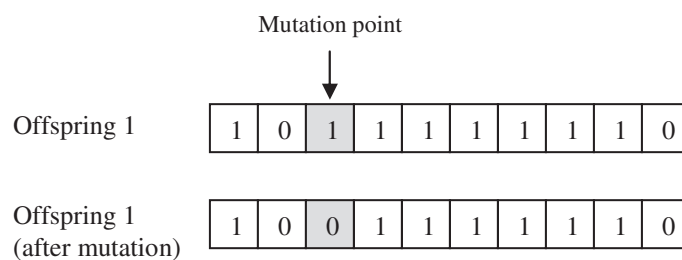


Figure IV.3: Mutation Operator

- Replacement

After the new offsprings are created with crossover and mutation operators, it is time to form up the successor generation. Recall that parent chromosomes were selected according to their fitness, so it is expected that the offsprings increase the fitness of the population generation by generation. Through replacement, genetic algorithm decides whether offspring will survive or will become exist. Some of the most common replacement techniques are explained below.

- Complete Replacement

This technique deletes all the members of the predecessor population and replaces them with the same number of new chromosomes that have just been created.

- Steady-state

In this technique, n old members are chosen in the population and replaced with “n” new members. The choice of the number “n” and the decision of which members to delete from the current population are important aspects of genetic algorithm.

- Replacement with elitism

This technique is same as complete replacement except that this time one or two chromosomes with the highest fitness are chosen to next generation. By this way, good solutions are preventing from become extinct.

IV.2.2 GA-based sensitivity optimisation

GA optimization has been defined as finding a vector of decision variables satisfying constraints to give acceptable values to objective function. It has recently been introduced to study the complex and nonlinear systems and has found useful applications in engineering fields. Due to the simple mechanism and high performance provided by GA for global optimization, GA can be applied to find the best design of DDGAA RADFET in order to improve the radiation sensitivity by satisfying of the following objective function:

- Maximization of the RADFET radiation sensitivity $S(X)$

Where X represents the input normalized variables vector which is given as $X = (t_{si}, t_1, t_2, L)$.

For the purpose of GA-based optimization of the radiation sensitivity of DDGAA RADFET, routines and programs for GA computation were developed using MATLAB 7.2 and all simulations are carried out on a Pentium IV, 3GHz, 1GB RAM computer. For the implementation of the GA, tournament selection is employed which selects each parent by choosing individuals at random, and then choosing the best individual out of that set to be a parent. Scattered crossover creates a random binary vector. It then selects the genes where the vector is unity from the first parent, and the genes where the vector is zero from the second parent, and combines the genes to form the child [66-69]. An

optimization process was performed for 20 population size and maximum number of generations equal to 200, for which stabilization of the fitness function was obtained.

The steady decrease in objective function in each generation until it reaches a best possible value can be attributed to the selection procedure used namely Roulette wheel selection.

The radiation sensitivity values of the DDGAA RADFET with and without optimization are shown in Table IV.1.

Symbol	OPTIMIZED DESIGN	Design without optimization	Conventional design
L(nm)	100	100	100
tsi(nm)	50	20	20
t1(nm)	5	5	5
t2(nm)	15	5	-
S(μ V/Gy)	162.22	95.45	30.68

Table IV.1: DDGAA RADFET Design Parameters

It is clearly shows that the radiation sensitivity, for optimized design (162.22 μ V/Gy) is better than the both conventional RADFET ($S = 30.68\mu V / Gy$) and DDGAA RADFET without optimization ($S = 95.45\mu V / Gy$).

IV.3 Radioactive environment sensing

In order to show the impact of the proposed design on the radioactive environment monitoring, we propose the study of a contemned radioactive environment. This latter is considered a big challenge in the field of the environment monitoring. In this work, using simulated database (built from numerical data) of total dose radioactivity distribution in 2-D space and the Multi-Layer-Perception (MLP) tool, we will study a contemned environment by gamma radiation.

The energy recorded by the sensor has to be transmitted, often in electronic form, to a receiving and processing station, where the data are processed into an image. Radiation that is not absorbed or scattered in the atmosphere can reach and interact with the Earth's surface. There are three forms of interaction that can take place when energy strikes, or is incident upon the surface [80].

In remote sensing, we are most interested in measuring the radiation reflected from targets [80]. This reflection disgusting the image caption by the sensors (which are located at reception stations), we propose that interacting energy (noise) is a Gaussian noise.

Artificial neural network (ANN) based methods have been widely used for modeling various complex and nonlinear processes (classification, speech recognition, and signal processing). The model based on artificial neural network assumes that input and output patterns of a given problem are related by a set of neurons organized in hidden layers [76-78]. The layers in these networks are interconnected by communication links that are associated with weights that dictate the effect on the information passing through them. These weights are determined by the learning algorithm.

The output of node j in the hidden layer is given by

$$h_j = g\left(\sum_{i=1}^n w_{ij} \cdot x_i + b_j\right)$$

And the output of the network by

$$y = \sum_{i=1}^k w_{oi} \cdot h_i$$

Where w_{ij} are the weights connecting the inputs to node j in the hidden layer, b_j is the bias to the node, and w_{oi} are the weights from the hidden to the output layer.

The activation function relates the output of a neuron to its input based on the neuron's input activity level. Some of the commonly used functions include: the threshold, piecewise linear, sigmoid, tangent hyperbolic, and the Gaussian function [81]. The learning process of the MLP network involves using the input–output data to determine the weights and biases. One of the most techniques used to obtain these parameters is the back-propagation algorithm [76-78]. In this method, the weights and biases are adjusted iteratively to achieve a minimum mean square error between the network output and the target value.

IV.3.1 Multilayered perceptron (MLP) networks

MLP networks are feed forward neural networks with one or more hidden layers.

A MLP network with two hidden layers is shown in Figure IV .4. The input layer acts as an input data holder that distributes the input to the first hidden layer. The outputs

from the first hidden layer then become the inputs to the second layer and so on. The last layer acts as the network output layer [77].

A hidden neuron performs two functions that are the combining function and the activation function. The output of the j^{th} neuron of the k^{th} hidden layer is given by

$$v_j^k(t) = F\left(\sum_{i=1}^{n_{k-1}} w_{ij}^k v_i^{k-1}(t) + b_j^k\right); \quad \text{for } j \leq n_k \quad (\text{IV.1})$$

and if the m^{th} layer is the output layer then the output of the l^{th} neuron \hat{y}_l of the output layer is given by

$$\hat{y}_l(t) = \sum_{i=1}^{n_{m-1}} w_{ij}^m v_i^{m-1}(t); \quad \text{for } l \leq n_o \quad (\text{IV.2})$$

where n_k , n_o w's, b's and $F(\cdot)$ are the number of neurons in k -th layer, number of neurons in output layer, weights, thresholds and an activation function respectively.

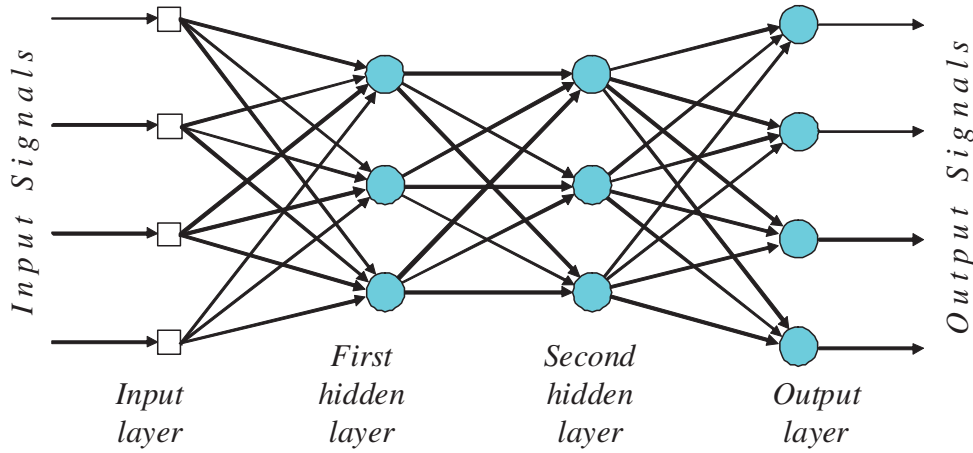


Figure IV.4: Multilayered perceptron networks with two hidden layers [77]

In the current study, the network with a single output node and a single hidden layer is used, i.e $m = 2$ and $n_o = 1$. With these simplifications the network output is:

$$\hat{y}(t) = \sum_{i=1}^{n_l} w_i^2 v_i^1(t) = \sum_{i=1}^{n_l} w_i^2 F\left(\sum_{j=1}^{n_r} w_{ij}^1 v_j(t) + b_i^1\right) \quad (\text{IV.3})$$

Where n_r is the number of nodes in the input layer. The activation function $F(\cdot)$ is

$$\text{selected to be } F(v(t)) = \frac{1}{1 + e^{-v(t)}} \quad (\text{IV.4})$$

The weights w_i and threshold b_j are unknown and should be selected to minimise the prediction errors defined as

$$\varepsilon(t) = y(t) - \hat{y}(t) \quad (\text{IV.5})$$

Where $y(t)$ is the actual output and $\hat{y}(t)$ is the network output.

IV.3.2 Training Algorithm

Back propagation algorithm is the steepest decent type algorithm where the weight connection between the j^{th} neuron of the $(k-1)^{\text{th}}$ layer and the i^{th} neuron of the k^{th} layer are respectively updated according to

$$\begin{aligned} w_{ij}^k(t) &= w_{ij}^k(t-1) + \Delta w_{ij}^k(t) \\ b_i^k(t) &= b_i^k(t-1) + \Delta b_i^k(t) \end{aligned} \quad (\text{IV.6})$$

with the increment $\Delta w_{ij}^k(t)$ and $\Delta b_i^k(t)$ given by

$$\begin{aligned} \Delta w_{ij}^k(t) &= \eta_w \rho_i^k(t) v_j^{k-1}(t) + \alpha_w \Delta w_{ij}^k(t-1) \\ \Delta b_i^k(t) &= \eta_b \rho_i^k(t) + \alpha_b \Delta b_i^k(t-1) \end{aligned} \quad (\text{IV.7})$$

where the subscripts w and b represent the weight and threshold respectively, α_w and α_b are momentum constants which determine the influence of the past parameter changes on the current direction of movement in the parameter space, η_w and η_b represent the learning rates and $\rho_i^k(t)$ is the error signal of the i^{th} neuron of the k^{th} layer which is back propagated in the network [77,78]. Since the activation function of the output neuron is linear, the error signal at the output node is

$$\rho^m(t) = y(t) - \hat{y}(t) \quad (\text{IV.8})$$

And for the neurons in the hidden layer

$$\rho_i^k(t) = F'(v_i^k(t)) \sum_j \rho_j^{k+1}(t) w_{ji}^{k+1}(t-1) \quad k = m-1, \dots, 2, 1 \quad (\text{IV.9})$$

Where $F'(v_i^k(t))$ is the first derivative of $F(v_i^k(t))$ with respect to $v_i^k(t)$.

Since back propagation algorithm is a steepest decent type algorithm, the algorithm suffers from a slow convergence rate. The search for the global minima may become trapped at local minima and the algorithm can be sensitive to the user selectable parameters.

IV.3.3 Adaptive noise filtering using Back Propagation Neural Network

Consider the signal transmitted through the noisy channel gets corrupted with the noise. The corrupted signal is given as the input to the BPNN filter as given below to filter the noisy part of the signal [79].

Let $x(n)$ be the noisy corrupted input signal to the system, $y(n)$ be the output signal of the system which is the filtered signal and $h(n)$ is the impulse response of the system. They are related mathematically as given below.

$$y(n) = x(n) * h(n) \Rightarrow y(n) = \sum_{k=0}^{N-1} h(k) * x(n-k)$$

‘*’ is the convolution operator. ‘N’ is the order of the filter. For instance if the order of the filter is 11,

$$y(n) = h(0)x(n) + h(1)x(n-1) + h(2)x(n-2) + h(3)x(n-3) + h(4)x(n-4) + \dots + h(10)x(n-10)$$

The $h(0)$, $h(1)$, ... $h(10)$ are the impulse response of the system, otherwise called as the filter coefficients of the system.

Obtaining the values of the filter coefficients is the task involved in designing the digital filter to do specific operation. To obtain the values there is the need to study about the nature of the noise of the channel [79].

In practical situations the reference signal is sent through the channel and the corresponding corrupted signal obtained as the output of the channel is stored. These are used for determining the filter coefficients of the FIR filter. Once filter coefficients are obtained, they are used to filter the real time noisy signal corrupted due to channel transmission at the receiver side.

Filter block is the Back propagation Neural Network block to perform filtering operation as described below. In this experiment the reference signal and its corresponding corrupted signal are assumed to be known.

IV.3.3.1 Approach

Step 1: Back propagation neural network is constructed with 11 input Neurons and 1 output neuron and 5 Hidden neurons

Step 2: In signal processing point of view, input of the neural network is the corrupted signal and the output of the neural network is the filtered signal.

Step 3: During the training stage, the elements of the Input vectors are the samples collected from the corrupted reference signal. Similarly element of the output vector is the corresponding sample collected from the reference signal.

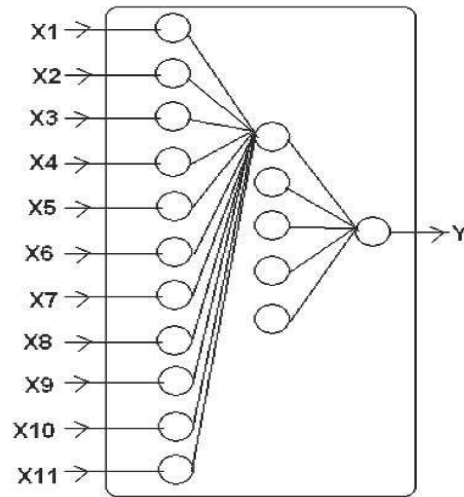


Figure IV.5 : BPNN Filter Structure [79]

x1	x2	x3	x4	x5	x6	x7	x8	x9	x10	x11	Y
X(10)	X(9)	X(8)	X(7)	X(6)	X(5)	X(4)	X(3)	X(2)	X(1)	X(0)	Y(0)
X(11)	X(10)	X(9)	X(8)	X(7)	X(6)	X(5)	X(4)	X(3)	X(2)	X(1)	Y(1)
X(12)	X(11)	X(10)	X(9)	X(8)	X(7)	X(6)	X(5)	X(4)	X(3)	X(2)	Y(2)
...											
X(16)	X(15)	X(14)	X(13)	X(12)	X(11)	X(10)	X(9)	X(8)	X(7)	X(6)	Y(16)
X(17)	X(16)	X(15)	X(14)	X(13)	X(12)	X(11)	X(10)	X(9)	X(8)	X(7)	Y(17)
X(18)	X(17)	X(16)	X(15)	X(14)	X(13)	X(12)	X(11)	X(10)	X(9)	X(8)	Y(18)
X(19)	X(18)	X(17)	X(16)	X(15)	X(14)	X(13)	X(12)	X(11)	X(10)	X(9)	Y(19)
X(20)	X(19)	X(18)	X(17)	X(16)	X(15)	X(14)	X(13)	X(12)	X(11)	X(10)	Y(20)
...											

Table IV.2: Sample Hetero Association table relating input vectors and output vectors of the BPNN [79]

The Hetero association table relating the sample input vector and the corresponding output vector used for training the constructed ANN is given below. Note that x is the corrupted reference signal and y is the reference signal [79].

Step 4: Train the Artificial Back propagation Neural Store the Weights and Bias.

Step 5: Now the BPNN filter is ready to filter the original corrupted signal.

IV.3 4 Result and discussion:

In this work, the artificial neural network is used to denoising the image distorted by the transmission noise (Figure.IV.6). In this context, the database for MLP optimization consists of 49600 samples split into three categories: training, validation and test sets. The training and validation are used tune MLP configuration and the test is used to test the MLP configuration to denoise the different regions of the contemned

environment. Test and training steps were run for a given MLP structure to obtain the optimal MLP configuration. The database is collected from several RADFETs, which have been located in different regions in the contaminated environment. In order to validate the denoising proprieties of the optimized MLP, test set is compared to the MLP response.

Figure IV.7 presents the space distribution of the gamma radiation in the investigated contaminated environment after the denoising process. It is shown that the different regions are clearly represented. This last observation shows the applicability and the efficiency provided by the MLP-based approach to study the radioactive environment.

Figure IV.8 shows that a good agreement between MLP and real results is found. Hence, the optimized structure can be used for the radioactive environment monitoring applications.



Figure IV.6: The distorted image due to the transmission noise



Figure IV.7: The denoised image using MLP

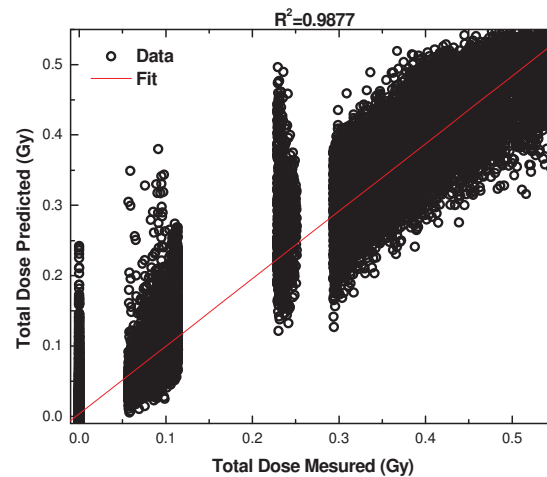


Figure IV.8: Validation of the neural network result for test set

IV.4 Conclusion

In this chapter, Application of the GA-based design approach to DDGAA RADFET has been discussed. It can be concluded that proposed GA-based approach is efficient and gives the promising results. In order to show the impact of the proposed design on the radioactive environment monitoring, we developed a MLP-based approach to study a contemned radioactive environment. BP is used to train MLP networks to perform system identification. The work suggests that the network trained using BP algorithm give a good result. The proposed approach can be used for remote sensing applications, where the information about the contemned radioactive environment should be transmitted in electronic form to a receiving and processing station. It is to note that our work can be extended to implement the proposed design into Software tools in order to study the engineering systems under radiation conditions.

Conclusions and future work

In this thesis, an extensive work is carried out in the field of FETs sensor modeling. We proposed a novel multigate design to improve the sensitivity behavior for deep submicron ISFET-based sensors where an analytical analysis was developed, it has been shown that the introduction of the second gate region exhibits an improvement in the screening of the drain potential variation, and reduces the short-channel-effects on the sensitivity behavior. The law of scaling capability of the proposed structure was compared to the conventional SG ISFET, illustrating the improved sensitivity behavior of the DG ISFET over SG ISFET's. The analytical analysis has been used to predict the sensitivity performances of downscaled ISFETs sensors, where the study showed that the proposed DG ISFET design exhibits a superior performance for short channel domain in terms of threshold voltage and sensitivity behavior.

It also describes a Numerical Analysis of Thin Film Junctionless pH-ISFET Sensor. It has been shown that the proposed sensor has no source and drain junctions, where the concentration and doping type is the same in the channel region and in the source and drain. The performances of the proposed design were compared to the conventional pH-ISFET, illustrating the superior performance of the proposed sensor with respect to the conventional pH-ISFET in terms of fabrication process and electrical performances. Our numerical analysis provides the incentive for experimental exploration of the pH-ISFETs with Accumulation-Mode aspect. In addition, A Junctionless-multigate design to improve the electrical performances for deep submicron ISFET-based sensors. Moreover, we compared new sensor design, pH-JGAAISFET, with conventional planar pH-ISFET through 2-D device simulations. The short-channel effects of the pH-JGAAISFETs were more effectively suppressed than those of the conventional planar pH-ISFET.

Moreover, we compared new sensor design, DDGAA RADFET, with conventional planar RADFET through 2-D analytical investigation. A two-dimensional analytical analysis comprising radiation-induced interface-trap effect, 2D surface and interface potentials, threshold voltage shift and sensitivity model for DDGAA RADFET has been developed. It has been found that incorporation of the gate all around design leads to an improved threshold behavior while also enhancing the gate controllability, and thus provides better performance as compared to conventional planar RADFETs.

The threshold voltage shift behavior of the proposed design was more effectively improved than that of the conventional planar RADFET. In addition, we confirmed that DDGAA RADFET had advantages in CMOS scaling in comparison with planar RADFET. Moreover, the DDGAA RADFET has a linear sensitivity about in radiation dose ranging from $D = 0$ to $D=3000$ Gy. With continued progress towards fabricating RADFET-based dosimeters, it is possible to fabricate DDGAA RADFET without much technological processes. Our analytical analysis provides the motive for experimental exploration of the DDGAA RADFETs with around-gate and cylindrical-channel aspects. Application of the GA-based design approach to DDGAA RADFET has also been discussed. It can be concluded that the proposed GA-based approach is efficient and gives promising results. In order to show the impact of the proposed design on the radioactive environment monitoring, we developed a MLP-based approach to study a contaminated radioactive environment. The proposed approach can be used for remote sensing applications, where the information about the contaminated radioactive environment should be transmitted in electronic form to a receiving and processing station, where the generated data from our dosimeter sensor have been processed in order to denoise the image using a MLP-based technique.

With continued progress towards fabricating RADFET-based dosimeters and pH-ISFET sensors, it is possible to fabricate all proposed multi-gate FET-based sensors without much technological processes. It is to note that our work can be extended to implement the proposed designs into Software tools in order to study the engineering systems. Also, future research can investigate the use of new soft-computing based-techniques (PSO and quantum PSO-multi-objective approach) and new materials such as the graphene and the silicene, which may produce better results for more complex and accurate systems.

References

- [1] Mehrdad Hosseini Zadeh, "Advances in Haptics", chapter book, In-Teh, April 2010.
- [2] Vedran Kordic, "Cutting Edge Robotics 2010", chapter book, In-Teh, September 2010.
- [3] F. Djeflal , Z. Goughali, Z.Dibi, D. Arar “Analytical analysis of nanoscale multiple gate MOSFETs including effects of hot-carrier induced interface charges”, *Microelectronics Reliability*. vol. 49, no. 4, pp. 377-381, 2009.
- [4] A. Tsompatzoglou, C.A. Dimitriadis, R. Clerc, Q. Rafhay, G. ananakakis, G. Ghibaudo, “Semi-analytical modeling of short-channel effects in Si and Ge symmetrical double-gate MOSFETs”, *IEEE Trans Electron Devices*, vol 54, no. 8, pp.1943-1952, 2007.
- [5] Paul A. Hamond et al "A System-on-Chip Digital pH meter for Use in a Wireless Diagnostic Capsule"., *IEEE Trans*, vol 52,no. 4,pp. 687-694, 2005.
- [6] A J Bard and L R Faulkner. "Ion sensitive field effect transistor modelling for multidomain simulation purposes". *Microelectronics Journal*, vol. 35, pp. 831-840, 2004.
- [7] A. Hulanicki, S. Geab and F. Ingman, *Chemical sensors: definitions and classification*, Pure&App/. Chern. Vol. 63, No. 9, pp. 1247-1250, UK, 1991.
- [8] *Proceedings of the International Meeting on Chemical Sensors*, Fukuoka, Japan, September 19-22, 1983,Editors: T. Seyma, K. Fueki,J. Shiokawa and S. Suzuki, Elsevier-Kodanscha, Amsterdam and Tokyo, 1983.
- [9] H. Wohltjen, *Chemical Microsensors and Microinstrumentation*, *Anal. Chem.*, 19, 135, 1984.
- [10] W.R. Seitz, *Chemical Sensors Based on Immobilized Indicators and Fibre Optics*, *CRC Critical Reviews in Anal. Chem.*, 19, 135, 1988.
- [11] M. Thompson and U. J. Krull, *Biosensors and Bioprobes*, *Trends in Anal. Chem.*, 3, 173, 1984.
- [12] T.E. Edmonds (ed.), *Chemical Sensors*, Blackie and Sons Ltd., London, 1988.
- [13] A.P.F. Turner, I. Karube and G.S. Wilson (eds.), *Biosensors. Fundamentals and Applications*, Oxford University Press, New York, 1987.
- [14] Wen Wang, *Advances in Chemical Sensors*, Janeza Trdine 9, 51000 Rijeka, Croatia, Published by InTech, 2011.
- [15] D. Schuetzle, R. Hammerle and J. Butler (eds.), *Fundamentals and Applications of Chemical Sensors*, ACS Symposium Series, 309 American Chemical Society, 1986.
- [16] W. Gopel, *Entwicklung Chemischer Sensoren. Empirische Kunst oder systematische Forschung?* *Techn.Messen*, 2,47,92, 175,1985.

- [17] C. Nylander, Chemical Sensors and Biological Sensors, J. Phys. Sci. Instr., Is, 736, 1985.
- [18] J. Janata and A. Bezegh, Chemical sensors, Anal. Chem., @, 62R, 1988.
- [19] J. Janata, R.J. Huber (eds.), Solid-state Chemical Sensors, Academic Press, New York, 1985.
- [20] SMiddelhoek, Ed. Sensors and Actuators, vol. 10, 1986.
- [21] F. Scheller, F. Schubert, D. Pfeiffer, R. Hintsche, I. Dransfeld, R. Renneberg, U. Wollenberger, K. Riedel, M. Pavlova, M. Kuhn, H-G. Muller, P.M. Tan, W. Hoffmann and W. Moritz, Research and development of biosensors, Analyst, U, 653, 1989.
- [22] J. Janata, "Principles of Chemical Sensors", Springer Dordrecht Heidelberg London New York, 2009.
- [23] P. K. Sekhar et al "Chemical Sensors for Environmental Monitoring and Homeland Security", The Electrochemical Society Interface, winter 2010.
- [24] S. N. Ahmed, "Physics and Engineering of Radiation Detection", Academic Press Inc. Published by Elsevier 2007.
- [25] R. T. Kouzes, J. C. McDonald, D. M. Strachan, S. M. Bowyer, "Radiation Detection and Interdiction at U.S. Borders", Oxford University Press, USA, 2011.
- [26] Fan Ren and S. J. Pearton, "Semiconductor Device-Based Sensors for GAS, Chemical, and Bio-Applications", Taylor and Francis, 2011.
- [27] Gerhard Lutz, "Semiconductor Radiation Detectors", Springer-Verlag Berlin Heidelberg 1999, 2007.
- [28] "Sensors and sensor systems for Industrial and Environmental Applications", Printed in the UK on recycled paper with a minimum HMSO score of 75, 2004 available for free: <http://www.bis.gov.uk/files/file18891.pdf>.
- [29] M. Meguellati, F. Djefal and D. Arar, "A novel multigate design to improve the sensitivity behavior for deep submicron ISFET-based sensors", 2nd International Conference on electronics systems CISE 09, october25-26, 2009, Batna, Alegria.
- [30] C. Merkle, "It's a small, small, small, small world", MIT's Technology Review, vol. 100, no.2, pp. 25-32, 1997.
- [31] J.A. Voorthuzen and P. Bergveld, "Photoelectric effects in Ta₂O₅-SiO₂-Si structures," Sensors and Actuators, B1, pp. 350-353, 1990.
- [32] L. Bousse, D. Hanfeman and N. Tran, "Time-dependence of the chemical response of silicon nitride surfaces," Sensors and Actuators, B1, pp. 361-367, 1990.

- [33] I. Kobayashi, T. Ogawa, and S. Hotta, "Plasma-enhanced chemical vapor deposition of silicon nitride", *Jpn. J. Appl. Phys.*, vol. 31, pp. 336-342, 1992.
- [34] M. Chan, Y. Taur, C-H. Lin, J. He, A.M. Niknejad, C. Hu, in *Technical Proceedings of the 2003 Nanotechnology Conference and Trade Show, Volume 2*, San Francisco California, p.270, 2003.
- [35] F. Djeflal, M. Meguellati, N. Abdelmalek, " Numerical Analysis of Thin Film Junctionless pH-ISFET Sensor", *J. Sensors & Transducer*, Published by IFSA, pp. 35-40, Vol. 123, December 2010.
- [36] P. Bergveld, Development of an ion-sensitive solid state device for neurophysiological measurement, *IEEE Trans. Biomed. Eng. BME*, Vol. 21, 1974, pp. 485-487.
- [37] T-M Pan, K-M Liao, Structural properties and sensing characteristics of Y₂O₃ sensing membrane for pH-ISFET, *Sensors and Actuators B*, Vol. 127, 2007, pp. 480-485.
- [38] B. Premanode, N. Silawan, W P Chan, Chris T, A composite ISFET readout circuit employing current feedback, *Sensors and Actuators B*, Vol. 127, 2007, pp. 486-490.
- [39] A. Morgenshtein, L. S-Boreysha, U. Dinnar, C. G. Jakobson, Y. Nemirovsky, CMOS readout circuitry for ISFET Microsystems, *Sens. Actuators B, Chem*, Vol. 9, 2004, pp. 122-131.
- [40] T. M. Pan, C. H. Cheng, C. D. Lee, Yb₂O₃ thin films as a sensing membrane for pH-ISFET application, *J. Electrochem. Soc*, Vol. 156, 2009, pp. 108-111.
- [41] C. Y. Chen, J. C. Chou, H. T. Chou, Characteristics of cost-effective ultrathin HfTiO_x film as sensitive membrane in ISFET fabricated by anodization, *J. Electrochem. Soc*, Vol. 156, 2009, pp. 225-228.
- [42] W-Y. Chung, C-H Yang, DG. Pijanowskac, P B. Grabiec, W. Torbicz, ISFET performance enhancement by using the improved circuit techniques, *Sensors and Actuators B*, Vol. 113, 2006, pp. 555-562.
- [43] C-W. Lee, I. Ferain, A. Afzalian, R. Yan, N D. Akhavan, P. Razavi, J-P Colinge, Performance estimation of junctionless multigate transistors, *Solid-State Electron*, Vol. 54, 2010, pp. 97-103.
- [44] J. P. Colinge, Multi-gate SOI MOSFETs, *Solid-State Electron*, Vol. 48, 2004, pp. 897-905.
- [45] T-M. Pana, M-D. Huanga, C-W. Lina, M-H. Wub, Development of high-k HoTiO₃ sensing membrane for pH detection and glucose biosensing, *Sensors and Actuators B*, Vol. 144, 2010, pp. 139-145.
- [46] ATLAS: 2D Device Simulator, SILVACO International, 2008.

- [47] F. Djéffal, D. Arar, N. Abdelmalek, M. A. Abdi, R. Mahamdi, and A. Errachid, "A Junctionless-Multigate Design to Improve the Electrical Performances for Deep Submicron ISFET-Based Sensors" *Sensor Lett.* Vol. 9, pp: 2309-2311 (2011).
- [48] F. Djéffal, M. Meguellati, A. Benhaya, "A two-dimensional analytical analysis of subthreshold behavior to study the scaling capability of nanoscale graded channel gate stack DG MOSFETs", Published by Elsevier, *J. Physica E*, pp. 1872–1877, 41 ,2009.
- [49] M. A. Abdi, F. Djéffal, M. Meguellati, D. Arar, "Two-Dimensional Analytical Threshold Voltage Model for Nanoscale Graded Channel Gate Stack DG MOSFETs", 16th IEEE International Conference on Electronics, Circuits, and Systems, ICECS 2009, Dec. 13-16, 2009 Hammamet, Tunisia.
- [50] F. Djéffal, M. A. Abdi, Z. Dibi, M. Chahdi, and A. Benhaya, *Materials Sci. Eng: B* 147, 239 (2008).
- [51] F. Djéffal, Z. Ghoggali, Z. Dibi and N. Lakhdar, Analytical analysis of nanoscale multiple gate MOSFETs including effects of hot-carrier induced interface charges, *Microelectronics Reliability*, vol. 49, pp. 377-381, 2009.
- [52] E. Moreno, J. B. Roldán, F. G. Ruiz, D. Barrera, A. Godoy, and F. Gámiz, *Solid-State Electron.* 54, 1463 (2010).
- [53] M.A. Abdi, F. Djéffal, D. Arar, M.L. Hafiane, Numerical Analysis of Double- Gate and GAA MOSFETs with trap states, *Journal of Materials Science: Materials in Electronics*, pp. 248-253, 19(12), 2008.
- [54] M. Meguellati, F.Djéffal. New Dual-Dielectric Gate All Around (DDGAA) RADFET dosimeter design to improve the radiation sensitivity. *Nuclear Instruments and Methods in Physics Research A* 683(2012)24–28.
- [55] F. Djéffal, D. Arar., M.Meguellati and T. Bendib, "New Junctionless Dual-Dielectric RADFET dosimeter design to improve the electrical behaviour", 8èmes Journées Maghreb-Europe Matériaux et Applications aux Dispositifs et Capteurs 7-9 Novembre 2012, SOUSSE, Tunisia.
- [56] M. Meguellati, F. Djéffal, D. Arar, T. Bendib and L. Khetache, "RADFET dosimeter design for environment monitoring applications", 23th International conference en microelectronics ICM'2012, December 17-20, 2012, Algiers, Algeria.
- [57] F. Djéffal, T. Bendib, M. Meguellati, D. Arar and M.A Abdi, "New Dual-Dielectric Gate All Around (DDGAA) RADFET dosimeter design to improve the radiation sensitivity", World Congress on Engineering, London, 4-6 July, 2012, UK.

- [58] The international technology roadmap for semiconductors (ITRS); 2007. <<http://public.itrs.net>>.
- [59] D. Jiménez, B. Iñiguez, J. Suñé, L.F. Marsal, J. Pallarès, J. Roig and D. Flores, Continuous Analytic I-V Model for Surrounding-Gate MOSFETs, *IEEE Electron Devices Letters*, Vol.25, pp. 571-573, 2004.
- [60] H. Kaur, S. Kabra, S. Haldar and R.S. Gupta, An analytical drain current model for graded channel cylindrical/surrounding gate MOSFET, *Microelectronics Journal*, vol. 38, pp. 352-359, 2007.
- [61] A. G. Holmes-Siedle, The space charge dosimeter-General principles of a new method of radiation dosimetry, *Nuclear Instruments and Methods*, vol. 121, pp. 169–179, 1974.
- [62] A. Kelleher, W. Lane, L. Adams, A design solution to increasing the sensitivity of pMOS dosimeters: The stacked RADFET approach, *IEEE Trans. Nuclear Science*, vol. 42, pp.48–51, 1995.
- [63] A. Jaksic, G. Ristic, M. Pejovic, A. Mohammadzadeh, C. Sudre, W. Lane, Gamma-ray irradiation and post-irradiation responses of high dose range RADFETs, *IEEE Trans. Nuclear Science*, vol. 49, pp. 1356–1363, 2002.
- [64] J.R. Schwank, S.B. Roeske, D.E. Beutler, D. J. Moreno, M.R. Shaneyfelt, *IEEE Trans. Nuclear Science*, vol. 43, pp. 2671–2678, 1996.
- [65] I. G. Ristic, S. Golubovic, M. Pejovic, “pMOS transistors for dosimetric application”, *Electronics Letters*, 29 (18), pp. 1644-1646, 1993.
- [66] Fayçal DJEFFAL and Mohamed MEGUELLATI, “multigate RADFET dosimeter For Radioactive Environment Monitoring Applications”, series title: lecture notes in electrical engineering, Editors names: Gi-Chul Yang, SIO-IONG AO. Len Gelman, Title of Book/Volume/Conference: IAENG Transactions on Engineering Technologies -Special Issue of the World Congress on Engineering 2012, GPU/PS: 3/9059, SPIN: GT-C-CTP-09/2012, Springer.
- [67] F. Djeflal, N. Lakhdar, M. Meguellati and A. Benhaya, " Particle swarm optimization versus genetic algorithms to study the electron mobility in wurtzite GaN-based devices", Published by Elsevier, *J. Solid-State Electronics*, pp.388-392, 53(9), 2009.
- [68] T. Bendib, F.Djeflal, M. Meguellati, A. Benhaya and M. Chahdi, "A compact drain current model based on Genetic algorithm computation to study the nanoscale Double-Gate MOSFETs", *J. Semiconductor Physics, Quantum Electronics and Optoelectronics*, pp. 27-30, 12(1), 2009.
- [69] M. Meguellati, F. Djeflal, D. Arar, F. Douak and L. Khetache, “New RADFET

Dosimeter Design For Radioactive Environment Monitoring Applications", accepted for publication in Engineering Letters, special issue of IAENG Journals, 2012.

[70] Goldberg, D, "Genetic Algorithms in Search, Optimization and Machine Learning, Reading", MA: Addison-Wesley. 1989.

[71] Holland. J, "Adaptation in Natural and Artificial Systems". University of Michigan Press, Ann Arbor, MI. 1975.

[72] David E. Goldberg, "Genetic Algorithms in Search, optimization, and Machine Learning", Pearson, 2000.

[73] A. Chipperfield, P. Fleming, H. Pohlheim and C. Fonseca, "Genetic Algorithm TOOLBOX For Use with MATLAB", Handbook published by Department of automatic control and systems engineering, university of sheffield

[74] S.N.Sivanandam · S.N.Deepa, "Introduction to Genetic Algorithms", Springer-Verlag Berlin Heidelberg 2008.

[75] Mitchell Melanie, "An Introduction to Genetic Algorithms", A Bradford Book, Cambridge, Massachusetts • London, England Fifth printing, 1999.

[76] A.P. Engelbrecht, "Computational Intelligence An Introduction", Second Edition, John Wiley & Sons Ltd,2007.

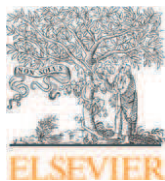
[77] Mu-Song Chen, "Analysis and design of the Multi-Layer Perceptron using polynomial basis functions", PHD thesis, THE UNIVERSITY OF TEXAS AT ARLINGTON, 1991.

[78] Taylor JG. "Neural networks and their applications". West Sussex (UK): John Wiley & Sons Ltd.; 1996.

[79] E.S. Gopi, "Algorithm Collections for Digital Signal Processing Applications Using Matlab", Published by Springer,2007.

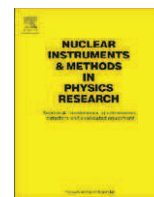
[80] A Canada Centre for Remote Sensing, Remote Sensing Tutorial, available on line for free: http://www.uprm.edu/biology/profs/chinea/gis/g06/NRC1_1_1_5.pdf.

[81] Guessasma S, Ghislain M, Christain C. Modeling of the APS plasma spray process using artificial neural networks: basis requirements and an example. Comput Mater Sci 2004;29:315.



Contents lists available at SciVerse ScienceDirect

Nuclear Instruments and Methods in Physics Research A

journal homepage: www.elsevier.com/locate/nima

New Dual-Dielectric Gate All Around (DDGAA) RADFET dosimeter design to improve the radiation sensitivity

M. Meguellati^a, F. Djeflal^{a,b,*}^a LEA, Department of Electronics, University of Batna, Batna 05000, Algeria^b LEPCM, University of Batna, Batna 05000, Algeria

ARTICLE INFO

Article history:

Received 8 February 2012

Received in revised form

4 April 2012

Accepted 26 April 2012

Available online 5 May 2012

Keywords:

Dosimeter

RADFET

Traps

Irradiation

Sensitivity

Analytical analysis

ABSTRACT

In this paper, a new radiation sensitive FET (RADFET) dosimeter design (called the Dual-Dielectric Gate All Around DDGAA RADFET dosimeter) to improve the radiation sensitivity performance and its analytical analysis has been proposed, investigated and expected to improve the sensitivity behavior and fabrication process for RADFET dosimeter-based applications. Analytical models have been developed to predict and compare the performance of the proposed design and conventional (bulk) RADFET, where the comparison of device architectures shows that the proposed design exhibits a superior performance with respect to the conventional RADFET in term of fabrication process and sensitivity performances. The proposed design has linear radiation sensitivities of approximately 95.45 $\mu\text{V}/\text{Gy}$ for wide irradiation dose range (from Dose=50 Gy to Dose=3000 Gy). Our results showed that the analytical analysis is in close agreement with the 2-D numerical simulation over a wide range of device parameters. As a result, we demonstrate that DDGAA RADFET dosimeter can be a viable option to enhance the performance of CMOS-based dosimeter technology for nuclear industry, space, radiotherapy and environment monitoring applications.

© 2012 Elsevier B.V. All rights reserved.

1. Introduction

The Gate All Around GAA MOSFETs have emerged as excellent devices to provide the electrostatic integrity needed to scale down transistors to minimal channel lengths, and allowing a continuous progress in digital and analog applications. In addition to a better electrostatics than the conventional bulk MOSFET, the use of these devices has advantages relative to the electronic transport, mainly due to (i) the reduced surface roughness scattering because of the lower vertical electric field and (ii) the reduction of the Coulomb scattering because the film is made of undoped/low-doped silicon [1–5]. Design and modeling guidelines of GAA MOSFETs have been discussed in previous works [2–7]. Employing this design for environment monitoring applications (irradiation measurement) becomes more beneficial if the device is made in vertical cylindrical recrystallized silicon due to highly flexible process integration options. There have been several reports of MOSFETs fabricated in recrystallized silicon for high-density digital integrated circuits [5].

Radiation sensitive MOSFETs (RADFETs) have been focused of interest both from applications and fundamental research point of

* Corresponding author at: LEA, Department of Electronics, University of Batna, Batna 05000, Algeria. Tel./fax: +213 33805494.

E-mail addresses: faycal.djeflal@univ-batna.dz, faycaldz@hotmail.com (F. Djeflal).

views. In electronic industry these devices are considered as attractive alternatives for nuclear industry, space, radiotherapy and environment monitoring applications due to their reliability, low power consumption, non-destructive read-out of dosimetric information, high dose range, and compatibility to standard CMOS technology and on-chip signal processing [8–10]. The main RADFET disadvantage is the relatively low sensitivity. In this context, the submicron multi-gate design may be considered as attractive alternative to overcome this disadvantage because of the high electrical performance and reliability provided by the multi-gate structure in comparison with single-gate one. However, as semiconductor devices are scaled into the deep submicron domain, short-channel effects (SCEs) begin to plague conventional planar CMOS-based devices. To avoid the electrical constraints and improve the sensitivity performance, a new design and enhancement of conventional (bulk) RADFET become important. In this work, a new design of RADFET called the Dual-Dielectric Gate All Around (DDGAA) RADFET dosimeter, in which the manufacturing processes and sensitivity performances will be greatly improved, is proposed for deep submicron CMOS-based dosimeter applications. The (DDGAA) RADFET dosimeter design presented in this paper is basically surrounded by dual-dielectric layers (SiO_2 and Si_3N_4) with low p-channel (Si) doping concentration. The results showed that the analytical model is in agreement with the 2-D numerical simulation over a wide range of device parameters. The proposed structure has been analyzed and validated by the good sensitivity and electrical performance obtained

in deep submicron regime in comparison with the conventional (bulk) design.

This paper is organized as follows. In Section 2, we derive an analytical interface potential distribution including radiation-induced interface-traps. The threshold voltage shift model can then be determined based on the interface potential model. In Section 3, we investigate the performance of the proposed design. The conclusions will be drawn in Section 4.

2. Theory development and model derivation

2.1. Interface potential analysis

Schematic cross-sectional view of the proposed (DDGAA) RADFET dosimeter is presented in Fig. 1. The insulator consists of a thermal oxide (SiO_2) grown on a (100) n on n+ epitaxial silicon substrate (channel), and a low pressure CVD silicon nitride layer (Si_3N_4) deposited on top of the oxide. N_{DJS} represents the doping level of the drain/source region, respectively. The channel region is bounded by source and drain spacing at $x=0$ and L , respectively, where L is the gate length. With a negatively applied gate bias, holes generated in the SiO_2 layer are transported and trapped at the $\text{SiO}_2/\text{Si}_3\text{N}_4$ interface producing a measurable threshold-voltage shift [9]. Therefore, our analytical analysis is focused to study the impact of the device design, planar and surrounding structures, on the sensitivity performance taking in to account the Dual-Dielectric aspect for the both cases in order to improve the sensitivity behavior for deep submicron applications. The investigation reported in this work for gamma radiation sources can also be applied qualitatively to other radiation sources (protons, electrons, etc.).

For deep submicron devices, the solution of 2D Poisson's equation satisfying suitable boundary conditions is required to model the interface potential. Refer to Fig. 1, the 2D Poisson's equation for the channel region is given by

$$\frac{1}{r} \frac{\partial}{\partial r} \left(r \frac{\partial}{\partial r} \psi(r, x) \right) + \frac{\partial^2}{\partial x^2} \psi(r, x) = \frac{qN_D}{\epsilon_{si}} \quad (1)$$

The boundary conditions for $\psi(x, r)$ are found by satisfying continuity of both the normal component of the electric displacement at the (Si/SiO_2) interfaces, and the potential at the source/drain sides.

Using the same parabolic potential profile in vertical direction [2] and applying the symmetry condition of $\partial\psi/\partial r=0$ for $r=0$, we obtain the following expressions of 2-D channel potential as

$$\psi(r, x) = \frac{C_{ox}}{\epsilon_{si} t_{si}} \left[V_g^* - \psi_s(x) \right] r^2 + \left(1 + \frac{C_{ox} t_{si}}{4\epsilon_{si}} \right) \psi_s(x) - \frac{C_{ox} t_{si}}{4\epsilon_{si}} V_g^* \quad (2)$$

where $\psi_s(x)$ represents the surface potential (the potential at the Si/SiO_2 interface) with C_{ox} represents the insulator capacitance

($C_{ox} = 2\pi\epsilon_1 L / \ln(1 + 2t_1/t_{si})$), t_{si} is the silicon thickness, the effective oxide and silicon nitride layer is defined as $t_{oxeff} = t_1 + t_2(\epsilon_1/\epsilon_2)$ with t_1 is the thickness of the SiO_2 ($\epsilon_1 = \epsilon_{ox}$) layer and t_2 is the thickness of the Si_3N_4 layer (ϵ_2). V_{bi} is the junction voltage between the source/drain and intrinsic silicon, $V_{bi} = (kT/q) \ln(N_{D/S}/n_i)$, n_i is the intrinsic silicon density, V_{ds} represents the drain-to-source voltage and k is the Boltzmann constant. V_g^* represents the effective voltage at the gate which is introduced to simplify notations and alleviate derivations for symmetric structure as $V_g^* = V_{gs} - V_{fb}$, with V_{fb} is the flat-band voltage.

Substituting (2) in (1), we obtain the differential equation that deals only with surface potential as

$$\frac{d^2 \psi_s(x)}{dx^2} - \frac{1}{\lambda^2} \psi_s(x) = D_1 \quad (3)$$

with $\lambda = \sqrt{\epsilon_{si} t_{oxeff} t_{si} / 4\epsilon_{ox}}$ and $D_1 = qN_D / \epsilon_{si} - (1/\lambda^2) V_g^*$ where λ represents the natural length of the analyzed (DDGAA) RADFET dosimeter. This parameter gives the scaling capability (down-scaling ability) of the device. D_1 is a factor which represents the impact of the applied gate voltage and channel doping on the surface potential.

The boundary conditions in channel and oxide regions (Fig. 1) are given as,

$$\psi_s(x=0) = V_{bi} \quad (4a)$$

$$\psi_s(x=L) = V_{bi} + V_{ds} \quad (4b)$$

$$\epsilon_2 \frac{V_{gs}^* - \psi_s^*}{t_2} = \epsilon_1 \frac{\psi_s^* - \psi_s}{t_1}$$

(continuity of the normal component of the electric displacement at the interface $\text{SiO}_2/\text{Si}_3\text{N}_4$)

$$(4c)$$

where ψ_s^* represents the interface potential at $\text{SiO}_2/\text{Si}_3\text{N}_4$ interface which satisfies the continuity of the normal component of the electric displacement at the interface (Eq. (4c)).

Substituting (4c) in (3), we obtain the differential equation that deals only with interface potential as

$$\frac{d^2 \psi_s^*(x)}{dx^2} - \frac{1}{\lambda^2} \psi_s^*(x) = D_2 \quad (5)$$

with $D_2 = \alpha - \beta V_{gs}^*$ and $\alpha = qN_D \epsilon_2 t_1 / \epsilon_{si} (\epsilon_2 t_1 + \epsilon_1 t_2)$, $\beta = \epsilon_2 t_1 / \lambda^2 (\epsilon_2 t_1 + \epsilon_1 t_2)$

The resolution of this equation allows us the calculation of the interface potential without (before) irradiation.

In the case of RADFET under irradiation new term should be introduced in order to include the radiation-induced interface-traps effect [2]. So, the parameter D_2 can be written, in this case, as, $D_2 = \alpha - \beta V_{gs}^* - (qN_f / \epsilon_2 t_2)$, with N_f represents the irradiation induced localized interface charge density per square area. The second term in this expression represents the impact of the

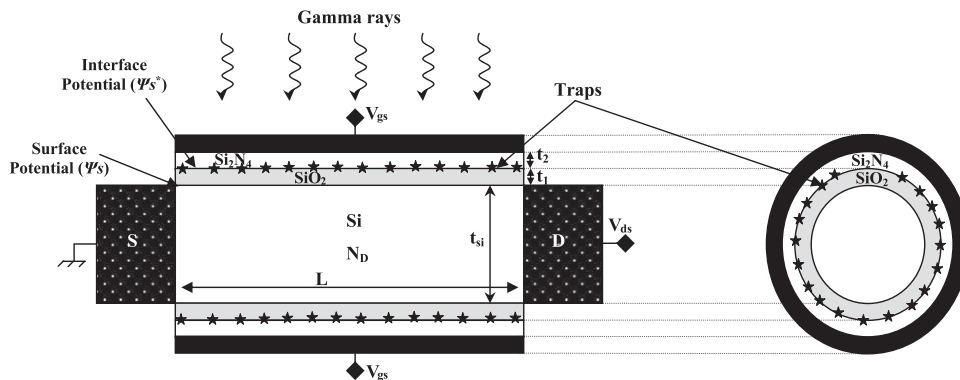


Fig. 1. Cross-sectional view of the proposed DDGAA RADFET design ($L=100$ nm, $t_1=5$ nm, $t_2=5$ nm, $t_{si}=20$ nm).

irradiation induced localized interface charge density on the interface potential.

Using these boundary conditions (Eq. (4a)–(c)), the surface and interface potentials can be, respectively, expressed as

$$\psi_s(x) = -\lambda^2 D_2 + \frac{\phi_D \sin h(x/\lambda) - \phi_S \sin h(x-L/\lambda)}{\sin h(L/\lambda)} \quad (6)$$

With $\phi_D = V_{ds} + \lambda^2 D_2$ and $\phi_S = V_{bi} + \lambda^2 D_2$

$$\psi_s^*(x) = \frac{\varepsilon_1 t_2}{\varepsilon_2 t_1 + \varepsilon_1 t_2} V_{gs}^* + \frac{\varepsilon_2 t_1 x}{\varepsilon_2 t_1 + \varepsilon_1 t_2} \psi_s(x) \quad (7)$$

2.2. Threshold voltage shift model

The basic concept of RADFET dosimeter is to convert the threshold voltage shift, ΔV_{th} , induced by radiation, into absorbed radiation dose, where $\Delta V_{th} = V_{th} - V_{th0}$ with V_{th} and V_{th0} represent the threshold voltage after and before irradiation, respectively.

Based on the surface potential model given by Eq. (6), the threshold voltage can be derived using the condition of the minimum channel potential $\psi_{s \min}|_{V_{gs} = V_{th}} = 2 \cdot \phi_B$, with $\psi_{s \min} = \psi_s(x_{\min})$, V_{th} is the threshold voltage value, and ϕ_B represents the bulk potential of silicon body given as $\phi_B = (K_B T/q) \cdot \ln(N_D/n_i)$ where K_B represents the Boltzmann constant. The location of the minimum surface potential can be obtained analytically by solving $d\psi_s(x)/dx = 0$ [2].

The solution of the equation $\psi_{s \min}|_{V_{gs} = V_{th}} = 2 \cdot \phi_B$ at low drain-source voltage for long channel lengths ($L \gg \lambda$) can be given as

$$V_{th} = \frac{(2A\phi_B + \lambda^2 \alpha + (qN_f/\varepsilon_2 t_2)) \sin h(L/\lambda) + (V_{bi} - V_{ds}) \sin h(L/2\lambda)}{(\beta \lambda^2 - (B/A)) \sin h(L/\lambda) - 2 \sin h(L/2\lambda)} \quad (8a)$$

with $A = \varepsilon_1 t_2 - \varepsilon_2 t_1 / \varepsilon_1 t_2$, $B = \varepsilon_2 t_1 / \varepsilon_1 t_2$

$$V_{th0} = V_{th}|_{N_f=0} = \frac{(2A\phi_B + \lambda^2 \alpha) \sin h(L/\lambda) + (V_{bi} - V_{ds}) \sin h(L/2\lambda)}{(\beta \lambda^2 - (B/A)) \sin h(L/\lambda) - 2 \sin h(L/2\lambda)} \quad (8b)$$

From (8a) and (8b), the threshold voltage shift can be given as

$$\Delta V_{th} = \frac{(qN_f/\varepsilon_2 t_2) \sin h(L/\lambda)}{(\beta \lambda^2 - (B/A)) \sin h(L/\lambda) - 2 \sin h(L/2\lambda)} \quad (8c)$$

3. Results and discussion

Fig. 2 shows the variation of the calculated surface potential (Fig. 2a) and interface potential (Fig. 2b) along the channel for a 100 nm DDGAA RADFET with different interface charge densities N_f at the bias condition $V_{gs} = -5$ V and $V_{ds} = 1$ V. It can be seen that a shift in the potential profile along the channel (for the surface and interface potentials) has been found. The shift in the potential profile screens the region near the source end from the variations in drain voltage and thus ensures reduction in short channel effect. In addition, a good uniform decreasing of the surface potential as function of the interface charge densities can be observed in Fig. 2a. This surface potential behavior can provide a high threshold voltage sensitivity as function of the interface charges densities (N_f), which is the main parameter which affects the RADFET sensitivity. Therefore, the proposed design can provide a high sensitivity performance. In Fig. 3, the variation of threshold voltage shift with different interface charge densities N_f has been compared with conventional bulk (single gate) RADFET. It is shown that the threshold voltage shift values are considerably increased in case of DDGAA RADFET even for interface charge densities more than $6 \cdot 10^{11} \text{ cm}^{-2}$. Moreover, due to the improved

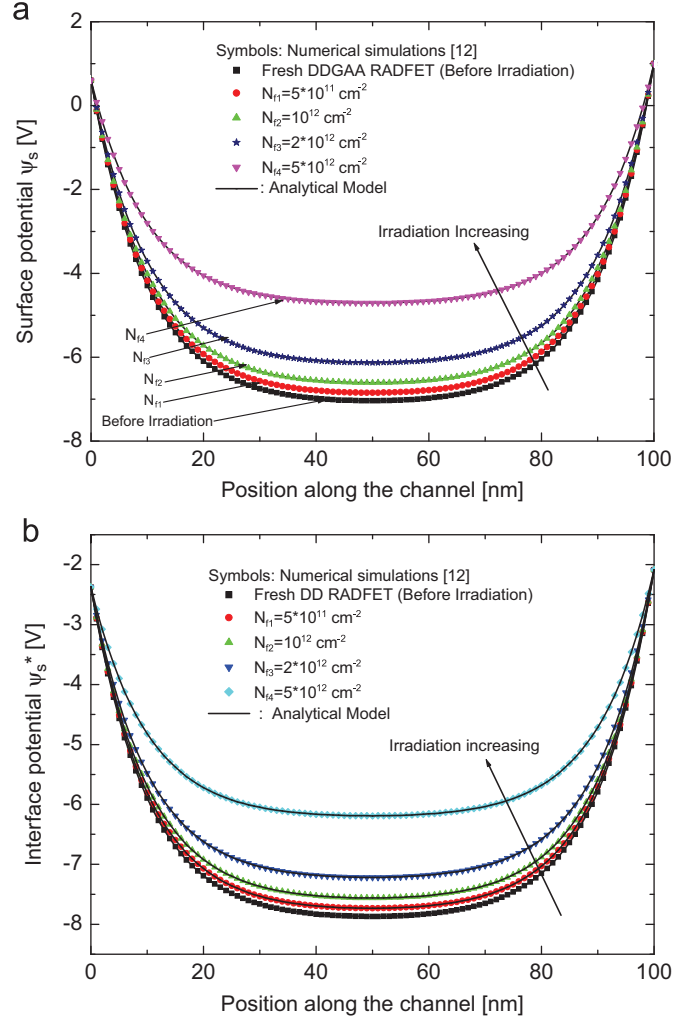


Fig. 2. (a) Variation of surface potential along the channel and (b) variation of interface potential along the $\text{SiO}_2/\text{Si}_3\text{N}_4$ interface for different irradiation-induced interfacial traps densities with ($V_{gs} = -5$ V, $V_{ds} = 1$ V, $L = 100$ nm, $t_1 = 5$ nm, $t_2 = 5$ nm, $\varepsilon_1 = 3.9$, $\varepsilon_2 = 7.5$, $t_{si} = 20$ nm, $N_D = 10^{15} \text{ cm}^{-3}$) (see Ref. [12]).

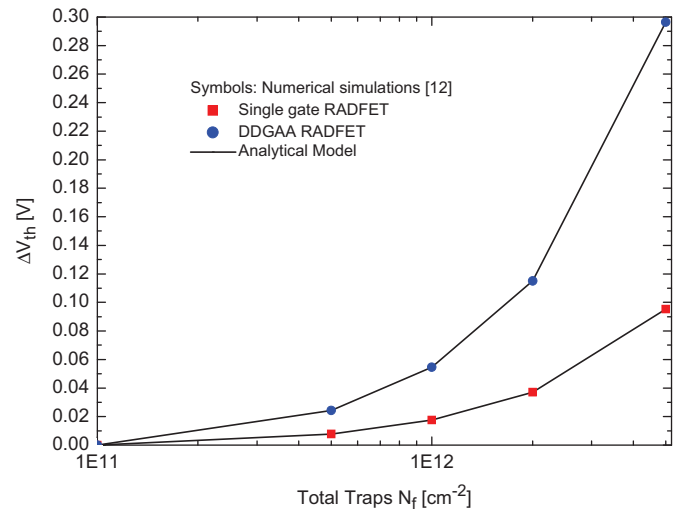


Fig. 3. Threshold voltage shift variation against the irradiation-induced interfacial traps densities for the conventional and DDGAA RADFET designs (see Ref. [12]).

gate controllability, DDGAA RADFET has a higher threshold voltage shift values as compared to conventional RADFET which makes it suitable for high sensitive dosimeter applications.

The RADFET radiation sensitivity, S , given by [10,11]:

$$S = \frac{\Delta V_{th}}{D} \quad (9)$$

where D represents the absorbed radiation dose.

From an experimental study carried out by Jaksic et al. [10] an empirical relationship between the interface charge densities, N_f , and the absorbed radiation dose, D , for the silicon material at room temperature can be written as

$$N_f = d_{11}D + d_{12} \quad (10)$$

where $d_{11} = 1.6 \times 10^9 \text{ cm}^{-2}/\text{Gy}$ and $d_{12} = 5 \times 10^{10} \text{ cm}^{-2}$ are fitting parameters.

Substituting (10) in (8c), we obtain the RADFET sensitivity model that deals only with absorbed radiation dose as

$$S = \frac{(q/\varepsilon_2 t_2) \sin h(L/\lambda) (d_{11} + (d_{12}/D))}{(\beta \lambda^2 - (B/A)) \sin h(L/\lambda) - 2 \sin h(L/2\lambda)} \quad (11)$$

In Fig. 4, the variation of DDGAA RADFET sensitivity versus the absorbed radiation dose, D , has been compared with conventional (bulk) RADFET. For both designs, the output response of the RADFETs is linear with absorbed radiation dose. It is clearly shown that DDGAA RADFET has higher sensitivity, $S = 95.45 \mu\text{V}/\text{Gy}$, in

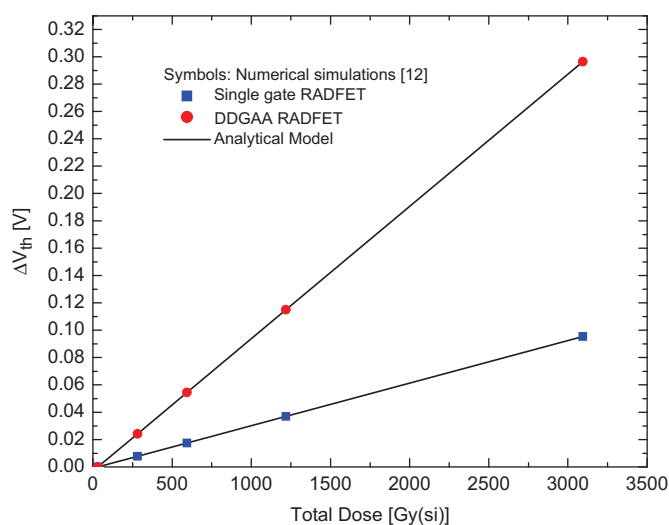


Fig. 4. Variation of threshold voltage shift in function of the absorbed radiation dose for the conventional and DDGAA RADFET designs (see Ref. [12]).

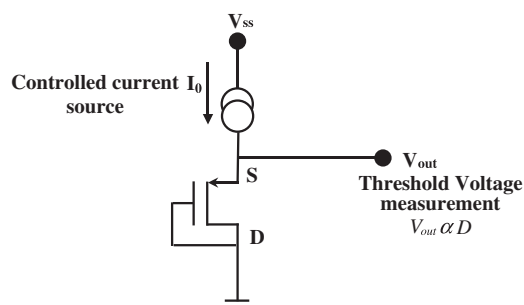


Fig. 5. Set-up for a measurement of V_{th} and absorbed radiation dose (read-out circuit configuration).

comparison with conventional RADFET design, $S = 30.68 \mu\text{V}/\text{Gy}$. This means that DDGAA RADFET has better electrical and scaling performances in comparison with the conventional design. So, our design provides a high sensitivity, better electrical and technological performances in comparison with the conventional structure. These results make the proposed design as a promising candidate for CMOS-based dosimeters.

Due to the high performance provided by the proposed RADFET design (high sensitivity and threshold voltage linearity), the read of the absorbed radiation dose (D) can be carried out by using a simple Read-out Circuit (RC), as it is shown in Fig. 5. In Fig. 5, the threshold voltage is measured at a single point of the transfer characteristics, applying a specified current (in the order of ten μA) to the RADFET, while drain and gate are shorted. Due to the simplicity of the Read-out Circuit, the RC configuration is suitable for practical low power applications.

It should be mentioned that from a fabrication point of view, the conventional deep submicron planar RADFET is much easier to fabricate than DDGAA RADFETs. With the advancement of CMOS process technology under 100 nm regime, fabrication of DDGAA RADFETs should not be complex in near future. Hence, our work concludes that DDGAA RADFET is a competitive contender to the mainstream RADFETs for the design of low-power RADFET-based circuits.

4. Conclusion

In this paper, we compared new sensor design, DDGAA RADFET, with conventional planar RADFET through 2-D analytical investigation. A two-dimensional analytical analysis comprising radiation-induced interface-traps effect, 2D surface and interface potentials, threshold voltage shift and sensitivity model for DDGAA RADFET has been developed. It has been found that incorporation of the gate all around design leads to an improvement of the threshold behavior while also enhancing the gate controllability, and thus providing better performance as compared to conventional planar RADFETs. In addition, in experiment, the proposed cylindrical design could be easily released in comparison to the planar one. The threshold voltage shift behavior of the proposed design was more effectively improved than those of the conventional planar RADFETs. Also, we confirmed that DDGAA RADFET had advantages in CMOS scaling in comparison with planar RADFET. Moreover, the DDGAA RADFET has a linear sensitivity about $S = 95.45 \mu\text{V}/\text{Gy}$ in radiation dose ranging from $D = 50$ to $D = 3000$ Gy. With continued progress towards fabricating RADFET-based dosimeters, it is possible to fabricate DDGAA RADFET without much technological processes. This work also provides the incentive and guide to further research and experimental exploration of the unique features of DDGAA RADFETs, and demonstrates a new way of engineering sub-micron CMOS-based integrated dosimeter circuits with the focus on uncovering the potential of DDGAA RADFET in the context of electrical and sensitivity performance.

References

- [1] The international technology roadmap for semiconductors (ITRS). <<http://public.itrs.net>>, 2007.
- [2] F. Djeflal, Z. Ghoggali, Z. Dibi, N. Lakhdar, Microelectronics Reliability 49 (2009) 377.
- [3] D. Jiménez, B. Iñiguez, J. Suñé, L.F. Marsal, J. Pallarès, J. Roig, D. Flores, IEEE Electron Devices Letters 25 (2004) 571.
- [4] H. Kaur, S. Kabra, S. Haldar, R.S. Gupta, Microelectronics Journal 38 (2007) 352.
- [5] M.A. Abdi, F. Djeflal, D. Arar, M.L. Hafiane, Journal of Material Science: Materials of Electronics 19 (2008) S248.

- [6] J. He, Y. Tao, F. Liu, J. Feng, S. Yang, *Solid-State Electronics* 51 (2007) 802.
- [7] J. He, Y. Tao, M. Fang, J. Feng, *IEEE Transactions on Electron Devices* 54ED (2007) 2293.
- [8] A.G. Holmes-Siedle, *Nuclear Instruments and Methods* 121 (1974) 169.
- [9] A. Kelleher, W. Lane, L. Adams, *IEEE Transactions on Nuclear Science* 42NS (1995) 48.
- [10] A. Jaksic, G. Ristic, M. Pejovic, A. Mohammadzadeh, C. Sudre, W. Lane, *IEEE Transactions on Nuclear Science* 49 (2002) 1356.
- [11] J.R. Schwank, S.B. Roeske, D.E. Beutler, D.J. Moreno, M.R. Shaneyfelt, *IEEE Transactions on Nuclear Science* 43 (1996) 2671.
- [12] Atlas User's manual, SILVACO TCAD, 2008.

ISSN 1726-5479

SENSORS & TRANSDUCERS

12^{vol. 123}/₁₀



Sensor Market Trends

International Frequency Sensor Association Publishing





Numerical Analysis of Thin Film Junctionless pH-ISFET Sensor

**Fayçal DJEFFAL, Mohammed MEGUELLATI, Nedhal ABDELMALEK
and Toufik BENDIB**

LEA, Department of Electronics, University of Batna, 05000, Algeria

Tel./fax: 0021333805494

E-mail: faycaldzdz@hotmail.com

Received: 25 August 2010 /Accepted: 21 December 2010 /Published: 28 December 2010

Abstract: In this paper, a new pH-ISFET sensor, called the Junctionless ISFET sensor (JISFET), and its numerical analysis have been proposed, investigated and expected to improve the fabrication process and the sensitivity behavior for pH-ISFET sensor-based applications. The numerical analysis has been used to predict and compare the performances of the proposed design and conventional pH-ISFET, where the comparison of device architectures shows that the proposed pH- JISFET sensor exhibits a superior performance with respect to the conventional pH-ISFET in term of fabrication process and electrical performances. Moreover, the proposed design has linear pH sensitivities of approximately 59.6 mV/pH for wide concentration range (from pH =2 to pH=12). The obtained results make the Junctionless ISFET sensor a promising candidate for future CMOS-based sensors. *Copyright © 2010 IFSA.*

Keywords: Junctionless ISFET, Thin film, Sensor, Electrical performances.

1. Introduction

Ion-sensitive field-effect transistors (ISFETs) have been focus of interest both from applications and fundamental research point of views. In electronic industry these devices are considered as attractive alternatives for chemical, physiological and environment monitoring applications due to their rapid time responses, reliability, and compatibility to standard CMOS technology and on-chip signal processing [1-4]. The so-called threshold voltage of the transistor is a function of the solution surrounding the gate. The operational mechanism of the ISFET originates from the pH sensitivity of the inorganic gate oxide such as SiO₂ or Ta₂O₅. Many experimental and theoretical studies have been recently published of describing the electrical and sensitivity behaviors of conventional pH-ISFET

sensor [5-7], in which the Inversion-Mode (IM) design is used to elaborate these sensors. A conventional pH-ISFET comprises two PN junctions called the source junction and the drain junction. The formation of such junctions involves extremely high doping concentration gradients, and low thermal budget processing must be used [8]. Flash annealing methods are used to heat silicon for a short time period in order to minimize diffusion effect, however even in total absence of diffusion, ion implantation and other doping methods do not obtain perfectly abrupt junctions with infinite concentration gradients [8]. To avoid the above-mentioned technological constraints, a new design and improvement of conventional pH-ISFET become important. In this work, a new design of pH-ISFET called Junctionless ISFET sensor (pH-JISFET), in which the manufacturing processes will be greatly improved, is proposed for future CMOS-based sensors. This latter is based on Accumulation-Mode (AM) aspect, in which the channel region has the same doping polarity as the source and drain. (AM) technology can also be applied to most Silicon-On-Insulator (SOI) designs [8, 9]. The pH-JISFET design presented in this work is basically Accumulation-Mode device with low channel doping concentration. The proposed sensor has no junctions, less variability, simpler fabrication process and better electrical performances than conventional inversion-mode ISFET sensors.

In this paper, we investigate and analyze numerically the pH-JISFET in order to explain the advantages of the proposed device over the conventional pH-ISFET with the same electric and geometric specifications that allow us to utilize the benefits of the incorporation of the Accumulation-Mode aspect on the design and fabrication process of the future pH-ISFET sensors.

2. JISFET Design and its Parameters

The pH-ISFET can be seen as an ions sensor device. The physical treatment of the pH-ISFET attempts to relate the amount of ions concentration and reference voltage applied between the gate, and the body to the amount of inversion or accumulation charges accumulated in the channel. This charge distribution in the channel can then be related to the variation of the threshold voltage for a given drain–source bias and ions concentration. The accumulated charge at the semiconductor/oxide interface, together with the channel electrostatic potential drop, gives rise to a capacitance C_{Si} . Fig. 1 shows a plot of the total, Electrolyte-Insulator-Semiconductor (EIS), capacitance, normalized to the insulator capacitance, as a function of bias voltage and pH values, illustrating the effect of the pH values on C-V characteristics for the depletion and accumulation working modes.

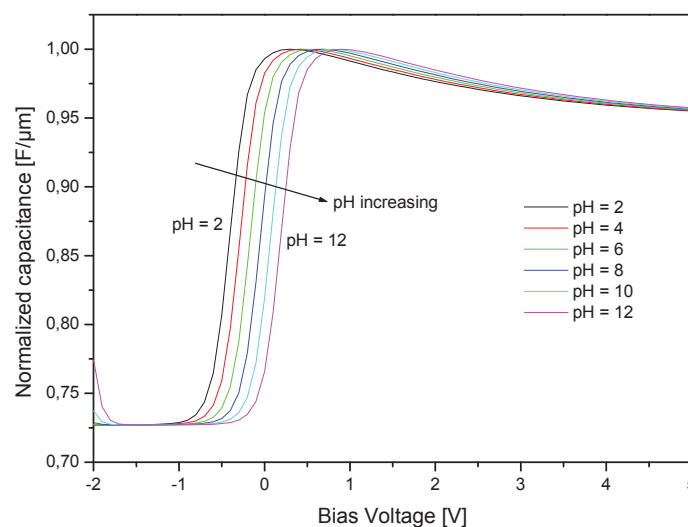


Fig. 1. C–V curves response of the proposed AM-based pH-JISFET for different pH values (from pH=2 to pH=12).

The main effect of a change in a pH solution is a shift in the threshold voltage and the total accumulation capacitance. This phenomenon can be modeled according to the site-binding model [10,2]. As a consequence of these shifts, the EIS structure can be used as sensor diode for depletion and accumulation working modes.

The cross-sectional view of the conventional pH-ISFET and pH-JISFET are shown in Fig. 2. From the figures it is clear that in the case of pH-JISFET design the channel region has the same doping polarity as the source and drain. So, the proposed design has no junctions and less variability in comparison to the conventional pH-ISFET. The device is analyzed with a gate oxide thickness of 10nm. The silicon film thickness is chosen to be very thin layer, 20nm, in order to avoid the shifting of the channel region in the deep of SOI film in the case of Accumulation-Mode design [8]. The channel length for both devices is 350nm which is compatible with CMOS process technology. Also, the incorporation of a high- k HoTiO_3 as sensing membrane deposited on oxide film can improve the sensitivity behavior in comparison with conventional pH-ISFET sensors for wide pH range [10].

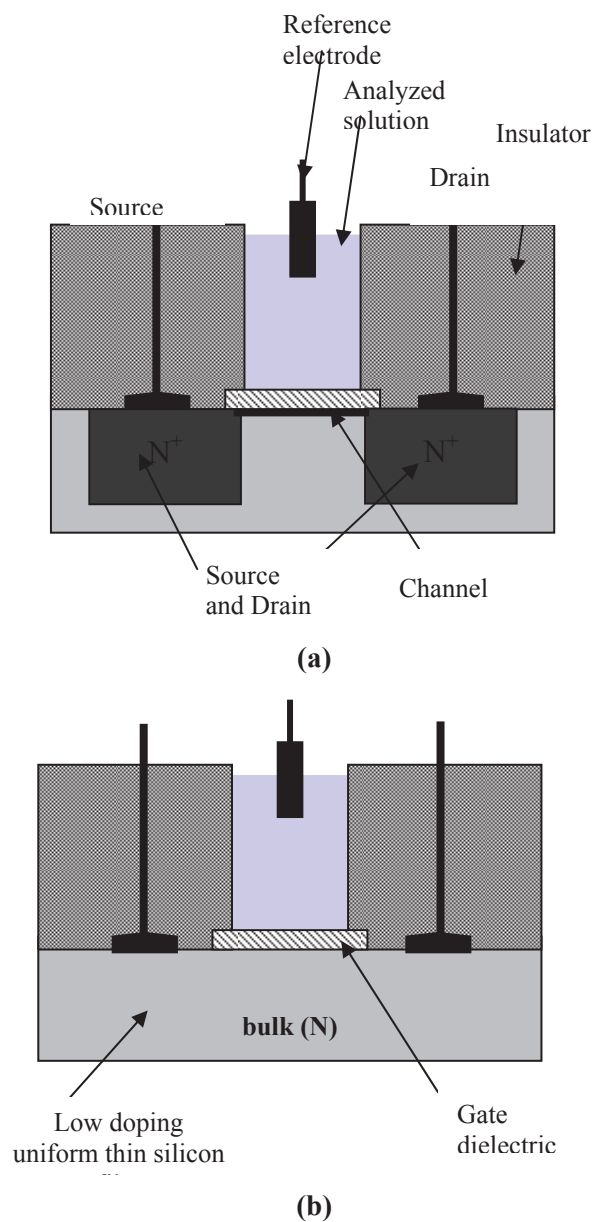


Fig. 2. Longitudinal cross sections showing the doping profiles: (a) conventional IM-based pH-ISFET, and the (b) proposed AM-based pH-JISFET.

The electrical parameters of both devices, AM-based JISFET and IM-based ISFET, were analyzed using ATLAS 2-D device simulator [11]. The numerical studies are performed to compare the characteristics of the proposed AM-based JISFET structure with conventional IM-based ISFET on the basis electrical and fabricating process performances. The parameters used in our study for both structures are given in Table 1.

Table 1. Simulation parameters of both devices.

Parameters	pH-ISFET	pH-JISFET
Channel doping	5.1016 cm ⁻³ (P-type)	5.1016 cm ⁻³ (N-type)
Source/Drain doping	1020 cm ⁻³ (N+-type)	5.1016 cm ⁻³ (N-type)
Silicon thickness (tsi)	20 nm	20 nm
Channel length (L)	0.35 μm	0.35 μm
Channel width (W)	1 μm	1 μm
Gate oxide thickness (tox)	10 nm	10 nm
Sensing membrane	high-k HoTiO ₃	high-k HoTiO ₃

The simulated AM-based JISFET has a uniform doping concentration ($N_D = 5.10^{16} \text{ cm}^{-3}$) throughout the channel and source/drain regions, whereas abrupt source and drain junctions are used for the IM-based ISFET. Appropriate models are used in ATLAS for drift-diffusion model without impact ionization, carrier mobility, recombination-generation and the parameters such as threshold voltage, channel electric field and leakage current compared by changing the pH between 2 and 12 at a constant of drain current of 10 μA for saturation regime and 4 μA for linear domain. It is to note that all computations have been done at room temperature.

3. Results and Discussions

Because of the uniform N-type doping of the channel, the AM-based JISFET requires an appropriate sensing membrane and reference voltage in order to improve the sensor performances and to achieve a suitable threshold voltage values for wide concentration range. The transconductance gives the same peak value in a concentration range between pH=2 and pH=12 as shown in Fig. 3.

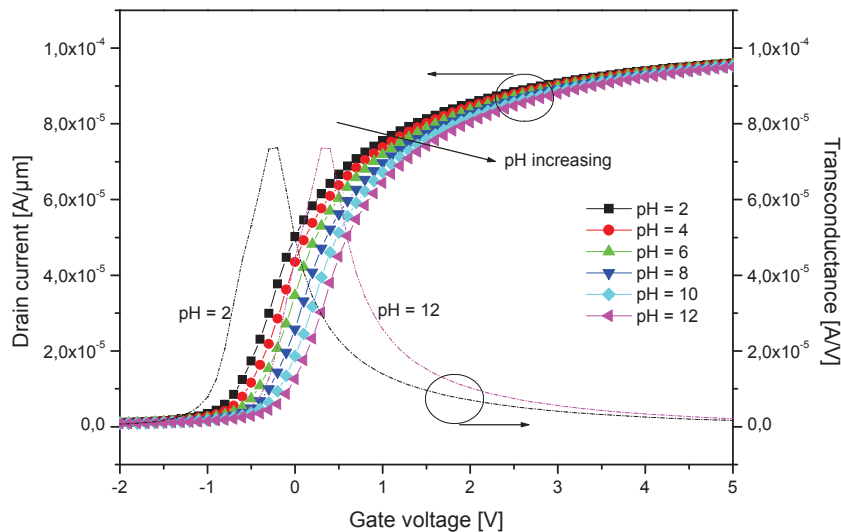


Fig. 3. Curves of the drain current and the transconductance versus bias voltage with different pH values.

The slope of the same I_D versus bias voltage can be obtained around the maximum transconductance. This slope has a concept with bias voltage that is the threshold voltage of AM-based JISFET. Fig. 4 shows that the pH sensitivity of the proposed AM-based JISFET sensor was investigated through the shift in the threshold voltage as function of pH values. This variation is mainly due to the ionization of the surface hydroxyl groups by either hydrogen ions or hydroxyl ions. To evaluate the sensing performances of the proposed design, we plotted the pH-dependence of the reference voltage for both working regimes (weak and strong accumulation modes). The pH sensitivity and linearity of the AM-based JISFET were about 59.60 mV/pH and 0.98 for weak and strong accumulation regimes. The same sensitivity has been recorded in the case of conventional design.

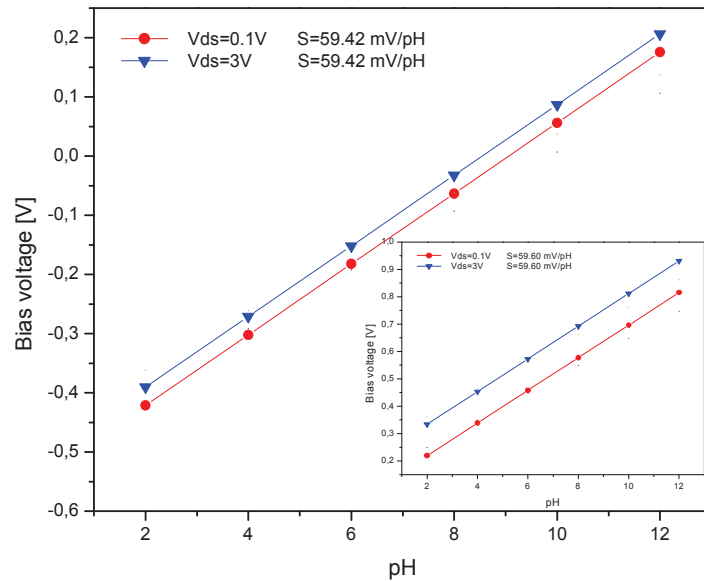


Fig. 4. Bias voltage of the AM-based pH-JISFET as function of pH values. The inset shows bias voltage of the conventional IM-based pH-ISFET as function of pH values for both working regimes (linear and saturation).

Table 2 shows a comparison of the sensitivities and the electrical performances of both architectures. As can be seen from the table, AM-based JISFET has better electrical performances in comparison with the conventional design. So, our design provides a high sensitivity, better electrical and technological performances in comparison with the conventional structure. These results make the proposed design as a promising candidate for future CMOS-based sensors.

Table 2. pH sensitivity and electrical characteristics of both devices.

Parameters	pH-ISFET	pH-JISFET
Output Conductance [$A/V \cdot \mu m$]	3.26.10-6	1.98. 10-8
Off-current [$A / \mu m$]	2.42.10-5	1.62.10-5
Subthreshold Swing [mV / dec]	92.38	61.58
Threshold voltage [V]	0.07	-0.14
DIBL [mV / V]	1821.90	244.27
Power consumption [$mW / \mu m$]	2.30	0.19
Sensitivity [mV / pH]	59.42	59.60
Thermal stability	stable for wide temperature range	stable for wide temperature range
Cost	average	Low

4. Conclusions

In this paper, a new pH-ISFET, called the Junctionless ISFET sensor (JISFET), based on Accumulation- Mode aspect has been proposed. The proposed sensor has no source and drain junctions, where the concentration and doping type is the same in the channel region and in the source and drain. The performances of the proposed design were compared to the conventional pH-ISFET, illustrating the superior performance of the proposed sensor with respect to the conventional pH-ISFET in terms of fabrication process and electrical performances. Moreover, the JISFET has a linear sensitivity about 59 mV/pH in a pH concentration ranging from pH =2 to pH=12. With continued progress towards fabricating pH-ISFET devices, it is possible to fabricate an AM-based JISFET without much technological processes. Our numerical analysis provides the incentive for experimental exploration of the pH-ISFETs with Accumulation-Mode aspect.

References

- [1]. P. Bergveld, Development of an ion-sensitive solid state device for neurophysiological measurement, *IEEE Trans. Biomed. Eng. BME*, Vol. 21, 1974, pp. 485–487.
- [2]. T-M Pan, K-M Liao, Structural properties and sensing characteristics of Y₂O₃ sensing membrane for pH-ISFET, *Sensors and Actuators B*, Vol. 127, 2007, pp. 480–485.
- [3]. B. Premanode, N. Silawan, W P Chan, Chris T, A composite ISFET readout circuit employing current feedback, *Sensors and Actuators B*, Vol. 127, 2007, pp. 486–490.
- [4]. A. Morgenshtein, L. S-Boreysha, U. Dinnar, C. G. Jakobson, Y. Nemirovsky, CMOS readout circuitry for ISFET Microsystems, *Sens. Actuators B, Chem*, Vol. 9, 2004, pp. 122–131.
- [5]. T. M. Pan, C. H. Cheng, C. D. Lee, Yb₂O₃ thin films as a sensing membrane for pH-ISFET application, *J. Electrochem. Soc.*, Vol. 156, 2009, pp. 108–111.
- [6]. C. Y. Chen, J. C. Chou, H. T. Chou, Characteristics of cost-effective ultrathin HfTiOx film as sensitive membrane in ISFET fabricated by anodization, *J. Electrochem. Soc.*, Vol. 156, 2009, pp. 225–228.
- [7]. W-Y. Chung, C-H Yang, DG. Pijanowskac, P B. Grabiec, W. Torbicz, ISFET performance enhancement by using the improved circuit techniques, *Sensors and Actuators B*, Vol. 113, 2006, pp. 555–562.
- [8]. C-W. Lee, I. Ferain, A. Afzalian, R. Yan, N D. Akhavan, P. Razavi, J-P Colinge, Performance estimation of junctionless multigate transistors, *Solid-State Electron*, Vol. 54, 2010, pp. 97-103.
- [9]. J. P. Colinge, Multi-gate SOI MOSFETs, *Solid-State Electron*, Vol. 48, 2004, pp. 897-905.
- [10]. T-M. Pana, M-D. Huanga, C-W. Lina, M-H. Wub, Development of high-k HoTiO₃ sensing membrane for pH detection and glucose biosensing, *Sensors and Actuators B*, Vol. 144, 2010, pp. 139–145.
- [11]. ATLAS: 2D Device Simulator, *SILVACO International*, 2008.

New RADFET Dosimeter Design For Radioactive Environment Monitoring Applications

M. Meguellati, F. Djeflal, D. Arar, F. Douak and L. Khetache

Abstract— In this paper, a radiation sensitive FET (RADFET) dosimeter design (called the Dual-Dielectric Gate All Around DDGAA RADFET dosimeter) to improve the radiation sensitivity performance and its analytical analysis have been proposed for RADFET dosimeter-based applications (monitoring, robotics, medical sciences,...). The proposed device and the Artificial Neural Networks (ANNs) have been used to study and show the impact of the proposed dosimeter on the environment monitoring and remote sensing applications. The obtained results make the DDGAA RADFET dosimeter a promising candidate for environment monitoring applications.

Index Terms— dosimeter, RADFET, traps, irradiation, sensitivity, Genetic Algorithm, ANNs.

I. INTRODUCTION

The Gate All Around GAA MOSFETs have emerged as excellent devices to provide the electrostatic integrity needed to scale down transistors to minimal channel lengths, and allowing a continuous progress in digital and analog applications. In addition to a better electrostatics than the conventional bulk MOSFET, the use of these devices have advantages relative to the electronic transport, mainly due to (i) the reduced surface roughness scattering because the lower vertical electric field and (ii) the reduction of the Coulomb scattering because the film is made of undoped/low-doped silicon [1-5]. Design and modeling guidelines of GAA MOSFETs have been discussed in previous work [2-5]. Employing this design for environment monitoring applications (irradiation measurement) becomes more beneficial if the device is made in vertical cylindrical recrystallized silicon due to highly flexible process integration options. There have been several reports of MOSFETs fabricated in recrystallized silicon for high-density digital integrated circuits [5].

Radiation sensitive MOSFETs (RADFETs) have been focus of interest both from applications and fundamental research point of views. In electronic industry these devices are

considered as attractive alternatives for nuclear industry, space, radiotherapy and environment monitoring applications due to their reliability, low power consumption, non-destructive read-out of dosimetric information, high dose range, and compatibility to standard CMOS technology and on-chip signal processing [6-8]. The main RADFET disadvantage is the relatively low sensitivity. In this context, the submicron multi-gate design may be considered as attractive alternative to overcome this disadvantage because of the high electrical performance and reliability provided by the multi-gate structure in comparison with single-gate one. However, as semiconductor devices are scaled into the deep submicron domain, short-channel effects (SCEs) begin to plague conventional planar CMOS-based devices. To avoid the electrical constraints and improve the sensitivity performance, a new design and enhancement of conventional (bulk) RADFET become important. In this work, a new design of RADFET called the Dual-Dielectric Gate All Around (DDGAA) RADFET dosimeter, in which the manufacturing processes and sensitivity performances will be greatly improved, is proposed for deep submicron CMOS-based dosimeter applications. The (DDGAA) RADFET dosimeter design presented in this paper is basically surrounded dual-dielectric layers (SiO_2 and Si_3N_4) with low p-channel (Si) doping concentration. The results showed that the analytical model is in agreement with the 2-D numerical simulation over a wide range of device parameters. The proposed structure has been analyzed and validated by the good sensitivity and electrical performance obtained in deep submicron regime in comparison with the conventional (bulk) design. In addition, in this work, we present the applicability of genetic algorithm optimization (GA) approach to optimize the radiation sensitivity of the DDGAA RADFET for integrated CMOS-based dosimeters. Finally, the proposed dosimeter model was used to study and show the impact of the proposed design on the environment monitoring applications.

II. THEORY DEVELOPMENT AND MODEL DERIVATION

A. Interface potential analysis

Schematic cross-sectional view of the proposed (DDGAA) RADFET dosimeter is presented in Fig.1. The insulator consists of a thermal oxide (SiO_2) grown on a (100) n on n+ epitaxial silicon substrate (channel), and a low pressure CVD silicon nitride layer (Si_3N_4) deposited on top of the oxide. $N_{D/S}$ represents the doping level of the drain/source

Manuscript received Sep 17, 2012.

F. Djeflal is with the Department of Electronics, University of Batna, Batna 05000, Algeria (phone: 303-555-5555; fax: 303-555-5555; (e-mail: faycal.djeflal@univ-batna.dz, faycaldzd@hotmail.com).

M. Meguellati, D. Arar, F. Douak is with Department of Electronics, University of Batna, Batna 05000, Algeria; (e-mail: m_meguellati@yahoo.fr).

L. Khetache is with the Electrical Engineering Department, University of Batna, Batna 05000, Algeria.

region, respectively. The channel region is bounded by source and drain spacing at $x=0$ and L , respectively, where L is the gate length. With a negatively applied gate bias, holes generated in the SiO_2 layer are transported and trapped at the $\text{SiO}_2/\text{Si}_3\text{N}_4$ interface producing a measurable threshold-voltage shift as it is shown in Fig. 1. The investigation reported in this work for gamma radiation sources can also be applied qualitatively to other radiation sources (protons, electrons, ...).

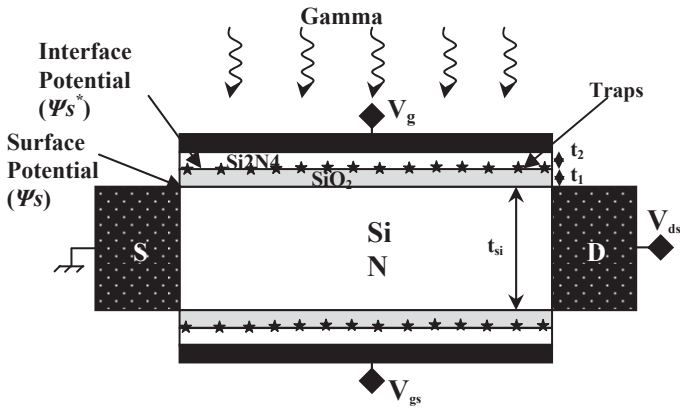


Fig 2. Cross-sectional view of the proposed DDGAA RADFET design

For deep submicron devices, the solution of 2D Poisson's equation satisfying suitable boundary conditions is required to model the interface potential. Refer to Fig. 1, the 2D Poisson's equation for the channel region is given by

$$\frac{1}{r} \frac{\partial}{\partial r} \left(r \frac{\partial \psi(r, x)}{\partial r} \right) + \frac{\partial^2 \psi(r, x)}{\partial x^2} = \frac{q \cdot N_D}{\epsilon_{si}} \quad (1)$$

The boundary conditions for $\psi(x, r)$ are found by satisfying continuity of both the normal component of the electric displacement at the (Si/SiO_2) interfaces, and the potential at the source/drain sides.

Using the same parabolic potential profile in vertical direction [2] and applying the symmetry condition of $\frac{\partial \psi}{\partial r} = 0$ for $r=0$, we obtained the following expressions of 2-D channel potential as

$$\psi(r, x) = \frac{C_{ox}}{\epsilon_{si} \cdot t_{si}} [V_g^* - \psi_s(x)] r^2 + \left(1 + \frac{C_{ox} t_{si}}{4 \epsilon_{si}} \right) \psi_s(x) - \frac{C_{ox} t_{si}}{4 \epsilon_{si}} V_g^* \quad (2)$$

where $\psi_s(x)$ represents the surface potential, C_{ox} represents the insulator capacitance ($C_{ox} = 2\pi\epsilon_1 L / \ln(1 + 2t_1/t_{si})$), t_{si} is the silicon thickness, the effective oxide and silicon nitride layer is defined as $t_{oxeff} = t_1 + t_2(\epsilon_1/\epsilon_2)$ with t_1 is the thickness of the SiO_2 ($\epsilon_1 = \epsilon_{ox}$) layer and t_2 is the thickness of the Si_3N_4 layer (ϵ_2), V_{bi} is the junction voltage between the source/drain and intrinsic silicon, $V_{bi} = (kT/q) \ln(N_{D/S}/n_i)$, n_i is the intrinsic silicon density, V_{ds} represents the drain-to-source voltage and k is the Boltzmann constant. V_g^* represents the effective voltage at the gate which is introduced to simplify notations and alleviate derivations for symmetric structure as $V_g^* = V_{gs} - V_{fb}$, with V_{fb} is the flat-band voltage.

Substituting (2) in (1), we obtain the differential equation that deals only with surface potential as

$$\frac{d^2 \psi_s(x)}{dx^2} - \frac{1}{\lambda^2} \psi_s(x) = D_1 \quad (3)$$

$$\text{with } \lambda = \sqrt{\frac{\epsilon_{si} \cdot t_{oxeff} \cdot t_{si}}{4 \cdot \epsilon_{ox}}} \text{ and } D_1 = \frac{q \cdot N_D}{\epsilon_{si}} - \frac{1}{\lambda^2} \cdot V_g^*$$

where λ represents the natural length of the analyzed (DDGAA) RADFET dosimeter. This parameter gives the scaling capability (downscaling ability) of the device. D_1 is a factor which represents the impact of the applied gate voltage and channel doping on the surface potential.

The differential equation that deals only with interface potential is given by

$$\frac{d^2 \psi_s^*(x)}{dx^2} - \frac{1}{\lambda^2} \psi_s^*(x) = D_2 \quad (4)$$

$$\text{with } D_2 = \alpha - \beta V_{gs}^* \text{ and } \alpha = \frac{q N_D \epsilon_2 t_1}{\epsilon_{si} (\epsilon_2 t_1 + \epsilon_1 t_2)}, \beta = \frac{\epsilon_2 t_1}{\lambda^2 (\epsilon_2 t_1 + \epsilon_1 t_2)}$$

where ψ_s^* represents the interface potential at $\text{SiO}_2/\text{Si}_3\text{N}_4$ interface which satisfies the continuity of the normal component of the electric displacement at the interface.

This resolution of this Equation allows us the calculation of the interface potential without (before) irradiation.

In the case of RADFET under irradiation new term should be introduced in order to include the radiation-induced interface-traps effect [2]. So, the parameter D_2 can be written, in this case, as, $D_2 = \alpha - \beta V_{gs}^* - q N_f / \epsilon_2 t_2$, with N_f represents the irradiation induced localized interface charge density per square area. The second term in this expression represents the impact of the irradiation induced localized interface charge density on the interface potential.

The surface and interface potentials can be, respectively, expressed as

$$\psi_s(x) = -\lambda^2 D_2 + \frac{\phi_D \sinh\left(\frac{x}{\lambda}\right) - \phi_S \sinh\left(\frac{x-L}{\lambda}\right)}{\sinh\left(\frac{L}{\lambda}\right)} \quad (5)$$

With $\phi_D = V_{ds} + \lambda^2 D_2$ and $\phi_S = V_{bi} + \lambda^2 D_2$

$$\psi_s^*(x) = \frac{\epsilon_1 t_2}{\epsilon_2 t_1 + \epsilon_1 t_2} V_{gs}^* + \frac{\epsilon_2 t_1 x}{\epsilon_2 t_1 + \epsilon_1 t_2} \psi_s(x) \quad (6)$$

B. Threshold voltage shift model

Schematic cross-sectional view of the proposed (DDGAA) RADFET The basic concept of RADFET dosimeter is to convert the threshold voltage shift, ΔV_{th} , induced by radiation, into absorbed radiation dose, where $\Delta V_{th} = V_{th} - V_{th0}$ with V_{th} and V_{th0} represent the threshold voltage after and before irradiation, respectively.

Based on the surface potential model given by Eq.(5), the threshold voltage can be derived using the condition of the minimum channel potential $\psi_{smin}|_{V_{gs}=V_{th}} = 2\phi_B$, with

$\psi_{smin} = \psi_s(x_{min})$, V_{th} is the threshold voltage value, and ϕ_B represents the bulk potential of silicon body given as $\phi_B = (K_B T / q) \cdot \ln(N_D / n_i)$. The location of the minimum

surface potential can be obtained analytically by solving $\frac{d\psi_s(x)}{dx} = 0$ [2].

The solution of the equation $\psi_{s\min}|_{V_{gs}=V_{th}} = 2\phi_B$ at low drain-source voltage for long channel lengths ($L \gg \lambda$) can be given as

$$V_{th} = \frac{\left(2A\phi_B + \lambda^2\alpha + \frac{qN_f}{\epsilon_2 t_2}\right) \sinh\left(\frac{L}{\lambda}\right) + (V_{bi} - V_{ds}) \sinh\left(\frac{L}{2\lambda}\right)}{\left(\beta\lambda^2 - \frac{B}{A}\right) \sinh\left(\frac{L}{\lambda}\right) - 2 \sinh\left(\frac{L}{2\lambda}\right)} \quad (7)$$

a)

$$\text{with: } A = \frac{\epsilon_1 t_2 - \epsilon_2 t_1}{\epsilon_1 t_2}, \quad B = \frac{\epsilon_2 t_1}{\epsilon_1 t_2}$$

$$V_{th0} = V_{th}|_{N_f=0} = \frac{\left(2A\phi_B + \lambda^2\alpha\right) \sinh\left(\frac{L}{\lambda}\right) + (V_{bi} - V_{ds}) \sinh\left(\frac{L}{2\lambda}\right)}{\left(\beta\lambda^2 - \frac{B}{A}\right) \sinh\left(\frac{L}{\lambda}\right) - 2 \sinh\left(\frac{L}{2\lambda}\right)}$$

(7b)

From (7a) and (7b), the threshold voltage shift can be given as

$$\Delta V_{th} = \frac{\frac{qN_f}{\epsilon_2 t_2} \sinh\left(\frac{L}{\lambda}\right)}{\left(\beta\lambda^2 - \frac{B}{A}\right) \sinh\left(\frac{L}{\lambda}\right) - 2 \sinh\left(\frac{L}{2\lambda}\right)} \quad (7c)$$

III. RESULTS AND DISCUSSION

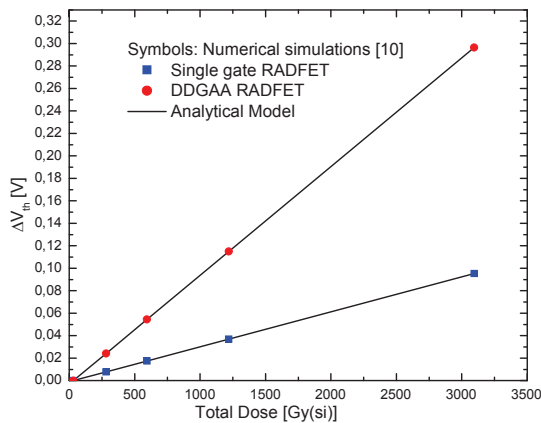


Fig 2. Variation of threshold voltage shift in function of the absorbed radiation dose for the conventional and DDGAA RADFET designs.

The RADFET radiation sensitivity S , given by [8,9]:

$$S = \frac{\Delta V_{th}}{D} \quad (9)$$

where D represents the absorbed radiation dose.

In Figure 2, the variation of DDGAA RADFET sensitivity versus the absorbed radiation dose, D , has been compared with conventional (bulk) RADFET. For both designs, the output response of the RADFETs is linear with absorbed radiation dose. It is clearly shown that DDGAA RADFET has higher sensitivity, $S = 95.45 \mu V / Gy$, in comparison with conventional RADFET design, $S = 30.68 \mu V / Gy$. This

means that DDGAA RADFET has better electrical and scaling performances in comparison with the conventional design. So, our design provides a high sensitivity, better electrical and technological performances in comparison with the conventional structure. These results make the proposed design as a promising candidate for CMOS-based dosimeters.

A. GA-based sensitivity optimization

GA optimization has been defined as finding a vector of decision variables satisfying constraints to give acceptable values to objective function. It has recently been introduced to study the complex and nonlinear systems and has found useful applications in engineering fields. Due to the simple mechanism and high performance provided by GA for global optimization, GA can be applied to find the best design of DDGAA RADFET in order to improve the radiation sensitivity by satisfying of the following objective function:

- Maximization of the RADFET radiation sensitivity $S(X)$

Where X represents the input normalized variables vector which is given as $X = (t_{si}, t_1, t_2, L)$.

For the purpose of GA-based optimization of the radiation sensitivity of DDGAA RADFET, routines and programs for GA computation were developed using MATLAB 7.2 and all simulations are carried out on a Pentium IV, 3GHz, 1GB RAM computer. For the implementation of the GA, tournament selection is employed which selects each parent by choosing individuals at random, and then choosing the best individual out of that set to be a parent. Scattered crossover creates a random binary vector. It then selects the genes where the vector is unity from the first parent, and the genes where the vector is zero from the second parent, and combines the genes to form the child. An optimization process was performed for 20 population size and maximum number of generations equal to 200, for which stabilization of the fitness function was obtained.

The steady decrease in objective function in each generation until it reaches a best possible value can be attributed to the selection procedure used namely Roulette wheel selection.

TABLE II
DDGAA RADFET DESIGN PARAMETERS

Symbol	Optimized design	Design without optimization	Conventional design
$L(nm)$	100	100	100
$t_{si}(nm)$	50	20	20
$t_1(nm)$	5	5	5
$t_2(nm)$	15	5	-
$S(\mu V/Gy)$	162.22	95.45	30.68

The radiation sensitivity values of the DDGAA RADFET with and without optimization are shown in Table. 1. It is clearly shows that The radiation sensitivity, for optimized design ($162.22 \mu V / Gy$) is better than the both conventional RADFET ($S = 30.68 \mu V / Gy$) and DDGAA RADFET without optimization ($S = 95.45 \mu V / Gy$).

B. Radioactive environment sensing

In order to show the impact of the proposed design on the radioactive environment monitoring, we propose the study of a contemned radioactive environment. This latter is considered a big challenge in the field of the environment monitoring. In this work, using simulated database (built from numerical data) of total dose radioactivity distribution in 2-D space and the Multi-Layer-Perceptron (MLP) tool, we will study a contemned environment by gamma radiation.

Artificial neural network (ANN) based methods have been widely used for modeling various complex and nonlinear processes (classification, speech recognition, and signal processing). The model based on artificial neural network [10-12] assumes that input and output patterns of a given problem are related by a set of neurons organized in hidden layers. The layers in these networks are interconnected by communication links that are associated with weights that dictate the effect on the information passing through them. These weights are determined by the learning algorithm.

The output of node j in the hidden layer is given by

$$h_j = g\left(\sum_{i=14}^n w_{ij} \cdot x_i + b_j\right)$$

And the output of the network by

$$y = \sum_{i=14}^k w_{oi} \cdot h_i$$

Where w_{ij} are the weights connecting the inputs to node j in the hidden layer, b_j is the bias to the node, and w_{oi} are the weights from the hidden to the output layer.

The activation function relates the output of a neuron to its input based on the neuron's input activity level. Some of the commonly used functions include: the threshold, piecewise linear, sigmoid, tangent hyperbolic, and the Gaussian function [11]. The learning process of the MLP network involves using the input-output data to determine the weights and biases. One of the most techniques used to obtain these parameters is the back-propagation algorithm [11– 13]. In this method, the weights and biases are adjusted iteratively to achieve a minimum mean square error between the network output and the target value.

The energy recorded by the sensor has to be transmitted, often in electronic form, to a receiving and processing station, where the data are processed into an image. Radiation that is not absorbed or scattered in the atmosphere can reach and interact with the Earth's surface. There are three forms of interaction that can take place when energy strikes, or is incident upon the surface [14].

In remote sensing, we are most interested in measuring the radiation reflected from targets. This reflection disgusting the image caption by the sensors (which are located at reception stations), we propose that interacting energy (noise) is a Gaussian noise.

In this work, the artificial neural network is used to denoising the image distorted by the transmission noise (Fig. 4). In this context, the database for MLP optimization consists of 49600 samples split into three categories: training, validation and test sets. The training and validation are used tune MLP configuration and the test is used to test the MLP configuration to denoise the different regions of the contemned environment. Test and training steps were

run for a given MLP structure to obtain the optimal MLP configuration. The database is collected from several RADFETs, which have been located in different regions in the contemned environment. In order to validate the denoising proprieties of the optimized MLP, test set is compared to the MLP response.

Fig.5 presents the space distribution of the gamma radiation in the investigated contemned environment after the denoising process. It is shown that the different regions are clearly represented. This last observation shows the applicability and the efficiency provided by the MLP-based approach to study the radioactive environment.

Fig. 6 shows that a good agreement between MLP and real results is found. Hence, the optimized structure can be used for the radioactive environment monitoring applications.



Fig. 4. The distorted image due to the transmission noise.

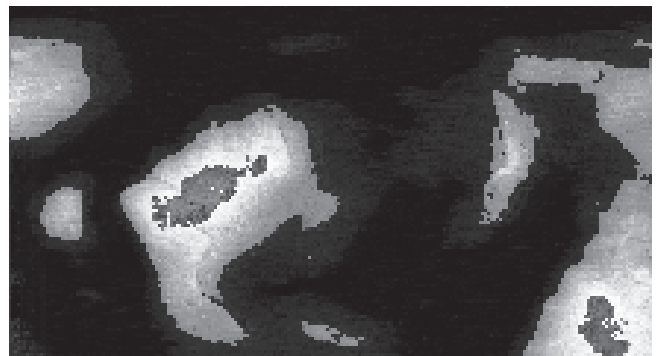


Fig. 5. The denoised image using MLP.

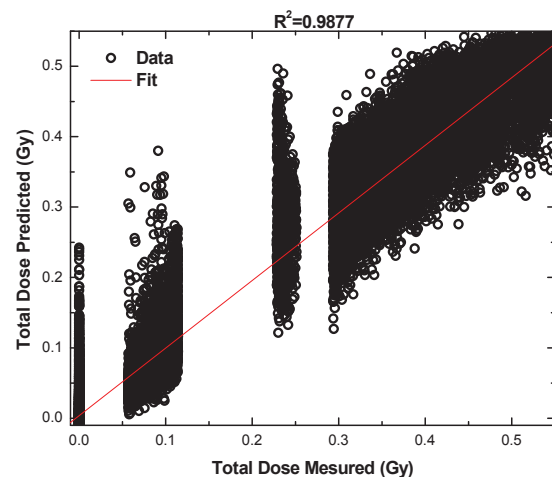


Fig. 6. Validation of the neural network result for test set.

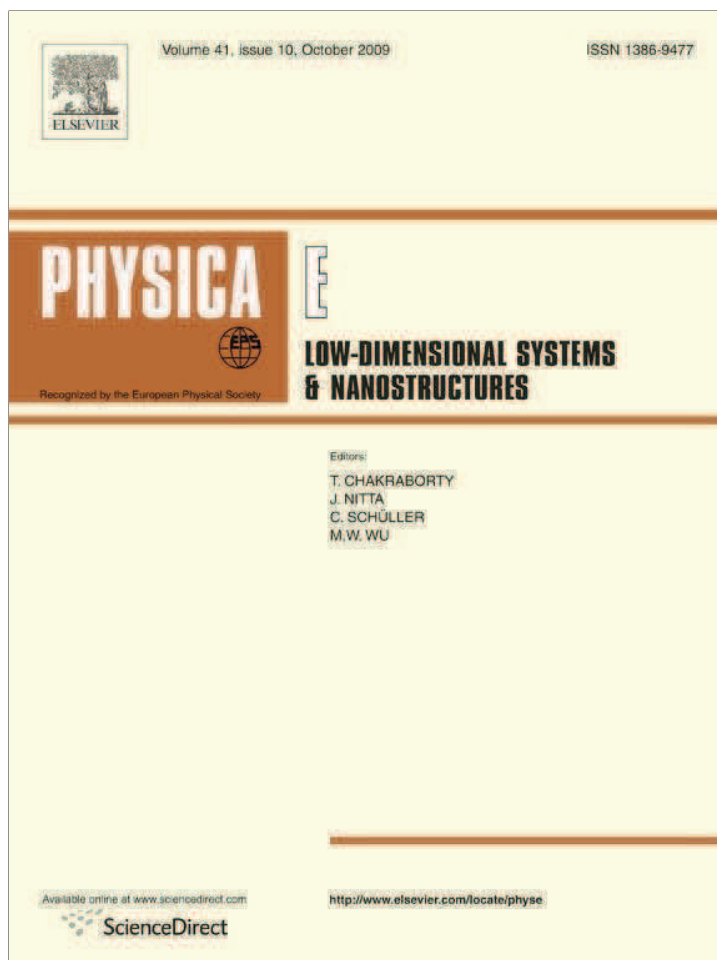
IV. CONCLUSION

In this paper, we compared new sensor design, DDGAA RADFET, with conventional planar RADFET through 2-D analytical investigation. A two-dimensional analytical analysis comprising radiation-induced interface-traps effect, 2D surface and interface potentials, threshold voltage shift and sensitivity model for DDGAA RADFET has been developed. The threshold voltage shift behavior of the proposed design was more effectively improved than those of the conventional planar RADFET. Also, we confirmed that DDGAA RADFET had advantages in CMOS scaling in comparison with planar RADFET. Application of the GA-based design approach to DDGAA RADFET has also been discussed. It can be concluded that proposed GA-based approach is efficient and gives the promising results. In order to show the impact of the proposed design on the radioactive environment monitoring, we developed a MLP-based approach to study a contaminated radioactive environment. The proposed approach can be used for remote sensing applications, where the information about the contaminated radioactive environment should be transmitted in electronic form to a receiving and processing station.

REFERENCES

- [1] The international technology roadmap for semiconductors (ITRS); 2007. <[http:// public.itrs.net](http://public.itrs.net)>.
- [2] Z. Ghoggali, F. Djeflal, N. Lakhdar, Analytical analysis of nanoscale Double- Gate MOSFETs including the hot-carrier degradation effects, *Int. J. Electronics*, pp. 119-127, 97(2), 2010.
- [3] D. Jiménez, B. Iñiguez, J. Suñé, L.F. Marsal, J. Pallarès, J. Roig and D. Flores, Continuous Analytic I-V Model for Surrounding-Gate MOSFETs, *IEEE Electron Devices Letters*, Vol.25, pp. 571-573, 2004.
- [4] H. Kaur, S. Kabra, S. Haldar and R.S. Gupta, An analytical drain current model for graded channel cylindrical/surrounding gate MOSFET, *Microelectronics Journal*, vol. 38, pp. 352-359, 2007.
- [5] MA. Abdi , F. Djeflal, D.Arar, ML. Hafiane, Numerical analysis of Double Gate and Gate All Around MOSFETs with bulk trap states. *J Mater Sci: Mater Electron*, vol. 19, pp. S248-S253, 2008.
- [6] F. Djeflal, T. Bendib, M. Meguellati, D. Arar and M.A Abdi, New Dual-Dielectric Gate All Around (DDGAA) RADFET Dosimeter Design to Improve the Radiation Sensitivity, *Proceedings of the World Congress on Engineering 2012 Vol II WCE 2012*, July 4 - 6, 2012, London, U.K., pp. 917-921.
- [7] A. Kelleher, W. Lane, L. Adams, A design solution to increasing the sensitivity of pMOS dosimeters: The stacked RADFET approach, *IEEE Trans. Nuclear Science*, vol. 42, pp.48-51, 1995.
- [8] A. Jaksic, G. Ristic, M. Pejovic, A. Mohammadzadeh, C. Sudre, W. Lane, Gamma-ray irradiation and post-irradiation responses of high dose range RADFETs, *IEEE Trans. Nuclear. Science*, vol. 49, pp. 1356-1363, 2002.
- [9] J.R. Schwank, S.B. Roeske, D.E. Beutler, D. J. Moreno, M.R. Shaneyfelt, *IEEE Trans. Nuclear Science*, vol. 43, pp. 2671-2678, 1996.
- [10] Atlas User's manual, SILVACO TCAD, 200
- [11] Guessasma S, Ghislain M, Christain C. Modeling of the APS plasma spray process using artificial neural networks: basis requirements and an example. *Comput Mater Sci* 2004;29:315.
- [12] F. Djeflal, M. Chahdi, A. Benhaya, M.L. Hafiane. An approach based on neural computation to simulate the nanoscale CMOS circuits: Application to the simulation of CMOS inverter. *Solid-State Electronics* 51 (2007) 48-56.
- [13] Taylor JG. *Neural networks and their applications*. West Sussex (UK): John Wiley & Sons Ltd.; 1996.
- [14] A Canada Centre for Remote Sensing, Remote Sensing Tutorial, available on line for free http://www.uprm.edu/biology/profs/chinea/gis/g06/NRC1_1_1_5.pdf.

Provided for non-commercial research and education use.
Not for reproduction, distribution or commercial use.

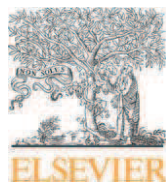


This article appeared in a journal published by Elsevier. The attached copy is furnished to the author for internal non-commercial research and education use, including for instruction at the authors institution and sharing with colleagues.

Other uses, including reproduction and distribution, or selling or licensing copies, or posting to personal, institutional or third party websites are prohibited.

In most cases authors are permitted to post their version of the article (e.g. in Word or Tex form) to their personal website or institutional repository. Authors requiring further information regarding Elsevier's archiving and manuscript policies are encouraged to visit:

<http://www.elsevier.com/copyright>



A two-dimensional analytical analysis of subthreshold behavior to study the scaling capability of nanoscale graded channel gate stack DG MOSFETs

F. Djeflal*, M. Meguellati, A. Benhaya

LEA, Department of Electronics, University of Batna, Batna 05000, Algeria

ARTICLE INFO

Article history:

Received 12 February 2009

Received in revised form

6 August 2009

Accepted 7 August 2009

Available online 15 August 2009

PACS:

85.35.-p

85.40.-e

02.60.-Pn

85.30.De

85.30.-z

Keywords:

Nanoscale MOSFETs

GCGS DG MOSFET

Short-channel-effects

Subthreshold behavior

ABSTRACT

In this paper, a new nanoscale graded channel gate stack (GCGS) double-gate (DG) MOSFET structure and its 2-D analytical model have been proposed, investigated and expected to suppress the short-channel-effects (SCEs) and improve the subthreshold performances for nanoelectronics applications. The model predicts a shift, increasing potential barrier, in the surface potential profile along the channel, which ensures a reduced threshold voltage roll-off and DIBL effects. In the proposed structure, the subthreshold current and subthreshold swing characteristics are greatly improved in comparison with the conventional DG MOSFETs. The developed approaches are verified and validated by the good agreement found with the numerical simulation. (GCGS) DG MOSFET can alleviate the critical problem and further improve the immunity of SCEs of CMOS-based devices in the nanoscale regime.

Crown Copyright © 2009 Published by Elsevier B.V. All rights reserved.

1. Introduction

The inherent benefits of MOSFET scaling are the speed improvement and the energy reduction which are associated with a binary-logic transition [1]. As the MOSFET is scaled below the 100 nm technology node, the advantages of MOSFET are diminished by the short-channel-effects (SCEs) [1,2]. These effects lead to the scaling limitations on conventional planar single gate MOSFETs. To overcome these limitations and realize high-performance MOS transistors, a new multi-gate transistor called double-gate MOSFET has been proposed as potential candidate for nanoscale CMOS-based circuits' design [1–5]. But, the continued scaling of SiO₂-based gate dielectrics leads to a large gate leakage and therefore, DG MOSFET performances can be degraded [4]. To minimize short-channel-effects and maintain full depletion and improved drain current, a new design and improvement of conventional DG MOSFETs become important. In this work, a new design of DG MOSFET called graded channel gate stack (GCGS) double-gate (DG) MOSFET, in which the gate leakage and SCEs will be greatly improved, is proposed for the future ULSI

circuits. In the proposed design, the average electric field under the gate further increases and the high density of interface trap states can be reduced using a gate stack structure [6–8]. Also, the incorporation of the step-function profile in channel doping can improve the breakdown voltage behavior in comparison with conventional fully depleted SOI MOSFETs devices for wide temperature range [9].

In this paper, we have developed a new analytical compact subthreshold behavior model comprising 2-D channel potential, threshold voltage, drain induced barrier lowering effect (DIBL), subthreshold current and subthreshold swing factor in order to explain the advantages of the proposed (GCGS) DG MOSFET over the conventional DG MOSFET with the same geometric specifications that allow us to utilize the benefits of the incorporation of both, the graded channel and high-k layer, aspects on the immunity of the proposed design against the short-channel-effects. The results so obtained are in close proximity with the simulated results thus confirming the validity of the proposed model.

This paper is organized as follows. Section 2 presents the modeling methodology of the subthreshold performances for the proposed design. Section 3 gives the obtained modeling results and discussion. Finally the conclusion is given in Section 4.

* Corresponding author. Tel.: +213 773796503; fax: +213 333805494.
E-mail address: faycaldzdz@hotmail.com (F. Djeflal).

2. Model formulation

2.1. Surface potential

A cross-sectional view of nanoscale graded channel gate stack (GCGS) DG MOSFET is shown in Fig. 1. The step-function graded channel doping distribution region is presented in Region I with a length of L_1 where N_{AH} and N_{AL} represent the high and low doping concentrations for both regions, respectively, L is the channel length of the DG MOSFET. The structure is symmetric, with a double-layer gate stack, oxide and high-k layers, with no overlap with the source extensions. ND/S represents the doping level of the drain/source region, respectively. Refer to Fig. 1, the Poisson's equation for both regions is given by

$$\text{Region I : } \frac{\partial^2 \psi(x, y)}{\partial x^2} + \frac{\partial^2 \psi(x, y)}{\partial y^2} = \frac{q N_{AL}}{\epsilon_{si}} \quad (1a)$$

$$\text{Region II : } \frac{\partial^2 \psi(x, y)}{\partial x^2} + \frac{\partial^2 \psi(x, y)}{\partial y^2} = \frac{q N_{AH}}{\epsilon_{si}} \quad (1b)$$

where the electrostatic potential $\psi(x, y)$ is referenced to the Fermi level, q represents the electronic charge and ϵ_{si} the silicon permittivity. The boundary conditions for ψ are found by satisfying the continuity of both the potential and the normal component of the electric displacement at the (Si/SiO₂)

interfaces, and the continuity of the potential at the source/drain sides

$$\epsilon_{ox} \frac{V_{F,eff} - \psi(x, 0)}{t_{oxeff}} = \epsilon_{si} \frac{\partial \psi(x, y)}{\partial y} \Big|_{y=0} \quad (2a)$$

$$\epsilon_{ox} \frac{V_{B,eff} - \psi(x, t_{si})}{t_{oxeff}} = \epsilon_{si} \frac{\partial \psi(x, y)}{\partial y} \Big|_{y=t_{si}} \quad (2b)$$

$$\psi(0, y) = V_{bi} \quad (2c)$$

$$\psi(L, y) = V_{bi} + V_{ds} \quad (2d)$$

where ϵ_{ox} is the oxide permittivity, t_{si} the thickness of silicon channel, V_{bi} the junction voltage between the source/drain and the intrinsic silicon, $V_{bi} = (kT/q) \ln(N_{D/S}/n_i)$, n_i the intrinsic silicon density and V_{ds} the drain-to-source voltage. t_{oxeff} is the effective oxide layer thickness of the insulator layer, oxide and high-k layers, and is defined as

$$t_{oxeff} = t_1 + \frac{\epsilon_1}{\epsilon_2} t_2 \quad (3a)$$

where t_1 is the thickness of the SiO₂ ($\epsilon_{ox} = \epsilon_1$) layer and t_2 is the thickness of the high-k layer (ϵ_2).

$V_{F,eff}$ and $V_{B,eff}$, represent the effective voltages at the front and bottom gates which are introduced to simplify notations and alleviate derivations for symmetric structure as follows:

$$V_g^* = V_{F,eff} = V_{B,eff} = V_{gs} - \phi_{MS} \quad (3b)$$

where ϕ_{MS} is the gate work function is referenced to the intrinsic silicon and V_{gs} represents the gate source voltage. For the symmetric structure, the electric field in the vertical (y) direction is symmetric with respect to $y = t_{si}/2$.

Following the approach developed by young [10], the potential distribution in the silicon film in the two regions is assumed to be a parabolic profile and is written as

$$\psi(x, y) = a(x) + b(x)y + c(x)y^2 \quad (4a)$$

Applying the boundary conditions (Eqs. (2a)–(2d) and $\partial \psi / \partial y = 0$, the symmetry condition of the structure, for $y = t_{si}/2$), we obtained the following expression of 2-D channel potential:

$$\psi(x, y) = \psi_s(x) + \frac{\epsilon_{ox} \psi_s(x) - V_g^*}{\epsilon_{si} t_{oxeff}} y - \frac{\epsilon_{ox} \psi_s(x) - V_g^*}{\epsilon_{si} t_{oxeff} t_{si}} y^2 \quad (4b)$$

where $\psi_s(x)$ represents the surface potential at Si/SiO₂ interfaces.

Substituting Eq. (4b) in Eqs. (1a)–(1b), we obtain the differential equation that deals only with the surface potential in the regions I and II as

$$\text{Region I : } \frac{d^2 \psi_{s1}(x)}{dx^2} - \frac{1}{\lambda^2} \psi_{s1}(x) = D_1$$

$$\text{Region II : } \frac{d^2 \psi_{s2}(x)}{dx^2} - \frac{1}{\lambda^2} \psi_{s2}(x) = D_2$$

with $\lambda = \sqrt{\epsilon_{si} t_{oxeff} t_{si} / 2 \epsilon_1}$, $D_1 = (q N_{AL} / \epsilon_{si}) - (1/\lambda^2) V_g^*$ for Region I, and $D_2 = (q N_{AH} / \epsilon_{si}) - (1/\lambda^2) V_g^*$ for Region II.

In Region I ($0 \leq x \leq L_1$), the boundary conditions of the surface potential (Fig. 1) are given as

$$\psi_{s1}(x = 0) = V_{bi} \quad (5a)$$

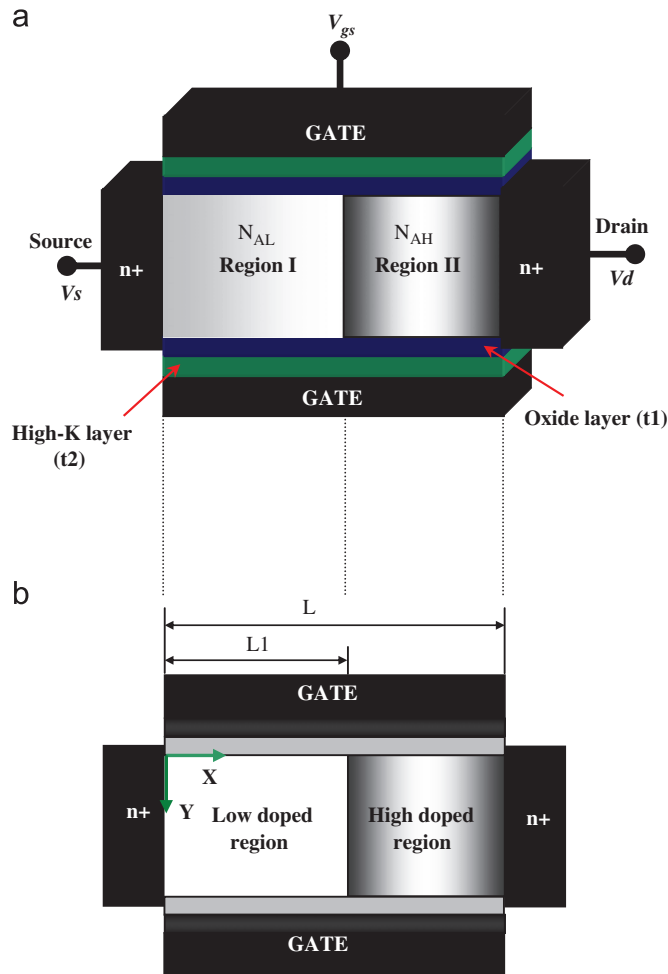


Fig. 1. (GCGS) DG MOSFET: (a) 3-D structure, (b) cross-sectional view through the channel.

$$\psi_{s1}(x = L_1) = V_p \quad (5b)$$

Using the Boundary conditions Eqs. (5a) and (5b), the surface potential in the first Region can be expressed as

$$\psi_{s1}(x) = -\lambda^2 D_1 + \frac{\phi_{D1} \sinh(x/\lambda) - \phi_{s1} \sinh((x - L_1)/\lambda)}{\sinh(L_1/\lambda)} \quad (6)$$

with $\phi_{D1} = V_p + \lambda^2 D_1$ and $\phi_{s1} = V_{bi} + \lambda^2 D_1$

In Region II ($L_1 \leq x \leq L$), the Boundary conditions of the surface potential (Fig. 1) are given as

$$\psi_{s2}(x = L_1) = V_p \quad (7a)$$

$$\psi_{s2}(x = L) = V_{bi} + V_{ds} \quad (7b)$$

Using Eqs. (7a) and (7b), the surface potential in the second region can be expressed as

$$\psi_{s2}(x) = -\lambda^2 D_2 + \frac{\phi_{s2} \sinh(x - L_1/\lambda) - \phi_{D2} \sinh(x - L/\lambda)}{\sinh(L - L_1/\lambda)} \quad (8)$$

with $\phi_{D2} = V_p + \lambda^2 D_2$ and $\phi_{s2} = V_{bi} + V_{ds} + \lambda^2 D_2$

V_p is the potential developed at the boundary of low doping channel and high doping regions. Using the continuity equation of the electric field at $x = L_1$, the value of this potential can be derived from

$$\left. \frac{\partial \psi_{s1}}{\partial x} \right|_{x=L_1} = \left. \frac{\partial \psi_{s2}}{\partial x} \right|_{x=L_1}$$

2.2. Threshold voltage

To evaluate the short-channel-effects parameters (threshold voltage roll-off, subthreshold current and subthreshold swing), we need to find the potential minimum along the channel. The position of minimum surface potential, x_{min} , is calculated by differentiating Eqs. (6) and (8) for both regions and equating the resulting expressions to zero. The position of the minimum surface potential and minimum surface potential are then obtained from Eqs. (6) and (8) for both regions as

$$x_{min1} = \frac{1}{2} \left[L - \lambda \ln \left(\frac{\phi_{s1} - \phi_{D1} e^{L_1/\lambda}}{\phi_{D1} - \phi_{s1} e^{L_1/\lambda}} \right) \right] \quad (9a)$$

$$\psi_{s1min} = -\lambda^2 D_1 + \frac{\phi_{D1} \sinh(x_{min1}/\lambda) - \phi_{s1} \sinh((x_{min1} - L_1)/\lambda)}{\sinh(L_1/\lambda)} \quad (9b)$$

$$x_{min2} = \left(\frac{L + L_1}{2} \right) + \frac{\lambda}{2} \ln \left(\frac{\phi_{D2} e^{L/\lambda} - \phi_{s2} e^{L_1/\lambda}}{\phi_{s2} e^{L/\lambda} - \phi_{D2} e^{L_1/\lambda}} \right) \quad (10a)$$

$$\psi_{s2min} = -\lambda^2 D_2 + \frac{\phi_{s2} \sinh((x_{min2} - L_1)/\lambda) - \phi_{D2} \sinh((x_{min2} - L)/\lambda)}{\sinh((L - L_1)/\lambda)} \quad (10b)$$

It is important to note that the minimum surface potential is defined as

$$\psi_{smin} = \min(\psi_{s1min}, \psi_{s2min}) \quad (11)$$

The threshold voltage, V_{th} , can be obtained by equating the minimum surface potential ψ_{smin} to $2\phi_B$ with ϕ_B represents the bulk potential of the silicon body given as, $\phi_B = (kT/q) \ln(N_{CH}/n_i)$

where N_{CH} represents the channel doping ($N_{CH} = N_{AL}$ in the first region and $N_{CH} = N_{AH}$ in the second region).

On solving $\psi_{smin} = 2\phi_B$, numerically, the threshold voltage can be calculated.

2.3. Subthreshold current

The current density primarily flows from the drain to the source and consists of both terms of drift current and diffusion current. The developed 2-D potential model can be used to drive an explicit analytical current equation in the subthreshold regime. For this, we follow the procedure proposed for 4-T and 3-T double-gate MOSFETs [11]. In the weak inversion region, the current is principally diffusion dominated and proportional to the electron concentration at the virtual cathode. Therefore, the subthreshold current derived for our (GCCS) DG MOSFET can be expressed as

$$J_n(y) = qD_n \frac{n_{min}(y)}{L} (1 - e^{-V_{ds}/V_t}) \quad (12)$$

where D_n represents the diffusion constant and V_t the thermal voltage. To evaluate the subthreshold current, we need to find the carrier concentration, $n_{min}(y)$, at the point along the channel where the potential is minimum. Since the minimum potential $\psi_{min}(y)$ varies with distance from the two gates, we can obtain the value of the minimum potential by replacing x_{min} in Eq. (4b) [5].

Using Boltzmann distribution, the electron density at virtual cathode can be written as

$$n_{min}(y) = (n_i^2 / N_{CH}) e^{\psi_{min}(y)/V_t} \quad (13)$$

The proposed structure (Fig. 1) can be considered as two gate stack (GS) DG MOSFETs, both devices are given by the first and the second region, respectively. It is clear that both devices are biased by two different voltages which are: V_p for the first (GS) DG MOSFET, and $V_{ds} - V_p$ for the second one. In the weak inversion domain, the subthreshold current for each region can be obtained by integrating Eq. (12) along the silicon film [11] taking into account the biasing voltage of each device. So, the total subthreshold current in our study can be given as

$$I_{sub} = I_{sub1} + I_{sub2} \quad (14)$$

with I_{sub1} and I_{sub2} represent the subthreshold current for the first and second region, respectively, given as

$$I_{sub1} = 2 \frac{K_1 V_t}{E_s} (e^{\psi_{min}/V_t} - e^{\psi_{min}^s/V_t}) \quad (15a)$$

$$I_{sub2} = 2 \frac{K_2 V_t}{E_s} (e^{\psi_{min}/V_t} - e^{\psi_{min}^s/V_t}) \quad (15b)$$

where E_s represents the constant electric field, $E_s = 2(\psi_{min} - \psi_{min}^s)/t_{si}$, ψ_{min}^s is the minimum potential at (Si/SiO₂) interface given by $\psi_{min}^s = \psi_{min}(x_{min}, 0)$, ψ_{min} represents the minimum potential, $\psi_{min} = \psi(x_{min}, t_{si}/2)$ and K_i a constant defined as $K_1 = (q\mu_n W V_t n_i^2 / L_1 N_{AL})(1 - e^{-V_p/V_t})$ and $K_2 = (q\mu_n W V_t n_i^2 / (L - L_1) N_{AH})(1 - e^{-(V_{ds} - V_p)/V_t})$, with W is the width of the (GCCS) DG MOSFET.

2.4. Subthreshold swing model

Assuming that the drain current, I_{ds} , is proportional to the total amount of the free carrier at the virtual cathode and their density $n_{min}(y)$ follows the Boltzmann distribution function (13), a general

subthreshold swing (S) model is obtained [3,5,10,12,13] as

$$S = \frac{\partial V_{gs}}{\partial \log I_{ds}} = \left[\frac{\int_0^{t_{si}/2} \exp(\psi_{\min}/Vt) (\partial \psi_{\min} / \partial V_{gs}) dy}{\int_0^{t_{si}/2} \exp(\psi_{\min}/Vt) dy} \right]^{-1} Vt \ln(10) \quad (15c)$$

An approximate solution of the integral (15c) given [10] as,

$$S = \frac{kT}{q} \ln(10) \left[\frac{\partial \psi_{\min}}{\partial V_{gs}} \right]^{-1} \quad (15d)$$

Therefore, a closed form expression for subthreshold swing for our (GCGS) DG MOSFET, in the case of $\psi_{\min} = \psi_{s1\min}$ where the minimum position is located in the first region, is obtained as

$$S = \frac{kT}{q} \ln(10) \left[1 + \frac{(\alpha + \beta) - \sinh(L_1/\lambda) - \sinh((L - L_1)/\lambda) - \sinh(L/\lambda)}{\sinh(L_1/\lambda)} \gamma + \sinh((x_{\min1} - L_1)/\lambda) \right]^{-1} \quad (15e)$$

with $\alpha = \sinh(L_1/\lambda) \cosh((L_1 - L)/\lambda)$, $\beta = \sinh((L - L_1)/\lambda) \cosh(L_1/\lambda)$ and $\gamma = ((\sinh(x_{\min1}/\lambda))/(\sinh(L/\lambda)))$

For long channel devices ($L \gg \lambda$) a simple new analytical subthreshold swing model can be expressed as

$$S = \frac{kT}{q} \ln(10) \left[1 + \frac{\sinh((x_{\min1} - L_1)/\lambda)}{\sinh(L_1/\lambda)} \right]^{-1} \quad (15f)$$

In addition, for short-channel conventional DG MOSFETs, $L_1 = L$ and $\varepsilon_2 = \varepsilon_1$, a new simple compact model can be given as

$$S = \frac{kT}{q} \ln(10) \left[1 + \frac{\sinh((x_{\min} - L)/\lambda) - \sinh(x_{\min}/\lambda)}{\sinh(L/\lambda)} \right]^{-1} \quad (15g)$$

The developed compact subthreshold swing has been used to plot a graphical abacus to study the scaling capability of the proposed (GCGS) DG MOSFET structure.

3. Results and discussion

Fig. 2 shows the variation of surface potential along the channel for (GCGS) DG MOSFET for $L = 20$ nm. It can be seen that the incorporation of GCGS design introduces an increasing of the potential barrier with the increasing of high-k layer dielectric permittivity ε_2 (Fig. 2a). But, this potential barrier is decreased when the high-k thickness (t_2) is increased (Fig. 2b). The shift in the potential profile screens the region near the source end from the variations in drain voltage and thus ensures reduction in threshold voltage roll-off in comparison with conventional DG MOSFETs. Thus, gate stack oxide acts as a controlling gate oxide. Fig. 3 compares the threshold voltage roll-off at drain source bias ($V_{ds} = 0.3$ V) for different lengths for conventional and (GCGS) DG MOSFETs. It is shown that the threshold voltage roll-off effect is considerably reduced in case of (GCGS) DG MOSFET even for channel lengths down to 10 nm. Moreover, due to the improved gate controllability, (GCGS) DG MOSFET has a lower threshold voltage as compared to conventional DG MOSFET which makes it suitable for nanoelectronics digital applications. Fig. 4 shows the variation of DIBL with channel length for different high-k dielectric constant for different DG MOSFETs structures. The DIBL is obtained from the difference between the threshold

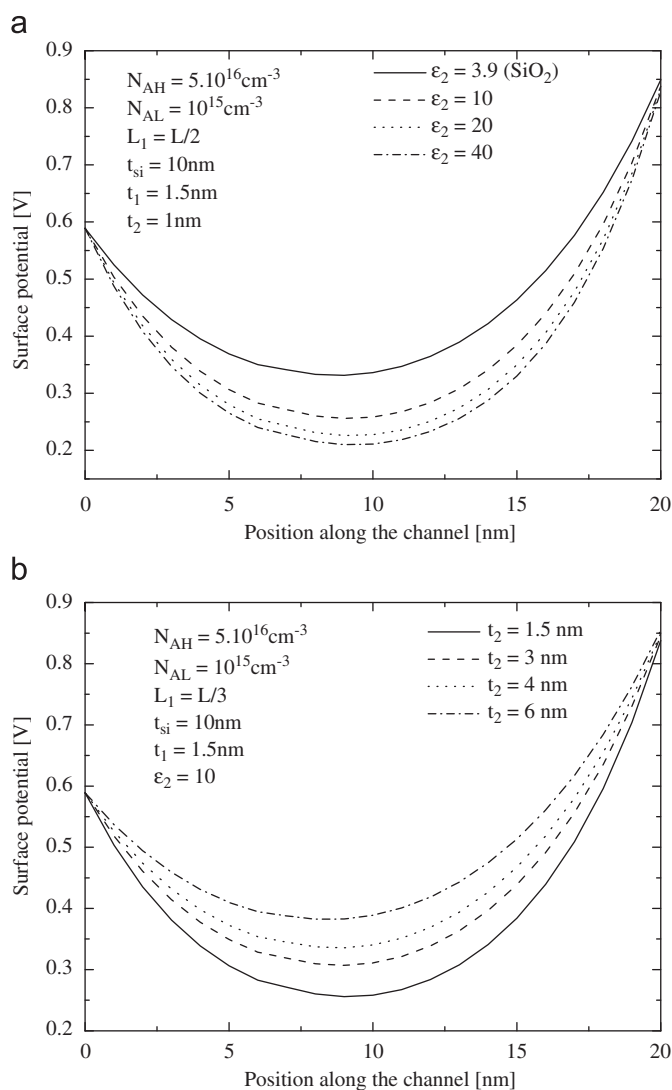


Fig. 2. Variation of surface potential along the channel for a 20 nm (GCGS) DG MOSFET as function of: (a) high-k thickness, t_2 , and (b) dielectric permittivity (ε_2).

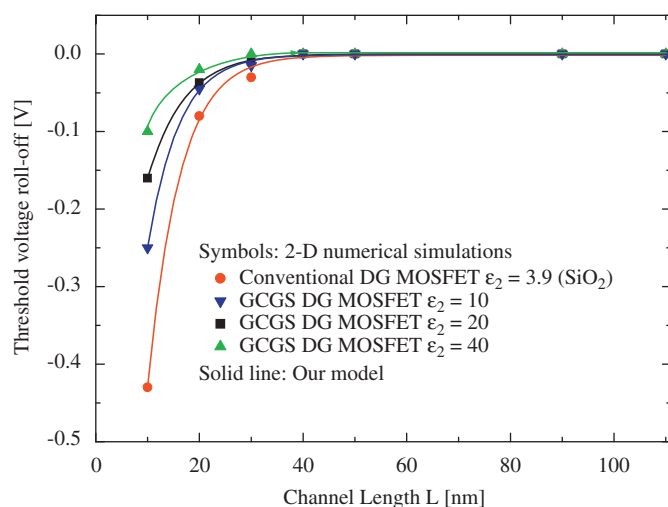


Fig. 3. Calculated threshold voltage roll-off for conventional and (GCGS) DG MOSFETs as function channel length (L) and dielectric permittivity (ε_2) ($L_1 = L/3$, $t_1 = 1$ nm, $t_2 = 1.5$ nm, $t_{si} = 10$ nm, $N_{AH} = 5.10^{16} \text{ cm}^{-3}$ and $N_{AL} = 10^{15} \text{ cm}^{-3}$).

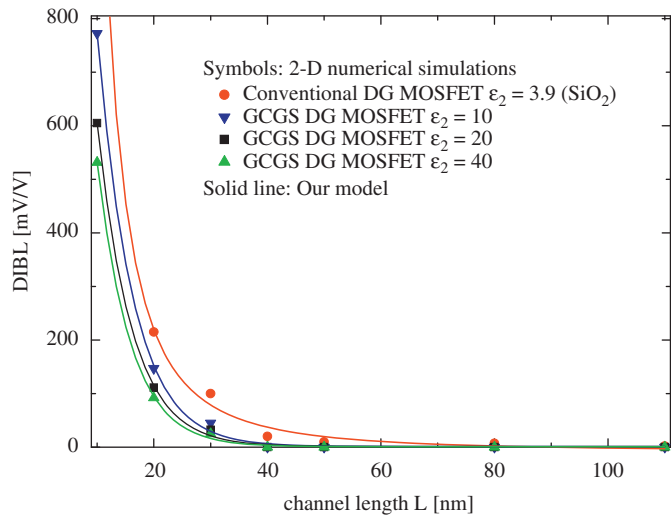


Fig. 4. Drain induced barrier lowering, DIBL, coefficient as function of channel length, for different dielectric constants (ϵ_2) ($L_1 = L/3$, $t_1 = 1$ nm, $t_2 = 1.5$ nm, $t_{si} = 10$ nm, $N_{AH} = 5.10^6$ cm⁻³ and $N_{AL} = 10^{15}$ cm⁻³).

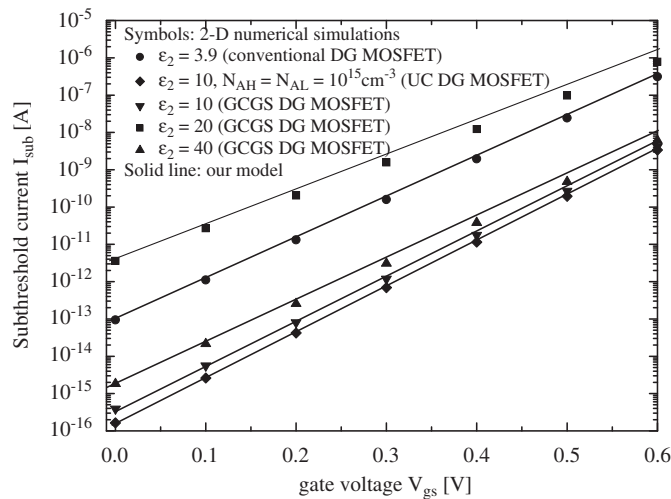


Fig. 5. Subthreshold current variation for different dielectric constants (ϵ_2) ($L = 20$ nm, $L_1 = L/2$, $t_1 = 1$ nm, $t_2 = 1.5$ nm, $t_{si} = 10$ nm, $N_{AH} = 5.10^6$ cm⁻³ and $N_{AL} = 10^{15}$ cm⁻³).

voltage at high drain–drain source voltage value (0.3 V) and the threshold voltage value at low drain–drain source voltage value (0.1 V). From Fig. 4, it can be shown that DIBL is lowest for (GCGS) DG MOSFET design as compared to conventional structure which indicates the fact that the incorporation of graded channel and high-k designs lead to an improvement of short-channel-effects.

In Fig. 5, the variation of subthreshold current with gate voltage for different high-k dielectric constants has been compared with conventional and uniform doped channel devices (UC DG MOSFET). Here, again, good agreement is obtained with simulation results using Silvaco and nanoMOS2.5 numerical simulators tools [14]. It is clearly shown that the subthreshold current reduces as the dielectric constant, ϵ_2 , and high doping value, N_{AH} , are increased. For conventional DG MOSFET, the OFF-state current is no longer negligible and contributes to standby power where the ratio I_{on}/I_{off} calculated in this case equal to 0.25×10^6 . In the case of (GCGS) DG MOSFET, we have found that the subthreshold current is greatly reduced and the ratio I_{on}/I_{off} increased to 15×10^6 . It is to note that the

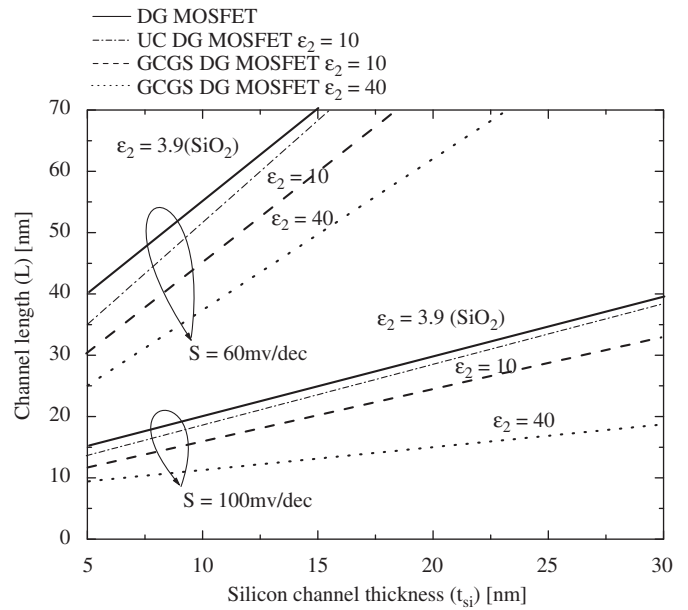


Fig. 6. Graphical abacus which allows studying the scaling capability of the proposed (GCGS) DG MOSFET design.

device with a low leakage current and high ratio, I_{on}/I_{off} , can provide the circuit with high quality commutation from OFF-state to ON-state when it is in digital operation for ULSI application. Therefore, the proposed (GCGS) DG MOSFET design can be considered as a potential candidate for nanoscale CMOS-based digital circuits. Fig. 6 shows the evolution of the subthreshold swing for different structures, where the effect of the (GCGS) design on the law of scaling capability of the DG MOSFET is presented. Clearly, 10 nm (GCGS) DG MOSFETs are likely to be used for the condition where $S = 100$ mV/dec is tolerable. For equal electrical and geometrical parameters, the (GCGS) DG MOSFETs provide a better subthreshold swing and a smaller OFF-current with respect to conventional and UC DG MOSFETs. In addition, it has been found that the scaling capability is improved and the minimal channel length of (GCGS) DG MOSFET is reduced to 37% for $S = 60$ mV/dec. Therefore, in (GCGS) DG MOSFET, the graded channel and high-k design in which the doping is kept low at near the source side and high near the drain end provides excellent immunity against the short-channel-effects and enhancement in subthreshold swing compared to the uniformly doped and conventional devices.

4. Conclusion

In this paper, 2-D subthreshold behavior model has been developed for (GCGS) DG MOSFET. It has been shown that the incorporation of the step-function profile in channel doping and the introduction of high-k region on the oxide layer exhibit an improvement in the screening of the drain potential variation, and reduced short-channel-effects. The law of scaling capability of the proposed structure was compared to the conventional double-gate case, illustrating the improved subthreshold behavior of the (GCGS) DG MOSFET over DG MOSFETs. The obtained results have been verified and validated using numerical simulators. As device dimensions penetrate into the nanoscale regime, the improved obtained performances make (GCGS) DG MOSFETs a better choice for future nanoscale CMOS-based devices.

References

- [1] F. Djéffal, Z. Dibi, M.L. Hafiane, D. Arar, *Materials Science and Engineering C* 27 (2007) 1111.
- [2] F. Djéffal, M. Chahdi, A. Benhaya, M.L. Hafiane, *Solid-State Electronics* 51 (2007) 48.
- [3] Q. Chen, B. Agrawal, J.D. Meindl, *IEEE Transactions on Electron Devices* 49 (2002) 1086.
- [4] F. Djéffal, Z. Ghoggali, Z. Dibi, N. Lakhdar, *Microelectronics Reliability* 49 (2009) 377.
- [5] H. Abd El-hamid, J.R. Guitart, B. Iñíguez, *IEEE Transactions on Electron Devices* 54 (2007) 1402.
- [6] M. Saxena, S. Haldar, M. Gupta, R.S. Gupta, *Solid-State Electronics* 47 (2003) 2131.
- [7] H. Kaur, S. Kabra, S. Haldar, R.S. Gupta, *Solid-State Electronics* (2008) 305.
- [8] A. Inani, R.V. Rao, B. Cheng, J. Woo, *Japanese Journal of Applied Physics* 38 (1999) 2266.
- [9] M. Galetti, M.A. Pavanello, J.A. Martino, *Microelectronics Journal* 37 (2006) 601.
- [10] K.K. Young, *IEEE Transactions on Electron Devices* 36 (1989) 504.
- [11] A. Dey, A. Chakravorty, N. DasGupta, A. DasGupta, *IEEE Transactions on Electron Devices* 55 (2008) 3442.
- [12] M.A. Abdi, F. Djéffal, D. Arar, M.L. Hafiane, *Journal of Materials Science: Materials in Electronics* 19 (2008) S248.
- [13] H. Abd El-hamid, J. Roig, B. Iñíguez, *Solid-State Electronics* 51 (2007) 414.
- [14] Z. Ren, R. Venugopal, S. Goasguen, S. Datta, M.S. Lundstrom, *IEEE Transactions on Electron Devices* 50 (2003) 1914.

ABSTRACT:

Sensors are central to engineering applications which are used for process control, monitoring, and safety. Sensors are also important in medicine for diagnostics, monitoring, critical care, and public health. This work is dedicated to the modeling of proposed devices and their applications in engineering systems. This dissertation is divided into four chapters; the first one is reserved to the Sensors and their applications in engineering. In the second chapter, novel designs to deep submicron FET-based chemical sensors are presented. The followed chapter, a new radiation sensitive FET (RADFET) dosimeter design (called the Dual-Dielectric Gate All around DDGAA RADFET dosimeter) to improve the radiation sensitivity performance and its analytical analysis have been proposed. Finally, in the last chapter, Improvement and Implementation of the (DDGAA) RADFET sensor in radioactive environment are presented using genetic Algorithms and artificial neural networks. We hope that this work has succeeded in reaching the fixed goals and satisfying too.

Keywords: ISFET, RADFET, gate all around, Genetic Algorithm, Sensor, Irradiation, Sensitivity, Dosimeter.

RÉSUMÉ:

Les capteurs sont au cœur des applications d'ingénierie qui sont utilisés pour le contrôle de processus, de surveillance et de sécurité. Les capteurs sont aussi importants en médecine pour le diagnostic, la surveillance, les soins intensifs et la santé publique. Le travail abordé dans cette thèse est consacré à la proposition et la modélisation des nouveaux dispositifs ainsi leurs applications dans les systèmes d'ingénierie. Cette thèse est composée de quatre chapitres: le premier chapitre expose une étude détaillée sur la notion des capteurs et leurs applications dans l'ingénierie. Dans le deuxième chapitre, la modélisation analytique et numérique des nouvelles conceptions des capteurs chimiques submicroniques à base de FET est présentée. Le chapitre suivant, un nouveau dosimètre à base de FET a été développé (appelée dosimètre à double diélectrique avec Porte enrobée DDGAA RADFET) pour améliorer les performances de sensibilité de capteur pour large domaine d'application. Le dernier chapitre est destiné à l'amélioration des performances du capteur développé et leur implémentation dans un milieu radioactif en utilisant les techniques évolutionnaires et connexionnistes. Nous pensons que ce travail a permis d'atteindre les objectifs fixés ainsi que les résultats obtenus sont satisfaisants.

Mots-clés: ISFET, RADFET, porte circulaire, algorithme génétique, Capteur, irradiation, Sensibilité, dosimètre.

:

تلعب الممجسات الإلكترونية دورا هاما في التطبيقات الهندسية، حيث تستخدم لمراقبة العمليات، والرصد، والسلامة. كما لها أهمية خاصة في مجال الطب حيث تستخدم لتشخيص الأمراض، الرصد، الرعاية الحرجة و الصحة العامة.

إذا، الهدف الرئيسي من هذه الأطروحة هو تقدير و تطوير جيل جديد من الممجسات و كذا كيفية إدماجها في النظر الهندسية ومجالات تطبيقاتها المختلفة، فضلا عن التحديات المطلوبة في التطبيقات الخاصة بهم. وتنقسم هذه الأطروحة إلى أربعة فصول: الفصل الأول مخصص لدراسة الممجسات وتطبيقاتها في مجال الهندسة. في الفصل الثاني نقوم بتقدير و تطوير جيل جديد من الممجسات الكيميائية. أما في الفصل الموالي فلقد تم تطوير نموذج تحليلي لتصميم جديد من مجسات الإشعاع (يسمى مقياس الجرعات ذو بوابة محيطية و عازل مزدوج) لتحسين أداء حساسية المجس الإشعاعي. الهدف من الفصل الأخير هو تحسين المجس المطور في الفصل السابق و تطبيقه في بيئة مشعة باستعمال تقنيات الخوارزمية الجينية و العصبيات الاصطناعية. و في الأخير نرجو أن العمل المنجز في هذه الأطروحة تمكن من بلوغ الأهداف المسطرة وتليتها أيضا.

: بوابة مزدوجة، بوابة محيطية، الشبكات العصبية الاصطناعية، الخوارزمية الجينية، الاستشعار،

الإشعاع، الحساسية، جهاز قياس الإشعاع.